Università degli Studi di Parma

Dottorato in
Scienza e Tecnologia dei Materiali Innovativi
XXI Ciclo

Growth of oxide thin films for energy devices by Pulsed Electron Deposition

Coordinatore:

Prof.ssa Anna Painelli

Supervisore:

Dr. Edmondo Gilioli

Dottorando:

Francesco Pattini

Contents

Introduction

Introduction

1.1 Worldwide energy status

During the last years the energy problem acquired more and more relevance within the social and economic situation of the world. The ever-growing energy consumption really allowed people and governments to understand the inadequacy of the fossil fuels to satisfy all the energy requirements necessary for long time. With the passing of time, many studies and researches have been driven to renewable and sustainable resources such as solar or geothermal energy, water power or wind power.

Moreover, the environmental pollution come into the limelight and deep studies to reach effective solutions appear necessary to conserve the environment for the present and the future. Frequently weather conditions dramatically change showing the relevance of the human behaviour and its negative effect on our life: desert areas are growing in number and width; the global warming is concrete and the melting of the perennial glaciers or the icecaps already raised the sea level.

Furthermore, world economy could get some benefits on renewable resources and in particular underdeveloped and developing countries where energy distribution appears difficult and too much expansive. Almost all of the 1,6 – 2 billion people who live without access to electricity, relying for their daily energy services, live in the developing world.

Lots of studies revealed the existence of a clear relationship between poverty and access to electricity and for this reason, poverty levels increase the more remote and inaccessible the communities are, while costs for electrification trough traditional method like grid connection increase due to transport and maintenance costs[1].

Renewable energy systems are favourable energy options, but the main challenge is to reduce their price to a competitive level, this could be reached thanks to the increasing global markets in new energy technologies that offer a large business potential to be captured. Wind and photovoltaics have now annual markets exceeding $20 billion each and the opportunities increased to $200 billion in 2006[2]. The total investments in the renewable power sector were $59 billion in 2006, of which over half in new technology and manufacturing capacity[3]. Further the growing markets for new energy technologies

and sources create new employment and export markets. For example, Germany, well-known for strong market incentives (i.e. feed-in-tariffs or VAT reduction) in renewable energy, demonstrated in 2006 a total turnover of €21,6 billion and 200000 working places in Renewable energy systems, mostly created during the last 10 years under strong domestic energy policies[4] while the number of jobs in renewable energy in the United States was 450,000 in the same year[5].

However the fossil fuel extraction and consumption played a central role in energy production field and this run is considered to last for long time (**fig. 1.1**).

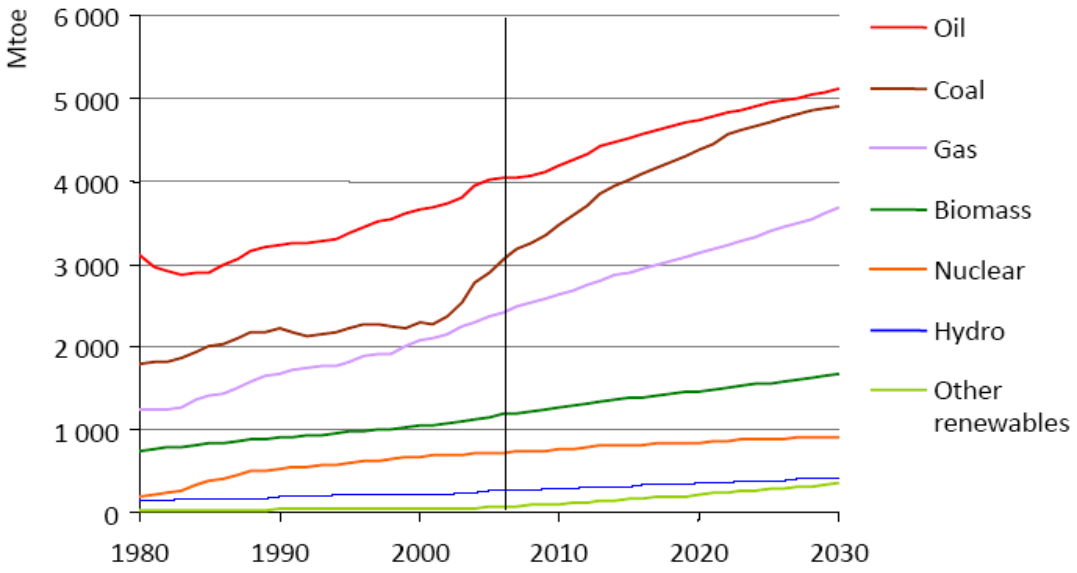

Fig. 1.1 – Evolution of total energy demand by resources from 1980 and forecast by 2030 in the world [6]

As shown in figure **1.2** most of energy consumption is due to commercial and residential use in developed countries but the level is much higher for industrial production in developing countries. Considering the large use of fossil fuel, population increases and the number of large industrial plants rapidly growing in the developing countries explains the continuous increase of energy requirement all over the world. From an economic point of view for developing countries, this is an interesting chance to grow and form an affluent society fighting against unemployment and poorness. But, on the other hand, the present behaviour will have also negative repercussion on the world, in particular for the present state of the high production of greenhouse gases related to the combustion of the fossil fuels.

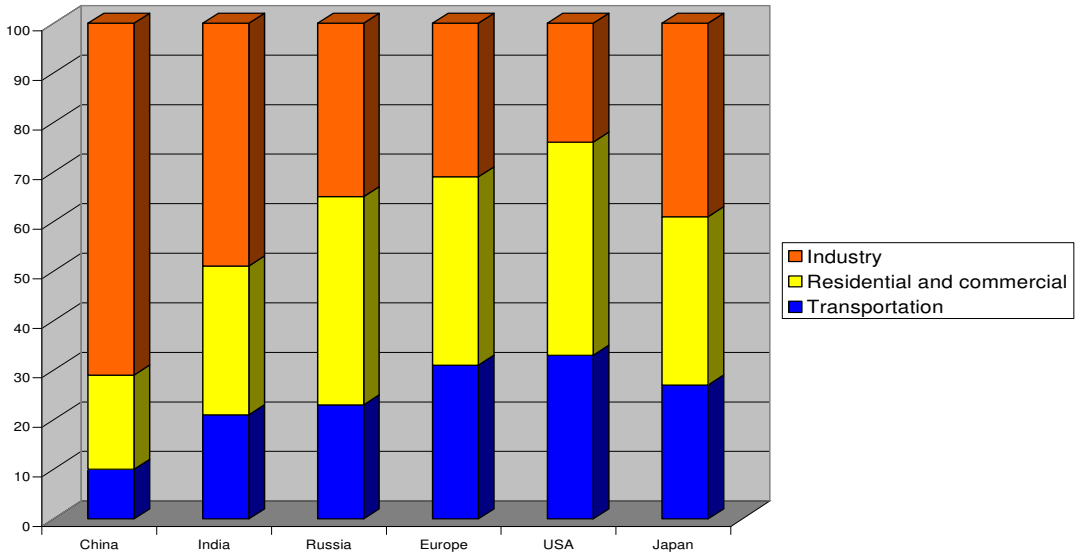

Fig. 1.2 – Total energy demand by sectors in 2005 in the developed and developing areas [1]

Indeed, the annual CO_2 emission (**fig. 1.3**) caused by consumption and production of energy presents the same behaviour of the total energy demand of the world, showing a sharp slope for developing and populated countries like China. Referring to **figure 1.1** you can exactly overlap the behaviour of coal consumption in the world with CO_2 emission produced by China.

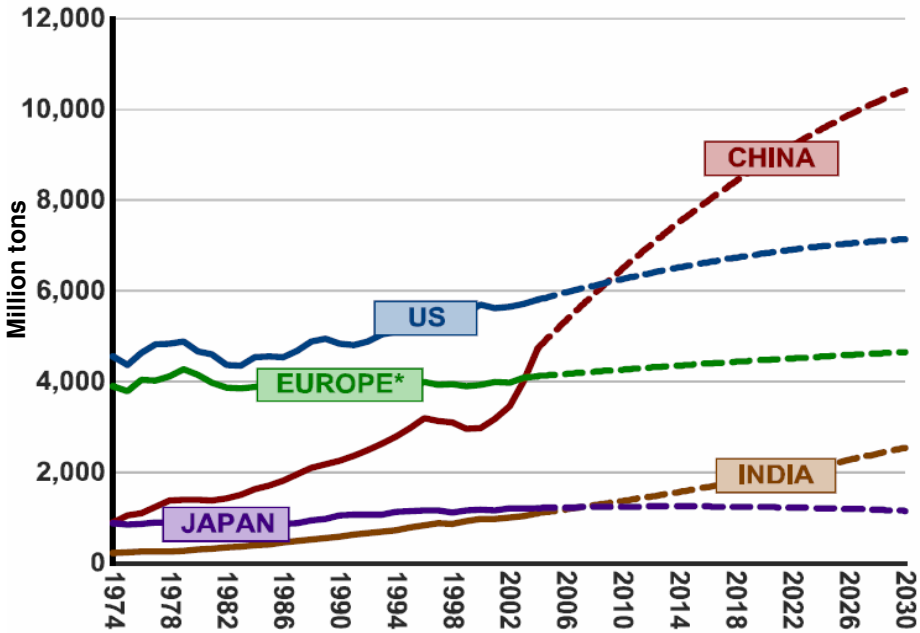

Fig. 1.3 – Data and forecast for annual CO_2 emission in the developed and developing areas [1]

1.2 Renewable sources: an overview

International Energy Agency (IEA) defines renewable energy as energy derived from natural processes that are replenished constantly. This definition applies to a wide range of energy sources derived directly or indirectly from the sun including solar, hydro, wind, biomass, but also includes non-solar sources such as geothermal, tidal and ocean currents. Renewable energy offers our planet a chance to reduce carbon emissions, clean the air, and prepare a more sustainable world for our civilization. It also offers countries around the world the chance to improve their energy security and spur economic development.

Up to now, more than 65 countries have goals for their own renewable energy futures and they are enacting a far-reaching array of policies to achieve those important results. Moreover many renewable technologies and productions are growing at a trend comprosed between 20 and 60%, year by year, capturing the interest of the largest global companies.

In 2007, more than $100 billion was invested in new renewable energy capacity, manufacturing plants, and research and development[7].

1.2.1 Geothermal

Geothermal energy is produced by the heat within the Earth where it can reach even 4000°C. Residual heat of the planet and the decay of some radioactive materials inside (Uranium, Thorium, etc.) originate this type of energy. Geothermal energy can be considered really inexhaustible and it is simple to collect because it propagates by conduction through compact rocks and by convection thanks to fluids present in the permeable and fractured ones, moving to the surface with an average decrease of about 3°C per 100 meters.

The Earth could be considered as an immense reservoir of heat: it is estimated that the heat contained within the first 5 km of the Earth's crust corresponds to about a half million times the current global need. Unfortunately this type of energy appears highly dispersed and hardly retrievable under advantageous means. On the other hand it has the important characteristic of being relatively constant over time, free from weather limitations such as diurnal or seasonal fluctuations and, what is most interesting from the economic point of view, is concentrated in areas with thermal anomalies (i.e. secondary volcanism) where it

may reach values of temperature directly exploitable by manufacturing plant. In these areas the water is heated by geothermal energy and it becomes available in the form of hot fluid or steam useful for thermal heating or electricity production, depending on its temperature and characteristics[8].

1.2.2 Wind power

Wind energy, caused by movements of air among zones of high and low atmospheric pressure, has spread everywhere on Earth but only in some areas is sufficiently intense and regular to submit some interest in practical use.

The exploitation of the wind for obtaining energy directly useful for navigation or for irrigation and processing for farming dated right from the beginning of human civilization and it is still practiced in different ways.

However, the conversion of wind energy into electricity is fairly recent. This process conceptually derives from the traditional windmills and are composed by a rotor blade installed on a fixed hub and designed to steal from the wind a part of its kinetic energy. Through the rotation of the blades electricity is generated by the turbine and it can be put into the grid or stocked in batteries. Actually the modern wind turbines have little in common with the traditional windmills, because they are very sophisticated machinery, made with materials able to resist stresses often comparable with those withstood by the wings of airplanes. The wind speed performs a crucial role in the design of the machines and in the calculation of the wind potential in a site. Therefore, a long-term study about changes in wind speed is essential for the purposes of a cost-effective exploitation of wind energy.

Wind energy is a real emission-free resource because the conversion to electricity is realized without any release of polluting substances in the atmosphere. The technology of electricity production based on wind power is the most mature and closer to the traditional sources among the new renewable ones. This explains the massive development rising in recent years, particularly in European Union, where the wind power installed is the largest in the world[9].

1.2.3 Water power

The energy production related to the water is based on its kinetic energy gained from energy potential lost in a jump or a downward path. It has been used for a long time for energy purposes and it was the first widely used energy source substituting human or animal efforts.

Up to now, first use of energy water is related to the production of electricity. In particular it is based on the course and on the flow of the rivers. Presence of falls are essential to optimally gain the most energy from the water and they could be natural or artificial. The most important and largest existing plants to produce electricity (hydroelectric plants) are built up near the largest rivers of the world, for example, in 1984 the Parana River, the border between Brazil and Paraguay, was inaugurated central Itaipu, which had a total capacity of 12600 MW then upgraded to 14000 MW in 2003. In October 2008, in China started the electricity production by the largest hydroelectric plant called "Three Gorges" on the Yang-Tze River and in 2009 will be completed making available a capacity of 22500 MW **(tab.1.1)**.

Name	**State**	**Year of completion**	**Total capacity (MW)**	**Electricity production (TWh)**
Three Gorges Dam	China	2008 – 2009	18300 – 22500	More than 100
Itaipu	Brazil/Paraguay	1984 – 2003	14000	90
Guri	Venezuela	1986	10200	46
Tucurui	Brazil	1984	8370	21
Grand Coulee	USA	1942 – 1980	6809	22,6
Sayano Shushenskaya	Russia	1985 – 1989	6400	26,8
Krasnoyarskaya	Russia	1972	6000	20,4
Robert-Bourassa	Canada	1981	5616	29
Churchill Falls	Canada	1971	5429	35
Bratskaya	Russia	1967	4500	22,6

Tab. 1.1 – List of the ten largest hydroelectric plants over the world [10]

As in the case of energy production from wind-power, electricity generated by hydropower plants do not have any type of pollutant emission. The only environmental impact is the alteration of natural habitats resulting from the buildings of artificial dams and the installation of pipes to optimize the use of hydraulics.

So far hydropower results the most important among the renewable resources. It contributes more than 6% to the global demand for primary energy but with much higher values for certain geographical areas, for example 27,5% in the South of America and more than 30% expected in the next years in China.

1.2.4 Biomass and biofuels

Most renewable heat is generated from biomass. It offers good future potential as an energy source able to replace fossil fuels. The stored solar energy in biomass from biodegradable matter can be converted into usable forms of bioenergy used for heating and cooling, or into other energy carriers as well as materials and chemicals. Biomass is very diverse and includes wood residues, organic wastes, crop residues, crops grown specifically for energy production, animal wastes, black liquor (the lignin-containing sulphite lies in the alkaline-spent liquor from pulp and paper production) and municipal solid waste (MSW). Due to the limited availability of land, biomass production for energy must be balanced against the need for food, fibre, animal feed, materials, biochemicals and forest sinks. Wood chips and pellets accounted for 5,7% of renewable heat generation in 2006[1].

Biofuels, also known as agrofuel, are fuels mainly derived from biomass or bio-waste. These fuels can be used for any purposes, but the main use is in the transportation sector. Most of the vehicles require liquid fuels which provide high power. Furthermore, clean fuels are needed to avoid additional greenhouse gases emission. For other forms of non transportation applications there are other alternative solid biomass fuel like wood that has been brought into use since a very long period and seems to be one of the major contributors of global warming[11].

Biofuels are the best way to reduce the emission of the greenhouse gases. They can also be looked upon as a way of energy security which stands as an alternative of fossil fuels limited in availability. Today, the use of biofuels has expanded throughout the globe. Some

of the major producers and users of biogases are Asia, Europe and America. Theoretically, biofuel can be easily produced through any carbon source; making the photosynthetic plants the most commonly used material for production. Almost all types of materials derived from the plants are used for manufacturing biogas. One of the greatest problems that is being faced by the researchers in the biofules field is how to covert the biomass energy into the liquid fuel. Some plants, such as jatropha and algae, are grown to naturally produce oil. These oils are heated to reduce their viscosity after which they are directly used as fuel for diesel engines or can be further treated to produce biodiesel suitable for various purposes[12]. Alternative methods are used to produce ethanol, but they need more energy than they produce. Indeed, fertilizing, harvesting, transport and corn processing are necessary to grow and transform sugar crops and starch in ethanol and they are all expensive procedures.

Some of the agricultural products that are specially grown for the production of biofuels are switchgrass, soybeans and corn in United States. Brazil produces sugar cane, Europe produces sugar beet and wheat while, China produces cassava and sorghum, south-east Asia produces miscanthus and palm oil while India produces jatropha.

Unfortunately, considering the forecasts on population growth all over the world, the humanitarian policy would be to maintain cropland for growing food and not fuel. Every day more than 16000 children die from hunger-related causes[13] and the situation would get worse. It would be morally wrong to divert cropland needed for human food to powering automobiles and intensive cultivation that also deplete soil fertility and the food production capability.

On the other side, most of the biofuels are derived from biomass or bio waste. Biomass can be termed as material derived from recently living organism. Most of the biomass is obtained from plants and animals and also include their by products. The most important feature of biomass is due to their natural origin as suitable renewable source of energy but we must remember that we need wood and forest for oxygen production and CO_2 reduction and they need some years to grow and few seconds to fall.

1.2.5 Solar Energy

With the passing of time from the first appearance of the civilization, humans get used to the sun and its energy, neglecting the importance for the present and the future of our world. Indeed, solar energy passes atmosphere in heat and light forms influencing climate or weather and sustaining life on Earth. Solar energy can be considered the principal renewable source because all other renewable energies, except geothermal, derive from energy received by the sun, for example, wind is a manifestation of the atmospheric circulation driven by solar energy causing differences of pressure among different warm masses of air[14]. Rather, we can assert that the sunlight is the origin of all the energy resources since the conversion of solar energy into chemical energy via photosynthesis produces food, wood and the biomass from which fossil fuels are derived[15].

Since ancient times the radiation of the sun has been used by the humans for agriculture and for various direct uses such as warming or cooking, but with new studies and new technologies aimed to new forms of solar energy exploitation, scientist and researchers reconsidered the sunlight and its interaction with new materials for various applications. For example, to this day, heating is one of the most requested energy product and the demand for heating accounts for a significant portion of world total energy demand. The building sector consumes 35,3% of final energy demand of which 75,0% is for space and domestic water heating[16].

Solar thermal is a relatively mature technology that has proven to be reliable and cost-competitive under certain circumstances since solar water heaters first became commercially available over thirty years ago. These modules already reached a significant market share in some countries such as China, Turkey, Japan, Israel and Germany.

A very interesting use of solar energy born during the 80's and it was developed for poor countries where water disinfection was difficult or expansive chemical products were needed. A group of medical researchers found that a great number of bacteria contained in water extracted by wells and closed in glass bottles were killed by UVA solar radiation after one day, or more, of exposure under sunlight[17]. Lots of studies followed and SODIS method[18,19] became at the same time a simple and great tool to obtain safe drinking water. This technique provided adequate water supply and sanitation facilities avoiding or

reducing serious health hazard and water-borne diseases for children or people living in poor countries.

The most-known application related to the sunlight is the electrical generation provided by photovoltaic materials that will be deeply discussed in next pages.

1.3 Aim and outline of this research

Since energy need of the world will increase more and more, the importance of renewable resources and energy efficiency became urgent and evident. After preliminary remarks about energy market and renewable resources chances, in this Thesis thin films deposition technique will be described in details. In III and V chapters, High Temperature Superconductor Coated Conductors (HTS-CC) devices and thin-film solar cells will be briefly presented to go into details of the importance and the studies carried out in this research about innovative materials to solve some problems related to these electrical devices.

HTS-CC can be seen as excellent devices to reduce energy waste in current transport and to enhance electricity generation by high performance turbines. At the moment, industrial production of Coated Conductors has not yet reached its full capacity operation, but hundreds of meter long tapes have been already realized. The main issue that slow down the concrete production is due to the high costs of the final device. Obviously it should be less than the copper cable cost, in order to prompt the substitution of old metal-based conductive cable with HTS-CC. One of the reasons causing this high cost is the complex multi-layer structure at the base of the HTS-CC[20], where several films are deposited by different method on a metal tape. In particular, as it turns out from market analysis evaluations, if the deposition rate of the complete HTS-CC increases enough to reach the cost/performance of 10 €/KA*m, the market penetration becomes a concrete possibility. In order to achieve this value a simplified architecture and effective deposition technique must be used.

In parallel, we direct our efforts to the thin-film solar cell, in order to realize high efficiency thin films solar cell based on CIGS. Second generation PV cells present a multi-layer architecture with an absorber layer made by a semiconductor material generally

grown between of Transparent Conductive Oxide (TCO) layer and a metal back contact film.

These two type of technologies could be very useful for a clever energy use in the future and they can contribute to perform a complete system for energy production and distribution avoiding fossil fuel necessity, CO_2 production and high energy waste. Nevertheless several problems remain unsolved and we faced them trying to clear and obtaining very promising results in a view of improving material properties and cost-effective devices to penetrate energy market.

This work has been partially financed by Edison S.P.A., in the frame of a collaboration, started in 2000, with IMEM-CNR. Hitherto, various national patents has been presented and in the last year three national patents concerning material production and technology development of Pulsed Electron Deposition (PED) route were deposited.

PED was first reported in different works on HTS thin films deposition during the 80s. It is conceptually similar to the Pulsed Laser Deposition (PLD) and certainly provides lots of opportunities and remarkable improvement margins in thin films deposition. From a the economic point of view the PED method is expected to offer significant cost-performance advantage relative to PLD, especially over large area deposition in view of industrial production.

The PED technique will be described in details (chapter 2) followed by some pages dedicated to an overview about superconductivity and High Temperature Superconductor Coated Conductors (HTS-CCs) (chapter 3). Related to this issue, the single buffer layer architecture based on doped-Ceria will be presented (chapter 4). This is an innovative idea designed, realized and characterized in our laboratory to reach a cost-effective route to product long-length CCs for energy applications and remarkable results obtained will be reported. The next chapter (chapter 5) introduces thin film solar cells based on CIGS (Cu(In, Ga) Se_2) to deepen the description of ZnO and Al-doped ZnO films as suitable TCO for PV in the next one (chapter 6). In this chapter, results reached for the samples grown and characterized at IMEM will be reported. At the end, conclusions and perspective will be presented for the application of PED to improve and simplify thin film deposition both for HTS-CC and 2^{nd} generation solar cells.

References

[1] International Energy Agency (IEA): World Energy Outlook 2006, (2006) Paris http://www.worldenergyoutlook.org/2006.asp

[2] J. Makower and C. Pernick Wilder: "Clean energy trends" (2007) http://www.cleanedge.com

[3] A. McCrone: "Winning over the skeptics. The continued rise of private equity investment in clean energy", *Renewable Energy World* (2007) pp. 41-49

[4] D. Marinova, A. Balaguer: "Transformation in the photovoltaics industry in Australia, Germany and Japan: Comparison of actors, knowledge, institutions and markets", *Renewable Energy*, *Volume 34, Issue 2* (2009), pp. 461-464

[5] R.H. Bezdek: "Renewable energy: economic powerhouse?", *Solar Today* **21** (2007), pp. 30-33

[6] International Energy Agency (IEA), World Energy Outlook 2008, (2008) London

[7] Renewable Energy Policy Network for the 21st Century (REN21), Renewables 2007, Global Status Report (2007) http://www.ren21.net/globalstatusreport/

[8] Istituto Superiore per la Ricerca Ambientale (ISPRA), http://www.apat.gov.it/site/it-IT/Temi/Energia_rinnovabile

[9] ENEL s.p.a. http://www.enel.it/attivita/ambiente/

[10] H.Khemani: "Ten Largest Hydroelctric Power Plants of the World", *Mechanical Engineering* (2008)

[11] Biofuel information, http://biofuel.org.uk/

[12] Z. Nazim, T. Muradov, N. Veziroğlu: ""Green" path from fossil-based to hydrogen economy: an overview of carbon-neutral technologies", *International Journal of Hydrogen Energy* (2008) in press

[13] R. E. Black, L. H. Allen, Z. A. Bhutta, L. E. Caulfield, M. de Onis, M. Ezzati, C. Mathers, J. Rivera: "Maternal and child undernutrition: global and regional exposures and health consequences", *The Lancet* (2008) **371**, pp. 243 - 260

[14] H. Le Treut, R. Somerville, U. Cubasch, Y. Ding, C. Mauritzen, A. Mokssit, T. Peterson, and M. Prather: "Historical Overview of Climate Change", *Climate Change 2007: The Physical Science Basis. Contribution of Working Group I to the Fourth Assessment Report of the Intergovernmental Panel on Climate Change,* (2007)

[15] W.Vermass: "An Introduction to Photosynthesis and Its Applications", Arizona State University (2007)

[16] International Energy Agency (IEA): "Renewables for heating and cooling" (2007), Paris

[17] A. Acra, Y. Karahagopian, Z. Raffoul, and R. Dajani: "Disinfection of oral Rehydration Solutions by Sunlight", *The Lancet,* (1980) **316** pp 1257- 1258

[18] Acra, Z. Raffoul, Y. Karahagopian: "Solar Disinfection of Drinking Water and Oral Rehydration Solutions", (1984) UNICEF report

[19] S. Murinda, S. Kraemer: "The potential of solar water disinfection as a household water treatment method in peri-urban Zimbabwe", *Physics and Chemistry of the Earth,* (2008) **33**, pp.829–832A.

[20] J. G. Bednorz, K. A. Muller, *Zeitschrift fur Physik B-Condensed Matter*, (1986) **64**

The Pulsed Electron Deposition technique

Introduction

In thin film technology the highest level of importance is related to deposition techniques that allow film growth with the desired properties. A lot of deposition method have been studied and some of them are still used, also for industrial production of thin film-based devices.

Vacuum deposition technique can be grouped in two main categories: physical vapour deposition (PVD) and chemical vapour deposition (CVD).

The basic PVD processes fall into two general categories: sputtering and evaporation. The application of PVD techniques ranges over a wide variety of applications from decorative, to high temperature superconducting films. Coupled with an effective growth-rate control, the thickness of the deposits can vary from angstroms to millimetres. A very large number of inorganic materials, such as metals, alloys, compounds, and mixtures, as well as some organic materials can be deposited using PVD technologies[1]. In physical vapour deposition (PVD) processes, the coating is deposited in vacuum by condensation from a flux of neutral or ionized atoms of materials listed above. In order to keep the materials very pure, physical vapour deposition processes require the use of very good vacuums system.

The factors that distinguish PVD from CVD are the following: reliance on solid or molten sources, as opposed to generally gaseous precursors in CVD; the physical mechanisms (evaporation or by means of impact) by which source atoms enter the gas phase; a reduced background pressure through which the gaseous species are transported; the general absence of chemical reactions in the gas phase and at the substrate surface (only reactive PVD processes are exceptions).

Besides vapour phase deposition also liquid phase (LPE) or by sol-gel route can be used to grow thin film with a high deposition-rate and a thickness control comparable to the vacuum technique. For several materials is made a frequent use of these deposition routes for the relative low-costs of the apparatus and the simply growing procedure. The problems related to LPE techniques are due to:

- reactant costs and toxicity (as in CVD technique);

- the low control of chemical, structural and morphologic homogeneity long the whole film;
- the necessity of many deposition steps and thermal treatments that give the techniques a difficult complementation with other deposition system.

Although scaling-up potential of LPE is very high, while PVD technique are still more reliable and therefore widely used for thin films deposition route.

2.1 Thin films deposition techniques

2.1.1 Sputtering

Sputter deposition is a PVD method of depositing thin films discovered in the 1850's. With the advent of modern vacuum technology it is now possible to deposit films of very high quality.

Sputtering typically involves the erosion of a cathode by plasma-extracted ions that hit the target placed onto the cathode and physically eject the atoms from the target surface (**fig. 2.1**). Sputtering sources are usually magnetrons that utilize strong electric and magnetic fields to trap electrons close to the surface of the magnetron on which is positioned the target. The electrons follow helical paths around the magnetic field lines producing more ionizing collisions with inert gas near the target surface. The sputter gas is an inert one, typically argon. The extra argon ions created as a result of these collisions leads to a higher deposition rate. It also allows to sustain the plasma at a lower pressure. The sputtered atoms are neutrally charged and so are unaffected by the magnetic trap. Charge build-up on insulating targets can be avoided with the use of RF source instead of the typical direct current (DC) ones where the sign of the anode-cathode bias is varied at a high rate. RF sputtering systems works well to produce highly insulating oxide films while DC power supply is dedicated to deposit pure metal, alloys or conductive compounds[2].

With particular materials or deposition steps, it is often used a method called “reactive sputtering”. In this case the deposited film is formed by chemical reaction between the target material and a reactant under gas form introduced into the vacuum chamber. The composition of the film can be controlled by varying the relative pressures of the inert and reactive gases. Oxide and nitride films are often fabricated using reactive sputtering. To

increase the deposition rate, is often used the Magnetron sputtering, where the magnetic device can be added to the RF or DC typical apparatus included in the target holder.

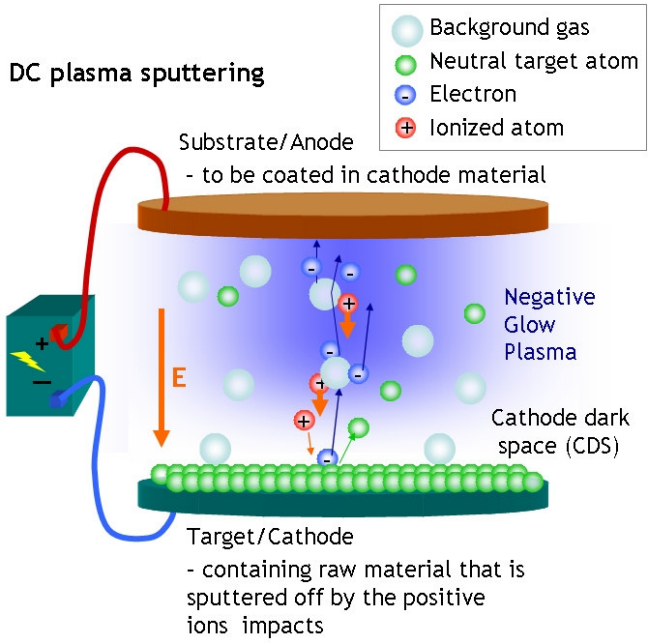

Fig. 2.1 – Sputtering deposition system equipped with DC power supply

2.1.2 Thermal Evaporation

The vacuum thermal evaporation deposition technique consists in heating until melting and evaporating the material to be deposited. The material vapour finally condenses in form of thin film on the substrate surface and on the vacuum chamber walls that causes a great waste of evaporated. Usually low pressures are pumped, about 10^{-6} or 10^{-5} mbar, to avoid reaction between vapours and atmosphere. At these low pressures, the mean free path of atoms is the same order as the vacuum chamber dimensions, so these particles travel in straight lines from the evaporation source towards the substrate. This originates 'shadowing' phenomena with 3D objects, especially in those regions not directly accessible from the evaporation source. Besides, in thermal evaporation techniques the average energy of vapour atoms reaching the substrate surface is generally low. This affects seriously the morphology of the films, often resulting in a porous and little adherent material. In thermal evaporation techniques, different methods can be applied to heat the material[3]. The equipments available use either resistance heating (by means Joule effect)

or bombardment with a relatively energetic and continuous electron beam, from an electron gun[4].

The assembly of the former technique is simple and results appropriate for depositing metals and some compounds with low melting temperature (**fig 2.2**).

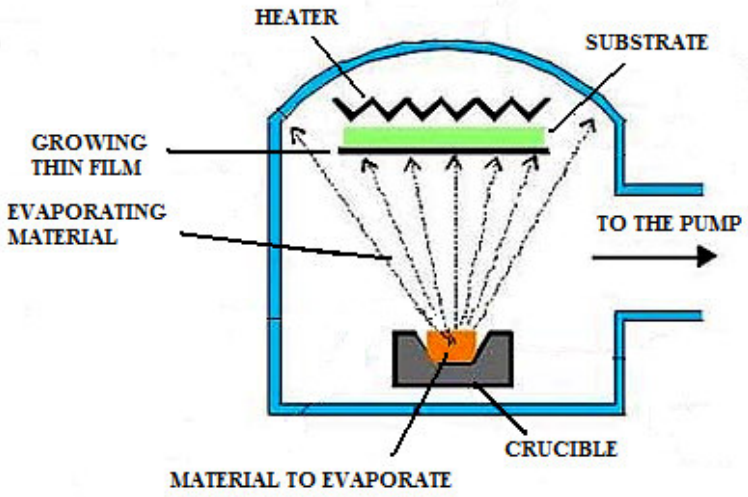

Fig. 2.2 – Thermal Evaporation system scheme

The second type of source generates free electrons by means the thermo-ionic emission caused by an incandescent filament (cathode). Emitted electrons are accelerated towards an anode by a high difference of potential. The crucible itself, or a near perforated disc, can act as the anode. A magnetic field is generally applied to bend the electron trajectory, allowing the electron gun to be positioned below the evaporation line (**fig. 2.3**).

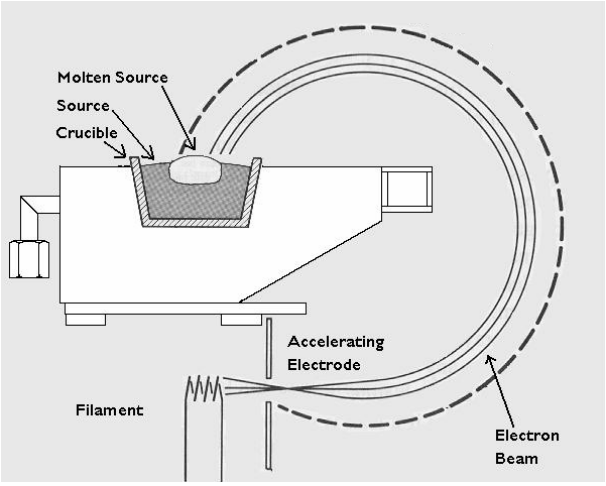

Fig. 2.3 – Electron Beam Gun for high melting point compounds thermal evaporation

As electrons can be focalized, it is possible to obtain a very localized heating on the material to evaporate, with a high density of evaporation power (several kW). This allows to control the evaporation rate, from low to very high values, and best of all, the chance of depositing metals and compounds with high melting point. The possibility of cooling the crucible avoids contamination degasification problems related to the heating.

By the use of two ore more crucibles, both in the 2 types of thermal evaporation described, it becomes possible the deposition of particularly complicated structure and compounds such as High Temperature Superconducting films (YBCO) or semiconductor absorbers for photovoltaic applications (CIGS).

2.1.3 Molecular Beam Epitaxy (MBE)

Molecular beam epitaxy is a technique for epitaxial growth via the interaction of one or several molecular or atomic beams that occurs on a surface of a heated crystalline substrate. Solid materials are placed in evaporation cells to provide an angular distribution of atoms or molecules in a beam[5]. The substrate is heated to the necessary temperature and, when needed, continuously rotated to improve the growth homogeneity (**fig. 2.4**).

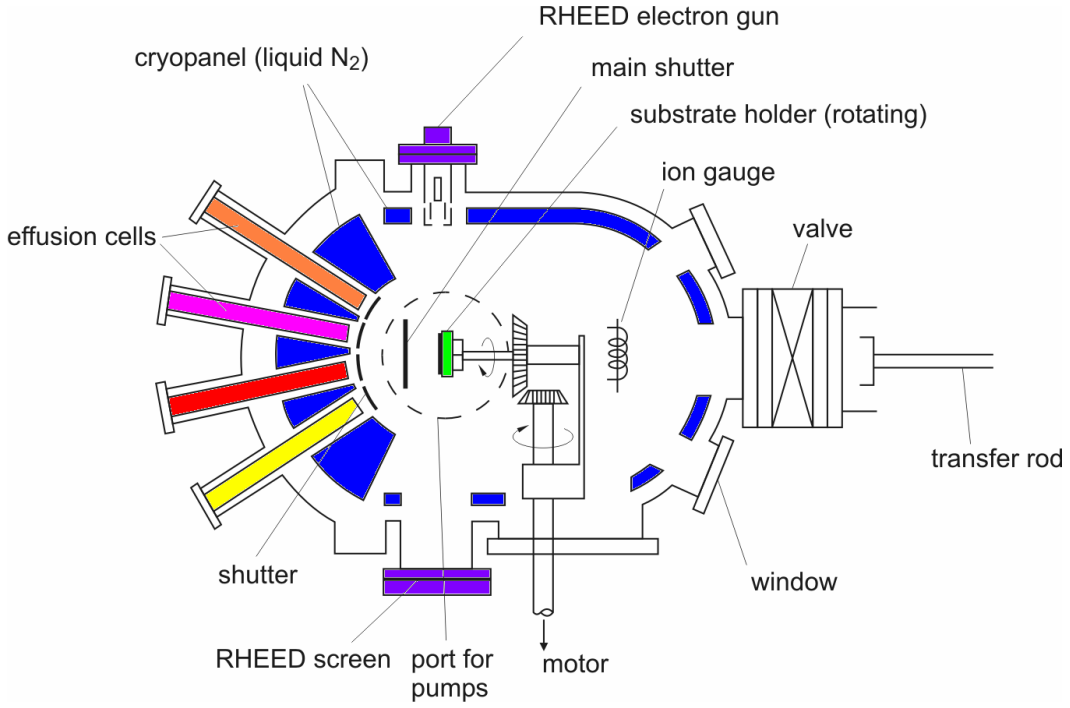

Fig. 2.4 – Scheme of the Molecular Beam Epitaxy system

Epitaxial growth and high purity of the films need extremely clean deposition chamber so ultra high vacuum (UHV) is required. Thus, UHV is the essential environment for MBE. Therefore, the rate of gas evolution from the materials in the chamber has to be as low as possible and for this reason pyrolytic boron nitride is chosen for the crucibles which gives low rate of gas evolution and chemical stability up to 1400°C. Also Molybdenum and Tantalum are widely used for the shutters, the heaters and other components, and only ultra-pure materials are used as source[6].

To reach UHV, a bake-out of the whole chamber at approximately 200°C for 24 h is required. Cryogenic screenings around the substrate minimizes spurious fluxes of atoms and molecules from the walls of the chamber avoiding the presence of undesired doping particles in the growth atmosphere.

Despite big technological problems and expansive features, MBE systems permit an excellent control of composition and doping of the growing structure at monolayer level by changing the nature of the incoming beam just by opening and closing mechanical shutters. The operation time of a shutter of approximately 0,1 second is normally much shorter than the time needed to grow one monolayer (from 1 to 5 s). Consequently the deposition rate of MBE apparatus is very low. Moreover the complete system is very complicated, expansive and not feasible for large area deposition. All of these characteristics render the technique not suitable for industrial application, although MBE is very common in laboratory studies, in particular for semiconductor-based devices.

The UHV environment of the system is also ideal for many in-situ characterization tools, like the RHEED (Reflection High Energy Electron Diffraction) technique, where the oscillation of the electron signal exactly corresponds to the time needed to grow a monolayer and the diffraction pattern on the RHEED screen gives direct indication about the state of the surface and the modality of layer growing. In addition, another in-situ monitoring system based on atomic absorption spectroscopy can be installed on MBE to control the amount of specific element. Thanks to the light beam passing through the elemental fluxes, the attenuated signal measured by photomultiplier tube (PMT) can be used to calculate the compositional ratio of co-evaporated material permitting to adjust the deposition parameters and thus obtain the optimal value[7].

2.1.4 Metal-organic Chemical Vapour Deposition (MOCVD)

Metal-organic Chemical Vapour Deposition (MOCVD or MOVPE) belongs to the chemical vapour deposition method which not imply an epitaxial growth. The formation of the films, especially compound semiconductors, takes place at the surface of the substrate after the reaction of organic compounds or more often metal-organics and metal hydrides containing the required chemical elements. The growth of the layers occur by final pyrolisis at the substrate surface of the chemical constituents reacted. The reaction takes place not in a vacuum, but in vapour phase at moderate pressures (10 to 100 mbar) among the gases introduced in the deposition chamber[8] (**fig. 2.5**).

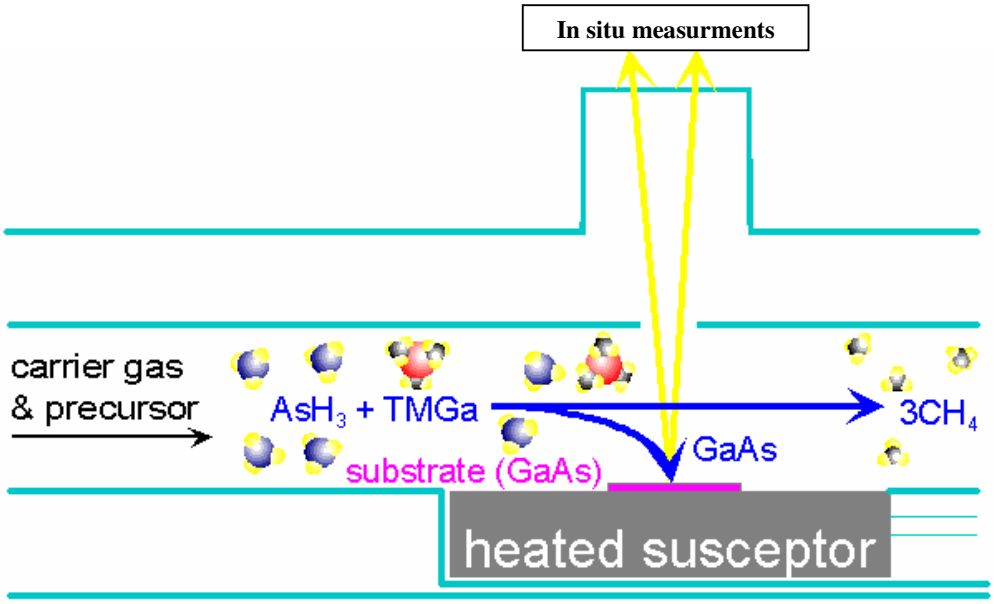

Fig. 2.5 – Metal-organic Chemical Vapour Deposition System with the reaction for growing GaAs/GaAs

The reagents are conveyed by the carrier gas, with a flow rate between 0,1 and 1 m/s, toward the reaction chamber, where the substrate is placed and where the deposition occurs under certain temperature and pressure conditions. The growth rate is usually around 1 µm/h and in contrast with MBE it is possible to deposit on a large scale. Some industries are currently producing devices using MOVPE deposition by means planetary reactors containing up to sixty substrates of 2 inches or 5 substrates up to 10 inches. Films realized in this way present high compositional and morphological uniformity over all the substrates.

2.1.5 Pulsed Laser Deposition (PLD)

In 1965 Smith and Turner, after the publications of some works about the use of ruby laser to vaporize and excite atoms from a solid surface, used laser to deposit thin films marking the start of the development of the pulsed laser deposition (PLD) technique. PLD is a thin film deposition technique where a high power pulsed laser beam is focused inside a vacuum chamber to strike a target of the desired compound. Material is then ablated from the target to form a plasma plume direct to the substrate where the compounds condenses as a thin film[9] (**fig. 2.6**).

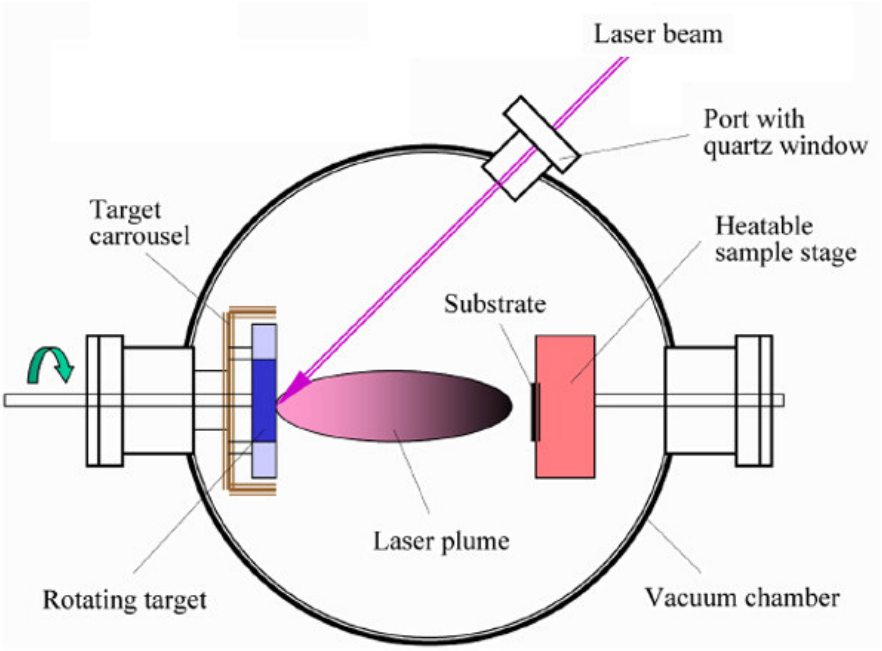

Fig. 2.6 – Pulsed Laser Deposition technique scheme

Thanks to the only presence of a UV radiation as energy source inside the chamber, the deposition step is very clean and this process can occur in ultra high vacuum or in the presence of a reactive or inert background gas. While the basic-setup is simple compared to many other deposition techniques, the physical phenomena of laser-target interaction and film growth are quite complex. When the laser pulse is absorbed by the target, energy is first converted to electronic excitation and then into thermal, chemical and mechanical energy resulting in evaporation, ablation, plasma formation and even exfoliation[10]. The ejected species expand in form of a plume containing lots of energetic species: atoms,

molecules, electrons, ions, clusters, particulates and molten globules, before depositing on the typically hot substrate.

The technique of PLD was found to have significant benefits over other film deposition methods, thanks to:

1. the capability for stoichiometric transfer of material from target to substrate;
2. relatively high deposition rates, typically ~10 nm/min, can be achieved at moderate laser fluxes;
3. the use of a carousel, housing a number of target materials, enables multilayer films deposition without the need to break vacuum for changing materials.

In spite of these significant advantages, most applications have been confined to the research environment and industrial uses did not take place. There are basically three main reasons for this:

1. the plasma plume created during the laser ablation process is highly forward directed, therefore the thickness of material collected on a substrate is highly non-uniform and the composition can vary across the film. Moreover the area of deposited material is also quite small, typically ~1 cm^2, in comparison to that required for many industrial applications where a much larger area coverage is required;
2. the ablated material contains macroscopic globules of molten material, up to 10 μm diameter. The inclusion of these particulates during the film growth is obviously detrimental to the properties of the material;
3. deposition of novel materials usually involves a not-short period of empirical optimization of deposition parameters because the fundamental processes occurring during the ablation an the consequently plume formation are not deeply understood.

2.1.6 Liquid phase epitaxy (LPE)

Liquid phase epitaxy (LPE) is a simple method to grow different materials layers from the melt on solid substrates. The most remarkable feature is related to the low temperatures used, well below the melting point of the compound to be deposited. The desired material is dissolved in the melt of another compound and the deposition process have place once fixed conditions of little supersaturation between dissolution and segregation. The

deposition of the layer on the substrate is slowly and uniform. The equilibrium conditions greatly depend on the temperature and on the concentration of the dissolved compound in the melt[11]. The growth of the layer from the liquid phase can be controlled by a forced cooling of the molten system. Impurity introduction can be strongly reduced and doping can be controlled with great accuracy by the addition of necessary dopants.

The method is mainly used for the growth of semiconductor compounds and very thin, uniform and high quality layers can be produced[12].

Substrates like semiconductor wafers, glass or ceramic can be applied for various applications. As in the case of the other deposition techniques, to facilitate nucleation, and to avoid tension in the grown layer, the thermal expansion coefficient of substrate and grown layer should be similar.

Two different tools have been realized for LPE: horizontal and vertical. In the case of a horizontal tool the melt or the melts are subsequently brought in contact with the substrate by a sliding boat system. By this way, it is possible to grow multi-layer stacks in an easy and automated process. Depending on the set-up of the system one or several wafer can be processed at the same time. On the other hand, the bowl volume is small, and the melt needs to be refreshed after each growth experiment.

A vertical system is usually used in combination with a dipping system for the liquid phase epitaxy growth. The samples are lowered into the melt with the aid of a pull-rod. In this system the melt volume to substrate surface area is much higher, giving the opportunity to grow thicker layers at a relatively high rate. Some complications arise when several substrates must be processed at the same time.

2.1.7 Sol-gel technology

The sol-gel process is a versatile solution process for making ceramic and glass materials. In general, the sol-gel process involves the transition of a system from a liquid "sol" (mostly colloidal) into a solid "gel" phase. Applying the sol-gel process, it is possible to fabricate ceramic or glass materials in a wide variety of forms: nanoclusters, ultra-fine or spherical shaped powders, thin film coatings, ceramic fibres, microporous inorganic membranes, monolithic ceramics and glasses, or extremely porous aerogel materials[13]. The starting materials used in the preparation of the "sol" are usually inorganic metal salts

or metal organic compounds, specially metal alkoxides. In a typical sol-gel process, the precursor is subjected to a series of hydrolysis and polymerisation reactions to form a colloidal suspension called “sol”. Thin films can be produced on substrate by spin-coating or dip-coating. When the “sol” is cast into a mould, a wet “gel” will form. With further drying and heat-treatment, the "gel" is converted into dense ceramic or glass articles. If the liquid in a wet “gel” is removed under a supercritical condition, a highly porous and extremely low density material called “aerogel” is obtained. As the viscosity of a “sol” is adjusted into a proper viscosity range, ceramic fibres can be drawn from the “sol”. Ultra-fine and uniform ceramic powders are formed by precipitation, spray pyrolysis, or emulsion techniques[14].

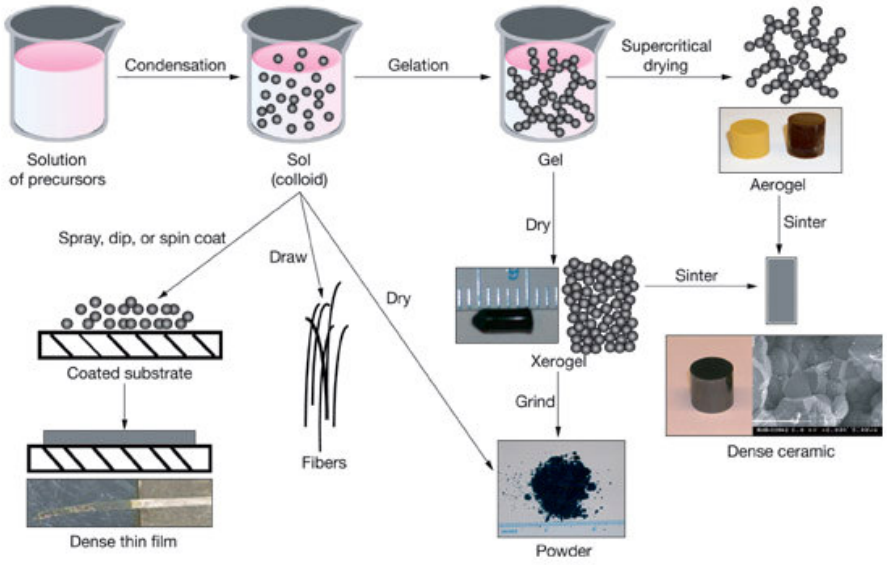

Fig. 2.7 – Sol-gel processes allow to obtain a great variety of products

2.2 Pulsed Electron Deposition (PED)

A critical component in thin films growth development is the deposition technique and the methodology chosen.

As it has been written in previous paragraphs, a great number of deposition technique can be used for multi-layer thin films devices.

In particular PLD, thanks to the nature of the pulsed energy flux supplied to the target, provides very high degree of stoichiometric fidelity in the deposited film leading to

excellent material properties. Indeed, pulsed energy techniques permit unique material processing technology. The short pulse length (about 10-100 ns) facilitates high power density at the target surface where the short penetration depth of the beam generates rapid non-equilibrium heating processes, forming a high direct, stoichiometric plasma plume[15]. Even though this is a remarkable feature, from the point of view a large scale and commercial production of thin films-based devices, excessive costs reduce the effectiveness of this technique. Thus, it is necessary to find a technology allowing both high performance deposition characteristic and low running and installation costs. These features can be achieved by the Pulsed Electron Deposition, where the energy carriers are electron and not photon as in PLD.

The first results obtained by a fast-low pressure gas discharge was reported in 1979[16]. The low pressure gas discharge occurs between a planar anode and a hollow cathode specially designed for particular and unique charged particle emission characteristics[17]. This relatively simple design was called pseudo-spark process. The energy beam is formed by electrons generated in a plasma inside a hollow cavity and driven trough a background gas.

Afterwards, in a novel prototype of PED system called Channel Spark, new accelerator parts were designed allowing higher conversion efficiency of electrical energy stored was reached: 30% against only 4% of pseudo spark discharge.

Despite the operation principle based on electrons, the focussing system is not so complicated as in electron microscope and magnetic lens are absent in PED equipment. In practice the pinched electron flux extracted by the plasma passes trough a little hole and is driven into 4-6 mm diameter glass or alumina tube towards the target. The acceleration of the electrons is induced by a high potential difference applied between the hollow cathode and the target holder (ground).

The electrical energy is stored in a variable number of high voltage ceramic capacitors which can deliver about 3-5 J/pulse. The discharge is activate by an external trigger circuit, the frequency of which can be simply adjusted by the operator.

The possibility to obtain an electron beam as small as several mm^2 in size permits very high current density in the beam (about 10^6 A/cm^2) and subsequently very high power density (up to 10^9 W/cm^2) with a pulse duration of about 100 ns onto the target surface[18].

2.2.1 Electrons generation and acceleration

The hollow cathode is a metal tube located in front of the anode and electrons are generated at its inner walls by means of ion impact or photo effect. The cathode operates in DC mode and the reduced electric field inside makes the electrons move slowly increasing the number of collision and ionization.

For very high current the hollow cathode is modified to operate in pulsed mode and it is called transient hollow cathode, consisting of a similar cathode only with a narrow exit which focus electron flow. In this case a trigger circuit is present to control discharge voltage and to ignite the plasma[19].

The acceleration system designed for PED is the main difference between pseudo-spark and channel-spark discharge and that is the reason of the efficiency improvement realized by the latter over the former technique. In pseudo-spark discharge, the electron acceleration is affected by a sequence of parallel electrodes separated by insulators. The arrangement of hollow cathode and electrodes leads to an electric field gradient that focuses the electrons along the central axis. The discharge occurs in the high voltage and low pressure of the Paschen curve[17] where, at a given breakdown voltage le low pressure discharge became a spark-like discharge characterized by a high current flow that rises according to an exponential function[20]. An intense pulsed electron beam is formed along the central axis and it is extracted from the cavity through the narrow opening.

The current density of this beam is about 5000 A/cm^2 with a pulse width of 100 ns (**tab. 2.1**).

Although good results has been obtained with pseudo-spark discharge, lots of problems about the stack of electrodes remained unsolved. The metal discs were subject to oxidation, changing the properties of the discharge over a relatively short period and requiring a frequent disc cleaning as a routine maintenance. Thereby, to overcome these difficulties a new scheme based on a dielectric channel was projected to replace the sequence of metal and insulator discs. This brought a great advantage in the stability of the electron beam and therefore a more effective energy transfer from the beam to the target up to 7-8 times higher than in the case of pseudo-spark discharges[21]. The pulsed nature of the energy source facilitates the ability to deposit complex metal oxides such as HTS conductors or

doped materials. Remarkable results are reported in the last years also for CIS[22], CIGS[23] and ZnO[24] thin films deposition for photovoltaic applications using PED systems.

Maximum discharge voltage	25kV (some prototype can reach 40kV)
Electrical efficiency	30%
Stored energy	3-5 J
Gas pressure	$1*10^{-3} – 5*10^{-2}$ mbar
Discharge time	About 100 ns
Repetition rate	1-10 Hz
Electron current	1,5 kA
Electron beam diameter at the target	2-3 mm
Maximum beam current density	10^5 A/cm^2
Power in the beam	15 MW
Power density in the beam	500 MW/ cm^2

Tab. 2.1 – Typical pulsed electron beam parameters [25]

2.2.2 Interaction between electron beam and target

When a high power density energy beam hit the solid surface of the target, the energy is absorbed by the surface and a rapid increase of the temperature occurs, generating a fast evaporation of the material and the formation of the plume composed by ablated material.

The reliability of this process critically depends on the amount of energy absorbed by the plasma plume rather than the target. This is a typical issue for PLD related to 2 main reasons: the amount of ablated material is very sensitive to the optical absorption coefficient of the target material and the plume steals a remarkable quantity of energy from the beam. In this second case the beam cannot reach the surface or it hits the target with too low energy to ablate it because the plume behaves like a shield.

In PED, ablation is independent from the optical properties of the target materials because the beam-solid and beam-plume interactions are quite different from PLD. In PED technique, initial heating of the surface is controlled by the balance of the heat-in flow via beam energy dissipation and the heat-out flow via thermal and electrical conductance of

the target material. A very high surface temperature is reached by the inelastic collision among electrons of the beam and target atoms. After a short path inside the target, a great part of energy is lost by electron for Coulomb interactions because of the scattering and the diffusion of the electrons into the material. This effect results in a confinement of the applied accelerating voltage within a 1 μm surface layer. The depth of this region is an order of magnitude greater than the absorption length of laser radiation and allow to evaporate an amount of material at least ten times greater than the typical mass ablated (0,6 μg/pulse) by 193 nm of ArF excimer laser PLD.

As reported in various experiments, the ablated mass is substantially constant for different type of materials if they present the same density (in solid or sintered form) and the same thermal conductance because the main parameter to control is the electron range in which it is actually effective and it strongly depends from the target properties. Hence, target preparation is fundamental to obtain excellent conditions of deposition rate and stoichiometry in material transfer.

2.2.3 Plume propagation

Generally in high pulsed energy ablation, the plasma plume generated at the surface of the target after the interaction with the energy beam expands in the direction of the maximum pressure gradient.

In comparison with PLD, in PED system the background pressure must be maintained one order of magnitude lower to avoid uncontrolled auto-discharge phenomena that can influence the deposition rate and the reproducibility of the experiment.

The parameter that we have to consider to understand the expansion mechanism of the plume are: plasma expansion, deceleration and thermalization of ablated material.

A simple model predicts that the optimal target-substrate distance (L_0) depends on number of ablated atoms (N_0) and gas pressure (P) following the equation below[26]:

$$L_0 \approx \left(\frac{N_0}{P} \right)^{1/3} \qquad \text{(Eq. 2.1)}$$

By this formula a very interesting information can be extracted about the optimal distance to grow thin films with a reasonable thickness uniformity onto 5-6 cm diameter substrates.

In spite of the PED simple apparatus, the basic phenomena and the physics of the discharge are not completely understood. Temporal and spatial development of the discharge have been investigated showing a very complex dynamics of the processes involved. Spectroscopic studies report some interesting data on the plasma plume composition revealing a high degree of ionization inside characterized by a lower kinetic energy than that observed in PLD plasma plume. This can be explained by some experiments that have been carried on to study energy distribution of electron beam reporting that the pulse consists of electron of different energies and only the leading edge contains the most energetic electrons. This energy distribution seems to be the cause of potential problem noticed in PED thin films growth: the generation of particulates that interfere with optimal film growth. The influence of ambient pressure and accelerating potential on the number and size of particulates appearing on the surface of films was investigated for the barium fluoride-based YBCO precursor process. It was found that the size of the particulates varies exponentially with accelerating voltage; it can be reduced to less than 100 nm by increasing the ambient pressure beyond that required for optimum deposition rate[27]. Other recent studies on different complex compounds such as, ZnO, $Ca_3(PO_4)_2$, $Ca_{10}(PO_4)_6(OH)_2$, $Zr_{0,8}Sn_{0,2}TiO_4$ and $Ba_xSr_{1-x}TiO_3$ confirmed that PED can lead to films free from micrometer size droplets and by a careful optimization of the beam parameters and beam-source components, it is possible to drastically reduce the density and size of nanoparticulates[28].

The possibility to control the formation of particulates could make PED useful for technical applications where the generation of sub-micron sized materials is desired.

2.3 PED installed @ IMEM-CNR laboratory

Integration of pulsed electron-beam source in a film growth deposition chamber is relatively simple because the system is flange mounted and integrated with a standard deposition chamber thanks to its reduced dimensions and easy handling.

Usually, the angle between the linear axis of the beam and the normal to the target surface is around 45° to optimize the impact onto the target with the minimum shadowing effect due to the tube guide for electron flux. The self focusing electron beam is guided to the target by a glass tube with inner diameter of 2-4 mm depending on the material to growth. Alumina or pure quartz can be used when high deposition temperature is necessary.

The target holder is a copper cylinder on which the target is fixed with Ag-based paste or locked with a stainless steel ring screwed on.

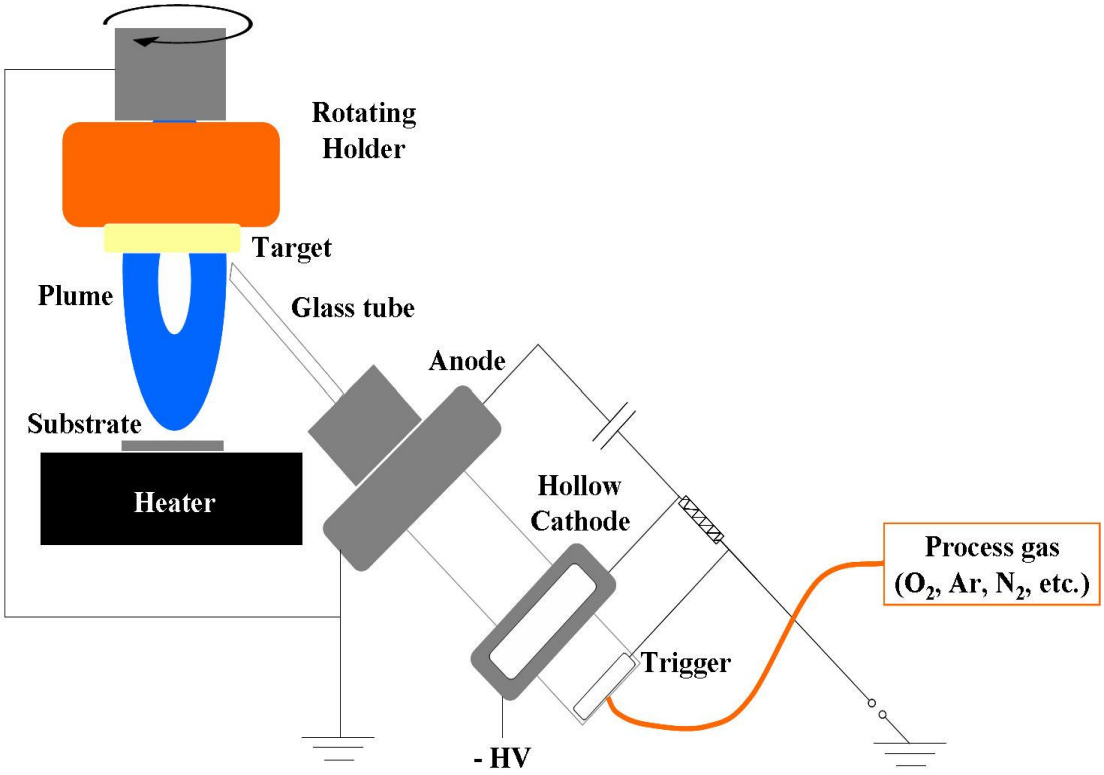

Fig. 2.8 – PED scheme of the system installed at the IMEM-Cnr laboratory

The electron source has been installed on a deposition chamber designed in our laboratory and realized by RIAL Vacuum s.p.a. for thermal evaporation of High Temperature Superconductor (HTS) to realize Coated Conductors (CC) for high efficiency energy devices.

In **fig. 2.9** the apparatus installed at IMEM is presented. It consists of three vacuum chambers connected each other in such a way that a flexible tape can move for different treatments under different conditions[29]. In details: in the first chamber the annealing

process in reducing atmosphere (forming gas, F.G.) takes place, needed to clear and reduce the eventually oxides present on the substrate surface. This chamber in equipped with an Alcatel turbo-molecular pump (400 l/s) to remove H_2O vapour inside and a IR-lamps heater opportunely designed to keep a uniform 700°C temperature along 60 cm. The second deposition chamber was first designed to host a thermal evaporation system; its large site is recommended to facilitate the operations inside and exploit the maximum deposition area typical of this technique. Following the PED installation, the old 8 IR-lamps heater has been removed and smaller one has been mounted. Also this heater has been designed in our laboratory and it is composed by a graphite block under which there are 2 IR lamps placed onto a water cooled stainless steal support. The vacuum system is composed by a water-cooled Pfiffer turbo-molecular pump (1200 l/s). The third chamber is necessary to perform the post-deposition process. Originally, it has been thought for the oxygenation of oxide compound but the substitution of the gas supply can be easily changed. This is the smallest of the three chambers because, usually, the post-deposition process is the faster among the others. The external chambers are equipped with the same vacuum system of the first one to allow a clean ambient for the process and to remove the aqueous vapour present inside. Also the heater is the same present in the first chamber but smaller for the short-time process occurring there.

Thanks to the differential vacuum system and the special interconnections between the deposition chamber and the external ones, a high difference of pressure (up to 6 order of amgnitude) can be kept avoiding the vacuum break during the substrate movement.

The substrate used for CC is a 80 μm thick metal tape of Ni-based alloy and two rolling pulleys positioned at the extremities pull the tape through the three chambers. The movement is assured by 2 step-by-step motors controlled by a home made circuit placed in the rack.

The PED gun has been installed on the door of the central chamber. Trigger circuit and frequency regulation device gas control and just under the chamber (**fig. 2.9**). This is important because it allows a short path to the gas from the valve to the gun, rendering very fast the effect of the pressure regulation on the plasma discharge and subsequently on electron flux. are located under the deposition chamber, too.

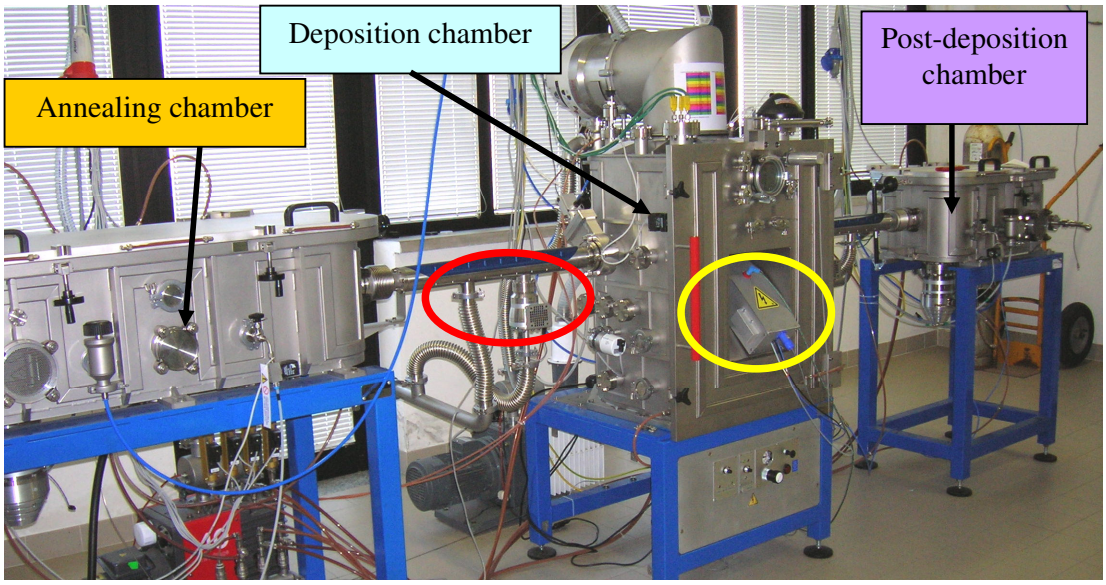

Fig. 2.9 – The three chamber apparatus for multi-layer deposition [29], with the pulsed electron beam source flanged on the front door of the deposition chamber in the yellow circle. In the red one the differential vacuum system mounted on the special interconnections between the chambers

High voltage power supply to accelerate the electrons is placed into an external rack while under the central chamber are positioned the trigger control and the gas-flow control to provide the necessary amount of gas to ignite the plasma in the hollow cathode. In this system one can use different type of reactive gas (N_2, O_2, mixture of Ar and H_2, etc.) to provide the optimal background atmosphere. Major detail will be presented in the next chapters.

References

[1] A. Mubarak, E. Hamzah, M. R. M. Toff: "Review of physical vapour deposition (PVD) techniques for hard coating", *Jurnal Mekanikal*, 20, (2005) pp. 42-51

[2] K. Wasa, M. Kitabatake, H. Adachi: "Thin Films Material Technology: Sputtering of Compound Materials", Springer (2004)

[3] M.Ohring: "Material Science of thin films: deposition and structure", Academic Press, USA (2002)

[4] Electron beam evaporation, http://www.tungsten.com/tipsbeam.pdf

[5] Basics of Molecular BeamEpitaxy (MBE) – Lessons of Fernando Rinaldi

[6] R.A. Swalin, "Thermodynamics of solids", John Wiley & Sons, New York, (1972)

[7] S. J. Benerofe; C. H. Ahn; M. M. Wang; K. E. Kihlstrom; K. B. Do; S. B. Arnason; M. M. Fejer; T. H. Geballe; M. R. Beasley; R. H. Hammond: "Dual beam atomic absorption spectroscopy for controlling thin film deposition rate", *Journal of vacuum science & technology. B. Microelectronics and nanometer structures. Processing, measurement and phenomena*, **12** (1994) pp. 1217-1220

[8] G.B.Stringfellow, Organometallic Vapour-Phase Epitaxy: Theory and Practice, Academic Press, London (1989)

[9] R. K. Singh and D. Kumar, "Advances in Pulsed Laser Deposition of Thin Films", Kluwer publishers, (1998)

[10] Pulsed Laser Deposition (PLD), http://pulsedlaser.net

[11] G. M. Blom, S. L. Blank, J. M. Woodall: "Liquid Phase Epitaxy" North-Holland, (1974)

[12] P. Y. Yu, M. Cardona. "Fundamentals of Semiconductors: Physics and Materials Properties", Springer (2005)

[13] J.D. Wright, N.A.J.M. Sommerdijk: "Sol-Gel Materials: Chemistry and Applications", CRC (2001)

[14] S. Sakka, "Handbook Of Sol-gel Science And Technology: Processing, Characterization, And Applications", Kluwer Academic Pub (2004)

[15] D.C. Paine and J.C. Bravemen: "Laser ablation for material Synthesis", Mater. Res. Soc. Proc. (1990)

[16] J. Christiansen and C. Schultheiss, *Z. Physic A,* **290** (1979)

[17] F.C. Matacotta and G. Ottaviani: "Science and technology of thin films" (1995) World Scientific

[18] C. Schultheiss, F. Hoffman, *Nuclear instruments and methods in physic research B,* **51** (1990)

[19] K. Mittag, P. Choi, Y. Kaufman, *Nuclear instruments and methods in physic research A,* **292** (1990)

[20] M. Hoebel, J. Geerk, G.Linker and C. Schultheiss: "Deposition of superconducting YBCO thin film by pseudo-spark ablation" , *Applied Physics Letter,* **56** (1990)

[21] Q.D. Jiang, F.C. Matacotta, M.C. Konijnenberg, G. Mueller and C. Schultheiss: "Deposition of $YBa_2Cu_3O_{7-x}$ thin films by channel-spark pulsed electron beam ablation", *Thin Solid Films,* **241** (1994)

[22] A.M. Andriesh, and V.I. Verlan: "Preparation of $CuInSe_2$ by e-beam ablation technology andproperties of thin films - solar cell components", *Semiconductor Conference, 2001. CAS 2001 Proceedings. International,* **1** (2001)

[23] A.M. Andriesh, V.I. Verlan, L.A. Malahova: "Controllable deposition of CdS, CIGS and heterostructures thin films by means of e-beam ablation technology", *Semiconductor Conference, 2003. CAS 2003. International,* **2** (2003)

[24] H. L. Porter, C. Mion, A. L. Cai, X. Zhang, J. F. Muth: "Growth of ZnO films on C-plane (0001) sapphire by pulsed electron deposition (PED)", *Materials science & engineering. B, Solid-state materials for advanced technology,* **119** (2005)

[25] A. Goyal: "second generation HTS conductors", kluwer Academic Publishers (2005)

[26] M. Strikovsky, J.H. Miller, *Applied Physics Letter,* **73** (1998)

[27] J.E. Mathis and H.M. Christen: "Factors that influence particle formation during pulsed electron deposition of YBCO precursors", P*hysica C: Superconductivity,* **459** (2007)

[28] M. Nistor, N.B. Mandache and J. Perrière: "Pulsed electron beam deposition of oxide thin films", *J. Phys. D: Appl. Phys.*, **41** (2008)

[29] Bindi M., Canetti M., Gangini F., Gauzzi A., Gianni L., Gilioli E., RampinoS. and Zannella S.: "Multi-chamber deposition system for continuous production of YBCO coated conductors by thermal co-evaporation", *Journal of Physics: Conference Series* (2006) **43**

HTS-Coated Conductors for energy applications

Introduction

The discovery of high temperature superconductivity (HTS) in the family of copper oxides by Bednorz and Müller[1] has been one of the main interesting discover in the history of physics renewing the interest in superconductivity. The most appealing property of HTS materials is their much higher critical temperature, Tc ~ 100 K as compared to the range of low temperature superconductors (LTS, such as Nb, NbTi or Nb_3Sn) with Tc ~ 10 K and sufficiently high to operate in superconductor regime in liquid Nitrogen (T_l = 77 K) which is much less expansive than liquid Helium. Secondly, epitaxially grown HTS films show very high current density, Jc (exceeding $5x10^6$ A/cm^2 in self-field, at 77 K)[2]. However, unlike the most widely used LTS material, all HTS materials are brittle and difficult to process. To face this difficulty, since the discovery of first HTS in 1987 YBCO[3], a lot of efforts and significant progresses have been made to realize long tapes for power and electronic applications.

3.1 History of superconducting materials

In 1911 superconductivity was first observed in mercury by Heike Kamerlingh Onnes. When he cooled it to the temperature of liquid helium at 4 K (-269 °C), its resistance suddenly disappeared. He soon discovered that a superconducting material can be returned to the normal state either by passing a sufficiently large current through it or by applying a sufficiently strong magnetic field[4].

The next great milestone in understanding how matter behaves at extreme cold temperatures occurred in 1933. German researchers Walter Meissner and Robert Ochsenfeld discovered that a superconducting material will repel an external magnetic field. It is well known that a magnet moving by a conductor induces currents in the conductor and this is the fundamental principle for electric generation. But, in a superconductor the induced currents exactly mirror the field causing the repulsion of the magnet. This phenomenon is known as strong diamagnetism and is today often referred to as the "Meissner effect". The Meissner effect is so strong that a magnet can actually be levitated over a superconductive material.

After the pioneering work of Onnes, Meissner and many other researchers, in subsequent years other superconducting metals, alloys and compounds were discovered. In 1941 Niobium nitride was found to superconduct at 16 K. In 1953 Vanadium-Silicon displayed superconductive properties at more than 17 K and, in 1962, scientists at Westinghouse developed the first commercial superconducting wire, an alloy of Niobium and Titanium.

The story changed dramatically in 1986, when J. Georg Bednorz and K. Alex Müller produced a new material with the formula La_2CuO_4 with a crossover temperature of 35 K. This appears different from the previous classes of material because it has a complex crystal structure made from several components, based around copper oxide units. This discovery earned Bednorz and Müller a Nobel prize, and was followed a year later by the discovery, achieved by Paul Chu and colleagues, of another material with the formula $YBa_2Cu_3O_7$ (often abbreviated to YBCO or 123 from the ratio of metal atoms in the structure) which had an even higher threshold temperature of around 92 K. This meant for the first time that a material exhibited superconducting behaviour at temperatures above that of liquid nitrogen (77 K), which is much cheaper and easier to handle than liquid He, necessary for low temperature superconductors discovered before.

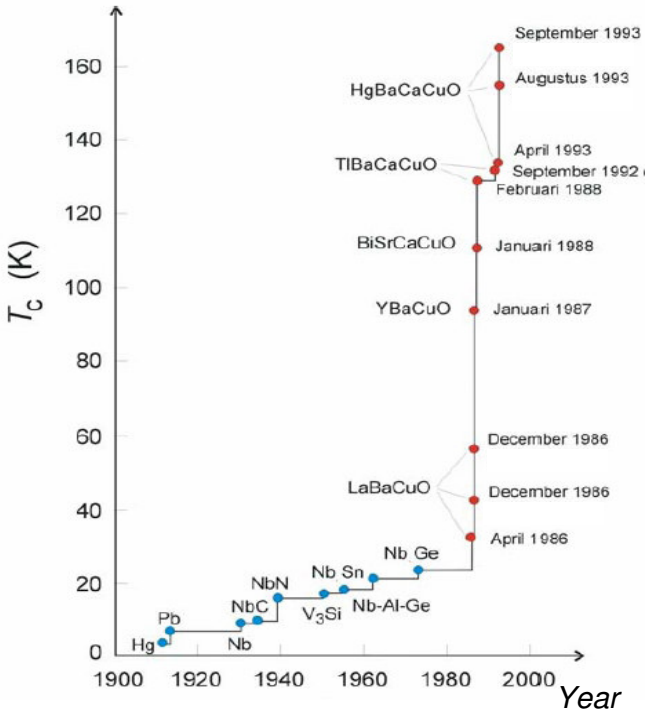

Fig. 3.1 – Superconducting materials discovered in 20th century

3.2 Properties of Superconducting materials

As the name suggest, the most important and evident property of this type of material is related to their ability of reaching a conducting state without any type of resistance under particular conditions of low temperature.

Superconductivity is a startling departure from the properties of normal conductors of electricity. In electric conductors, the external electrons of atom shells are not bound to individual cores but are free to move through the material; their motion constitutes an electric current when a potential is applied. In normal conductors these so-called conduction electrons are scattered by impurities, dislocations, grain boundaries, and lattice vibrations (phonons) due to the temperature (**fig. 3.1**).

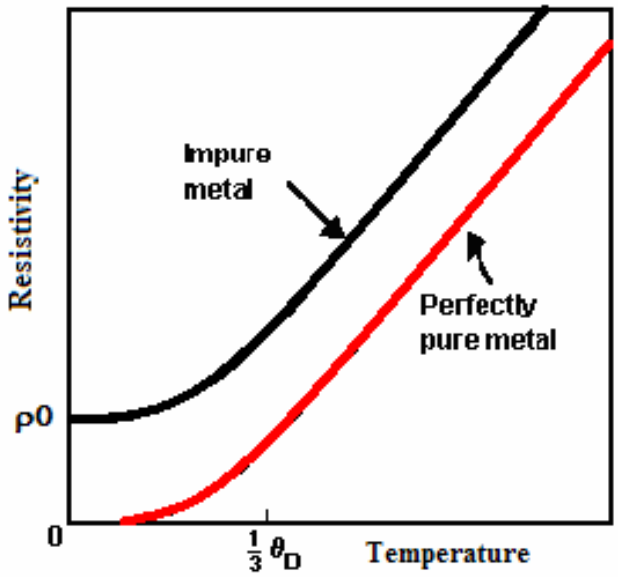

Fig. 3.1 – Impure and perfectly pure metal resistivity behavior vs. Temperature [5]

For a normal metal, the behaviour of resistivity, ρ, versus temperature, *T*, follows the Matthiessen's law written below:

$$\rho(T) = \rho 0 + \rho i\ (T) \qquad \text{(Eq. 3.1)}$$

where $\rho 0$ is a non-zero value in presence of impurities and the second term, ρi, derives from the scattering between electrons and phonons. Above a certain value of temperature

related to the Debye one θD, $\rho(T)$ increases linearly with temperature, following an exponential T^5 law[6].

In a superconductor, however, there is an ordering among the conduction electrons that prevents this scattering. Consequently, under the critical temperature (Tc) of a superconductor, electric current can flow with no resistance at all (**fig. 3.2**).

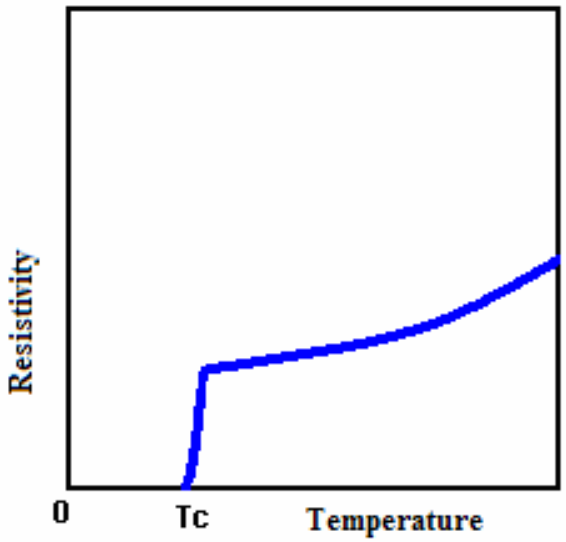

Fig. 3.2 – Superconductor resistivity behavior vs. Temperature [5]

This particular behavior is due to a formation of electron pairs known as “Cooper pairs”. The mechanism by which two negatively charged electrons are bound together is still controversial in "modern" superconducting systems such as the cuprates or alkali metal fullerides, but well understood in conventional superconductors (i.e. aluminium) in terms of the mathematically complex BCS (Bardeen Cooper Schrieffer) theory[7].

The BCS theory is based on the fact that the interaction between electrons resulting from virtual exchange of phonons is attractive when the energy difference between the electrons states involved is less than the phonon energy.

Below Tc the binding energy of the electron pairs causes the opening of a gap in the energy spectrum at the Fermi level (i.e. the highest occupied level in a solid) separating the pair states from the "normal" single electron states.The electrons are bound together by their interaction with the vibrations of the underlying lattice: one electron in the pair

polarizes the lattice by attracting the nuclei towards it, leaving a region of excess positive charge (a potential well) into which a second electron is attracted: the positively charged nuclei thus mediate an attraction between the negatively charged electrons. Only electrons within the vibration frequency, characteristic of Fermi Energy (E_f), can be paired by this interaction, and only a small fraction of the electrons become superconducting (**fig. 3.3**).

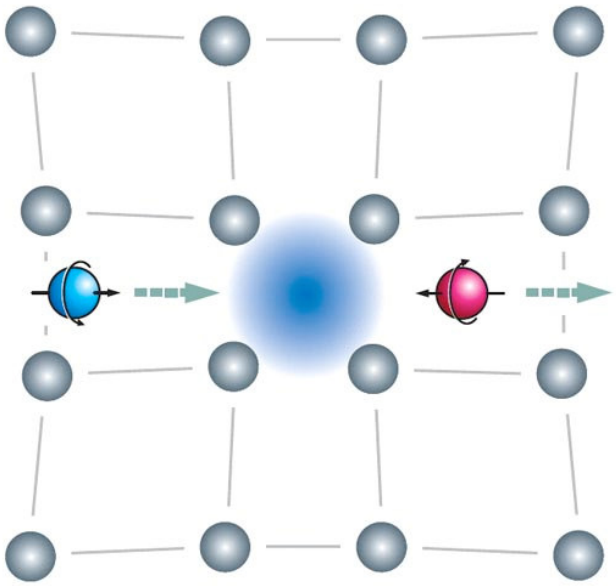

Fig. 3.3 – Model of Cooper pairs formation

The pair formation is a process where two fermions (the free electrons) are considered as a single boson (the Cooper pair) that can condense in to the same energy level making a superfluid-like system responsible for the superconducting properties. Until this quantum state is maintained, it is coherent and with the lower energy for the system that implies there is not energy dissipation by charge transport.

The wave function describing all the Cooper pairs, varies in a distance given by a parameter called coherence length, characteristic of the material. The coherence length indicates the size of a Cooper pair representing the shortest distance over which superconductivity can be established in a material. This is typically on the order of 1000Å; although it can be as small as 30Å in the copper oxides.

Another difference between typical superconductors (Type 1) and cuprates or other complex superconductors (Type 2) is the diamagnetic behaviour they show once applied an

external magnetic field. The parameter defining these groupings is the penetration depth that relates to how deeply a magnetic field will penetrate the surface of a Type 2 superconductor. The field inside the material will decay exponentially into the surface depending on the paired electron density within the superconductor according to the London low. On the contrary a Type 1 superconductor present a perfect diamagnetism and it completely expels the external magnetic field under a critical value Hc (Meissner effect)[8]. The expulsion of the magnetic field is accomplished by shielding supercurrents which flow at the surface of the superconductor without any Ohmic losses. Above the Hc, the material loses its superconducting properties, becoming a normal conductor, even below the critical temperature (Tc) (**fig. 3.4**).

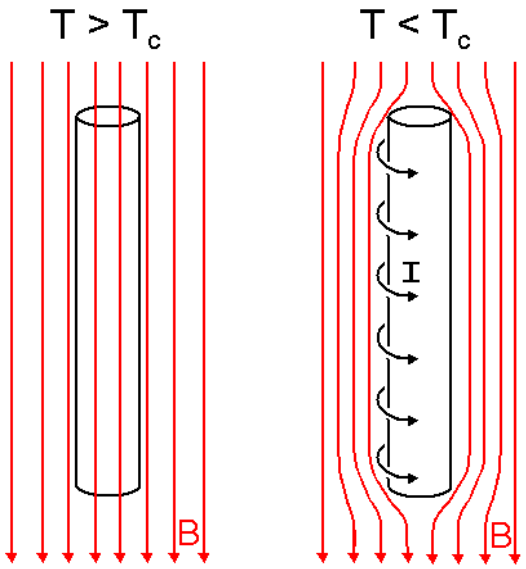

Fig. 3.4 – Magnetic field expulsion by shielding supercurrent on the surface in Type 1 superconductor

For a Type 2 superconductor two critical induction fields, Hc1 and Hc2, exist. Below the critical temperature, T < Tc, the magnetic field is totally excluded from the material only below Hc1 (Meissner State). In this state a Type 2 superconductor behaves as a Type 1 one below is typical Hc. Between the two critical fields, magnetic flux starts to penetrate into the material without affecting the superconducting state (mixed state). When the applied field exceeds the Hc2 value, the material becomes a normal conductor, as the Type 1 one above his Hc.

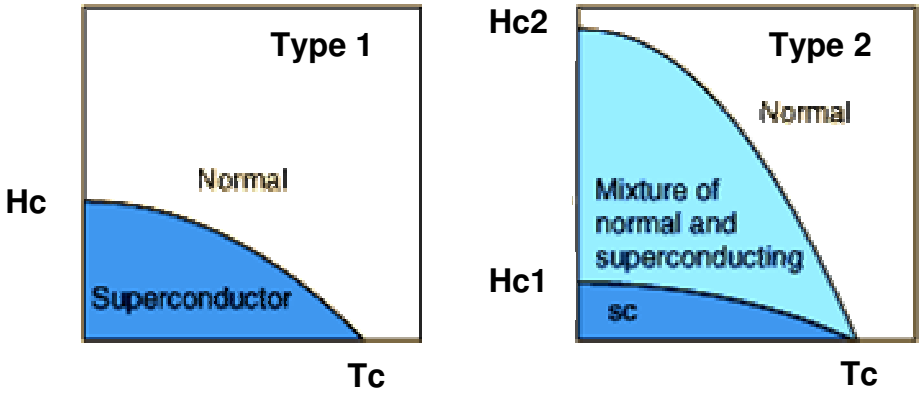

Fig. 3.5 – Type 1 and Type 2 superconductor phase diagram (magnetic field vs. temperature)

In the mixed state magnetic flux can penetrate the superconductor in form of filaments arranged in a periodic array[9]. At the vortex centre where the magnitude of the local field is largest, the density of superconducting electrons n_s is zero (**fig. 3.6**).

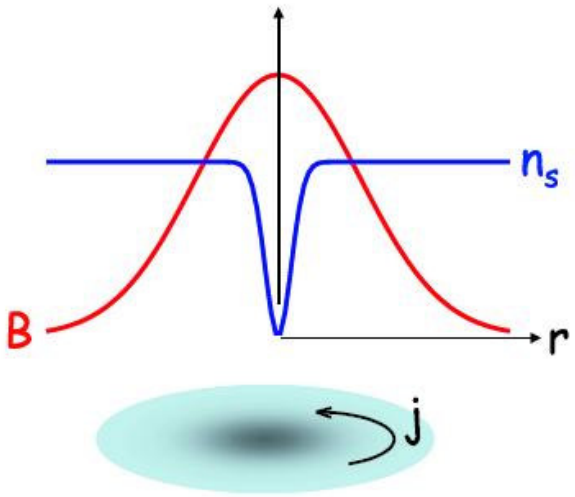

Fig. 3.6 – Magnetic field and density of superconducting electrons into the flux vortex

As one moves radially out from the centre of a vortex core, n_s increases and the supercurrents screen a greater amount of flux. At a radius on the order of the coherence length, n_s approaches the value in the bulk of the sample. Outside of the vortex core, magnetic field vanishes into the superconducting regions of the sample. In a perfect superconducting material, vortices arrange in a triangular lattice, known as Abrikosov lattice, in order to minimize the electrical repulsion between themselves. Moreover, a real

motion of the vortices through the superconducting material has been observed while a current flows in the material if there are no impurities or defects. This phenomenon is caused by the Lorentz force generated by the contemporary presence of a magnetic field and moving charge carriers. Every moving vortex generates an electric field interacting with the current flux and a consequent energy dissipation. It is also clear from such experiments which verify the flux quantum that it is energetically more favourable to increase the number of vortices enhancing the magnetic field rather than increasing the amount of flux in each vortex[10].

In a concrete material vortices cannot freely move through the sample because they encounter lots of pinning centre such as impurities, lattice defects and secondary phases. These objects are often useful to minimize the energy dissipation inside the material preventing the vortices from moving too much.

3.3 High Temperature Superconductors (HTS)

The partial penetration of the magnetic flux into the material in very high magnetic fields makes Type 2 superconductors the only candidates for power applications. Low-Tc Type 2 superconductors (LTS) wires carrying very high current density have been fabricated since the second half of the last century for the production of high field superconducting magnet working at Helium boiling point (4,2 K). However the discovery of HTS opened a wide area of interest for superconductivity in power applications thanks to the possibility of using liquid Nitrogen rather than the much more expansive liquid Helium. HTS materials are Type 2 superconductors based on copper oxides, with a Tc of about 100 K. Starting from the compound discovered by Bednorz and Muller, several materials have been found HTS from 1986. One of the compounds more deeply studied is $YBa_2Cu_3O_{7-\delta}$ (YBCO or 123), with Tc = 92 K. This temperature is high enough to enable the employ of liquid nitrogen (77 K) as cooling fluid, thus widening its utilization for power applications. Whereas the BCS theory has been very successful in describing conventional LTS materials assuming that electrons are coupled via electron-phonon interaction to form Cooper pairs, different theories have been proposed for the pairing mechanism in HTS but this issue remains highly controversial. Recent surveys hold that it relates to the planar

layering within the crystalline structure and researchers suggest the holes, considered like positively-cherged vacancies within the lattice, of hypocharged oxygen in the charge reservoirs are responsible of the superconducting behavior.

The first superconducting Type-2 compound, an alloy of lead and bismuth, was fabricated in 1930 by W. de Haas and J. Voogd, but it was not recognized as such until later, that is after the Meissner effect discovery. The first oxide superconductors was created in 1973 by DuPont researcher Art Sleight when $Ba(Pb,Bi)O_3$ was found to have a Tc of 13 K. Then, in 1986, a truly breakthrough discovery was made in the field of superconductivity. Alex Müller and Georg Bednorz, researchers at the IBM Research Laboratory in Rüschlikon, Switzerland, created a brittle ceramic compound that superconducted at the highest temperature then considered possible: 30 K[1]. What made this discovery so remarkable was that ceramics are normally insulators and until then, researchers had not considered them as possible high-temperature superconductor candidates. The Lanthanum, Barium, Copper and Oxygen compound ($La_{2-x}Ba_xCuO_4$) that Müller and Bednorz synthesized, behaved in an unusual way. The discovery of the first superconducting copper-oxides (a family called then cuprates) won the 2 men the Nobel Prize the following year. It was later found that tiny amounts of this material were actually superconducting at 58 K, due to a small amount of lead, making the discovery even more noteworthy. So, researchers all over the world began doping and working on copper-based ceramics to reach higher and higher Tcs. In 1987, as it has been mentioned, in a research team at the University of Houston substituted Yttrium for Lanthanum in the Müller and Bednorz molecule and achieved the incredible value of 92 K Tc[3]. That was the first time a material (today referred to as YBCO and probably the most studied HTS compound) had been found superconducting at temperatures warmer than liquid nitrogen, cheaper than liquid Helium, easily handled and commonly available coolant. Additional milestones have been achieved using often toxic elements in the base perovskite ceramic. The current class of ceramic superconductors with the highest transition temperatures are the mercuric-cuprates. The first synthesis of one of these compounds was achieved in 1993 at the University of Colorado with the formula $HgBa_2Ca_2Cu_3O_8$[11]. The world record Tc of 138 K is now held by a thallium-doped, mercuric-cuprate compound based on various toxic elements $(Hg_{0,8}Tl_{0,2})Ba_2Ca_2Cu_3O_{8,33}$ and under extreme pressure its Tc can be increased up to 166 K.

The materials under discussion belong to the class of ionic perovskite and they all present CuO_2 planes stacked in different manner. Cuprates are variations of the crystal type known as perovskites. Perovskites are well-known minerals whose chemical formula is ABX_3. Thus, perovskites contain three elements A, B and X in the proportion 1:1:3. Atoms A are metal cations, atoms B and X are nonmetal anions. Element X is often represented by oxygen. In general, the high temperature superconductors are materials with basically tetragonal structure, and all of them have one or more CuO_2 planes in the **a-b** plane. Superconductivity in cuprates occurs in this copper-oxide planes. The CuO_2 layers are always separated by particular blocks containing other atoms such as Bi, O, Y, Ba, La etc., which provide the charge carriers into CuO_2 planes. These layers are often called "charge reservoirs" and they strongly influence the critical temperature Tc. The latter correlates with the number of CuO_2 layers, for example, at fixed doping level (i.e. the number of oxygen atoms in the structure), by increasing the number of CuO_2 layers (N), Tc first increases, reaching the maximum value and then decreases. The same behavior is more or less universal in cuprates, where the variable can be the doping level, N, the lattice constants **a**, **b** or **c**. Hence, the maximum Tc value can only be achieved when all the necessary parameters have their optimal values (**fig. 3.7**).

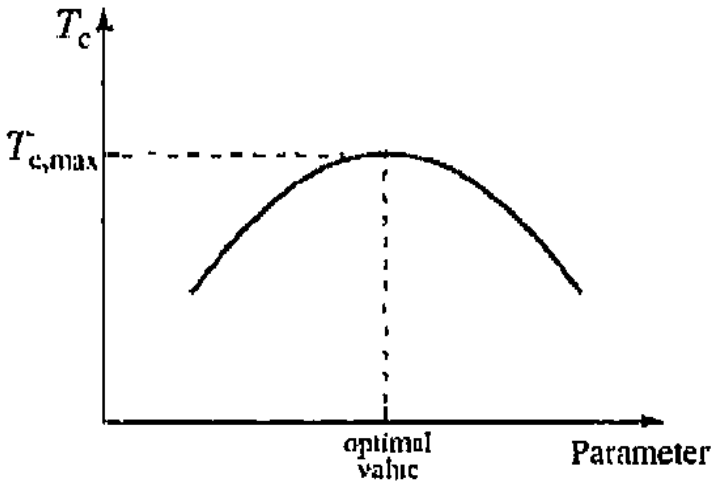

Fig. 3.7 – Critical temperature as a function of the doping level, N or lattice constants (parameter)[12]

3.4 $YBa_2Cu_3O_x$ compound

3.4.1 Structural properties

YBCO, which is commonly termed "123", is the first superconductor found to have Tc > 77 K. The first prperty noted by everyone is the non-stoichiometric formula of this compound where the presence of oxygen atoms can vary from 6 to 7 almost continuously. The two CuO_2 layers typical for HTS are separated by a single Yttrium atom. The superconducting phase with Tc = 92 K has an orthorhombic structure with a O vacancy located at every CuO plane, along **a**-axis at site (½, 0, 0), causing the Pmmm symmetry. The Y and two Ba ions are stacked along the **c**-axis, and the other O vacancy is in the Y plane. The unit cell parameters are: a = 3.8185 Å, b = 3.8856 Å and c = 11.6804 Å [13].

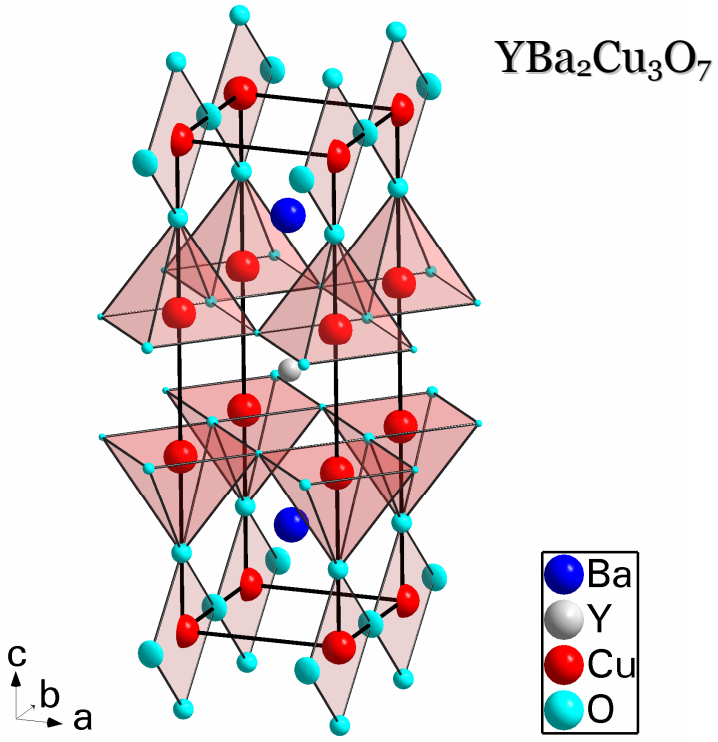

Fig. 3.8 – YBCO perovskite structure shows superconducting CuO_2 planes, CuO chains and BaO planes as charge reservoir blocks

Y ion has a spacing function between the two CuO_2 layers. In the crystal, Y has a valence of +3. The replacement of Y by many of the lanthanide series of rare-earth elements causes no appreciable change in superconducting properties. Each copper ion in the CuO_2 planes

is surrounded by a pyramid of five oxygen ions. Outside the layer CuO_2-Y-CuO_2 layer sandwich are BaO planes and CuO chains. In the crystal, Ba has a valence of +2. The distance CuO in the chains is about 1,9 Å, as it is in the planes. Theorists noticed YBCO is the only high-temperature superconductor compound having one-dimensional CuO chains and came up with a "chain" theory of HTS but later was abandoned. In $YBa_2Cu_3O_6$, there are no CuO chains, and the compound is an antiferromagnetic insulator. Indeed, doping addition or atoms deficiency in the cuprate structure has strong effects on carrier concentration and transport properties, because it affect the copper formal valence, varying the hole concentration in the CuO_2 planes. $YBa_2Cu_3O_6$ must be doped with Oxygen to gradually become a metallic conductor and then a superconductor at low temperature. The doping is achieved by adding oxygen atoms which form the CuO chains. So, the oxygen content can be changed reversibly from 6,0 to 7,0 "simply" by pumping oxygen in and out of the parallel CuO chains running along the **b**-axis. Therefore, the CuO chains play the role of charge reservoirs. Moreover the increase of oxygen content drives the unit cell to reach square symmetry where **a = b**.

At an oxygen content of 6,4 antiferromagnetic long-range order disappears and the superconducting phase starts developing. The maximum value of Tc is achieved at doping level of about 6,95, the optimal value for the doping.

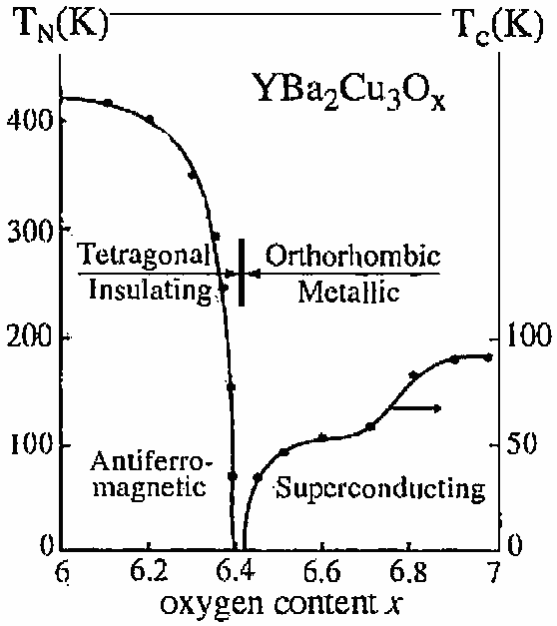

Fig. 3.9 – YBCO phase diagram as a function of the oxygen content between 6 and 7 [12].

Depending on the oxygenation degree, YBCO structure is transformed from a non-superconducting tetragonal phase, with $x < 6,4$ and without CuO charge reservoir chains to an orthorhombic one, called Ortho I, with $x > 6,75$ and almost completely saturated CuO bonds along **b**-axis. Another orthorhombic phase, Ortho II, with lower Tc than the Ortho I one, exists in the intermediate range for x included between 6,4 and 6,75[13]. The carrier concentration in the CuO_2 planes and consequently the YBCO superconducting properties are heavily affected by the number of oxygen atoms in CuO chains.

3.4.2 Electrical properties

Because of the layered structure of the HTS compounds, electrons move easily in some directions, and with difficulty in others. This gives rise to a particular property known as anisotropy. With the raising of Tc from YBCO to BSCCO and thallium compounds also the anisotropy keep on increasing greatly. In concrete terms, a large anisotropy means that electrons can barely move in the **c**-direction, and the superconductor is effectively two-dimensional. This condition of anisotropy was totally obscure to previously known LTS, but with HTS, in which only on the planes of copper oxide the supercurrent flows, anisotropy must be considered with attention. The main difference that researchers noticed was in the coherence length (ξ): LTS present an isotropic coherence length and HTS an anisotropic one. In particular the value of in-plane ξ for YBCO is in the order of the atomic space (ξ **a-b** ~30 Å), while the out-of-plane coherence length ξ **c** is about one tenth of the ξ **a-b** one and results about 4 Å[14].

As we said in the last paragraph, YBCO structure can be seen as a two dimensional superconductor in the **a-b** plane. Hence the critical current density, Jc, can be higher in these planes than along the **c**-direction (Jc **a-b** >> Jc **c**). Another electrical property affected by the anisotropy is the normal state resistivity (ρ). The value of ρ along the **c**-direction is considerably larger than that measured along the **a-b** plane[15]. The in-plane normal state resistivity of HTS material shows a linear metallic temperature, while the out-of-plane resistivity seems to exhibit a semiconducting behavior (**fig. 3.10**).

After these considerations in thin film deposition it is necessary growing YBCO grains with the c-axis perpendicular to the growth direction to obtain high efficiency for power

applications. In this way the current can flow along the a-b planes maximizing the value of critical current density, Jc. Under different circumstances, even a little angle should exist between the c-axis and the direction of growth, the current flow will pass both in the **a-b** plane and along the c-direction, greatly reducing the critical current density value.

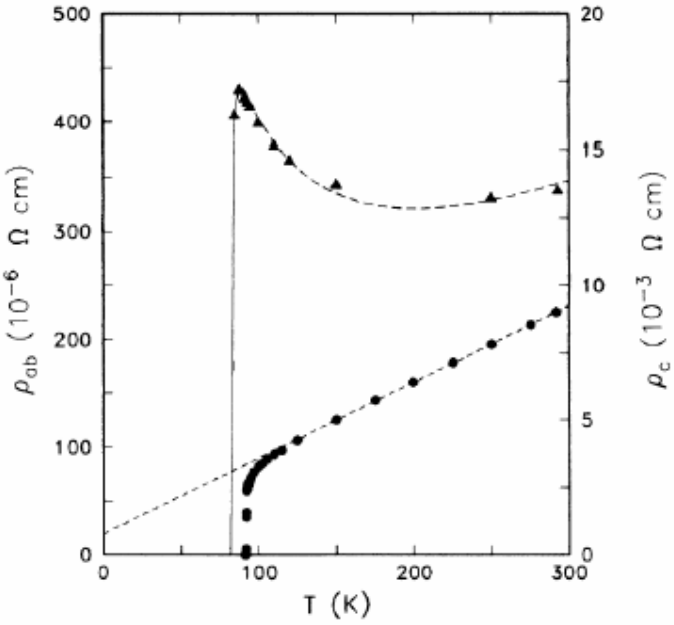

Fig. 3.10 – Anisotropy in electrical properties (resistivity) in different direction of YBCO [16].

For most studies or applications based on cuprates epitaxial films are required, rather than polycrystalline samples containing large-angle grain boundaries. This is due to the fact that generally grain boundaries reduce the Jc of high-Tc superconductors and increase their surface resistance (Rs). Indeed electrical transport properties, Jc, and Rs, depend in different ways on the microstructure and composition of the films. For example, the highest Jc values are obtained in films with a high density of dislocations, which pin vortices, strongly supporting more current before the resistive losses caused by their movement. These pinning sites, however, reduce Tc and it is necessary to reach the best compromise among the properties needed for a specific applications.

Unlike the critical temperature Tc and the critical field Hc_2, Jc is not an intrinsic property of YBCO material. It does not only depends on temperature and on magnetic field, but also on the microstructure of the material. For instance, when YBCO film is in polycrystalline

form, grain boundaries (GBs) are the main limitation for critical current density. Grain boundaries formation is caused by the misorientation between adjacent grains given by the rotation around a particular axis. A tilted low-angle grain boundary is composed by a chain of edge dislocations with Burgers vector, **b**, perpendicular to the GB plane[17,18]. Dislocations induce significant strain fields across the grain boundary, thus locally creating non-superconducting regions[19].

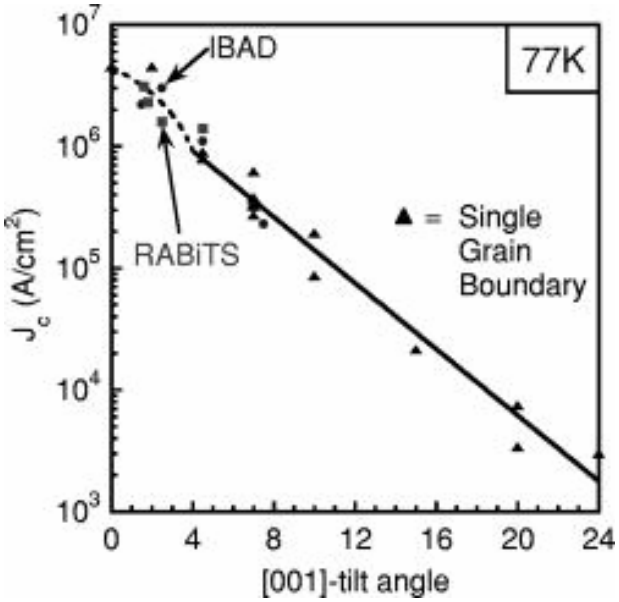

Fig. 3.11 – Jc behavior vs. tilt angle θ around the [001] direction for a YBCO film grown on a SrTiO3 (triangles), IBAD (dots) and a Ni-W cube-textured (squares) polycrystalline coated conductor [20]

3.4.3 Magnetic properties

Another property of YBCO compound is related to its ability to carry very high current in strong magnetic fields. However, in every Type-2 superconductors, the existence of an irreversibility field (H_{irr}), above which superconductivity is lost, has been observed. This field value appears well below the upper critical field Hc_2. In the region of the H vs. T graph between (H_{irr}) and Hc_2, the material shows a non-zero electrical resistance although it still presents a superconductor behavior. The presence of an irreversibility field results from the magnetic field generated by the supercurrent flows which penetrates in the material as flux vortices. Under H_{irr}, the flux vortices are pinned, so they do not create any dissipation. Between H_{irr} and Hc_2 the flux vortices are free to move subject to the Lorentz

force and they originates a further voltage which is the main responsible of the non-zero resistance in the material.

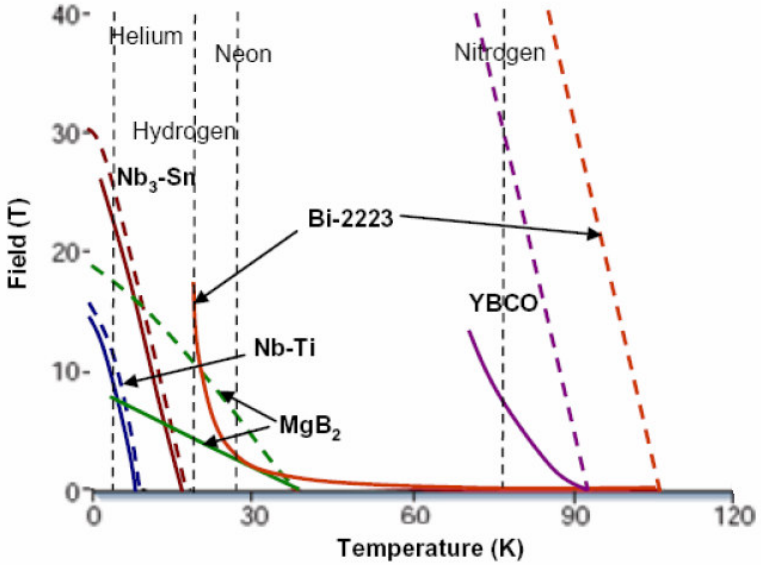

Fig. 3.12 – H_{irr} (dashed lines) and Hc_2 for different type 2 superconductor compounds [21]

The different phase diagrams result from the distinct physical parameters and the crystal structures of these materials. For the isotropic cubic Nb-Ti and Nb_3Sn compounds, H_{irr} is about 0,85 times Hc_2, which is very low. All the other three higher-*Tc* compounds have anisotropic layered structures, which result in significant anisotropy and in all cases the irreversibility line is systematically much lower than Hc_2. The strongly anisotropic Bi-2223 compound exhibits an enormous difference between Hc_2 and the irreversibility field at 77 K (H_{irr} is about 0,2 T, while Hc_2 is of the order of 50 T). Among HTS material, the highest irreversibility field have been found for YBCO compound, due to the small distance between CuO_2 planes. This particular property allows YBCO to be the best candidate for power application and energy transport devices.

3.5 HTS thin films and wires

To obtain polycrystalline YBCO thin films with optimal transport properties two requirements about grain texture are needed. The first one is the *out-of-plane* orientation, that is the film growth with the perpendicular alignment of the c-direction to the substrate

plane, in order to maximize the Jc on **a-b** planes to capitalize anisotropic effect. The second requirement is the *in-plane* orientation, with every grain aligned in the growth plane in order to minimize the presence of high-angle grain boundaries and the consequent current breakdown getting through them. Polycrystalline materials exhibiting such a double grain orientation are said "*biaxially textured*". These characteristics have been the main problems in YBCO tapes production because a reliable thin film process was absent. On the contrary, the Bi-based compounds (BSCCO 2212 and 2223) appeared to be very promising thanks to the large Jc enhancement in granular samples where Ag could be artificially added at the grain boundaries to enhance electric performances. Using this type of Bi-based superconductor multi-filamentary wires can be fabricated by the Powder-In-Tube (PIT) method[22] and they were called first generation tapes. The second generation tapes are called Coated Conductors (CC) and are based on biaxially textured YBCO thin films grown onto metal substrates buffered with layers[23-25].

3.5.1 Bi-based PIT wires

First generation tapes are defined as multi-filamentary tapes based on a combinations of about 50 fine filaments embedded in a matrix of silver or silver-alloy. Silver or silver alloy tubes are filled with precursor powder (a mixture of (Bi,Pb)-2212, $CaPbO_4$ and CuO) that will be reacted to form the superconductor. Silver plays a special role in this technology because it is chemically inert to the superconductor and because of its ability to diffuse oxygen at high temperatures, allowing a sensitive control of oxygen content of the final product. Moreover it results helpful to enhance the Jc at grain boundaries of the superconductor. About 50 wires are bundled together into another silver tube and deformed again. The multifilamentary wires are then deformed into a flat tape-shaped wire and the final step is applied. It in involves one or multiple heat treatments, usually in the range of 800-900 °C to react the powder, thus forming the desired HTS material within each individual filament. The combination of fine filaments with the metal matrix reduces the crack formation and allow critical strains, whether tensile, compressive or bend, in a range of several tenths of percent.

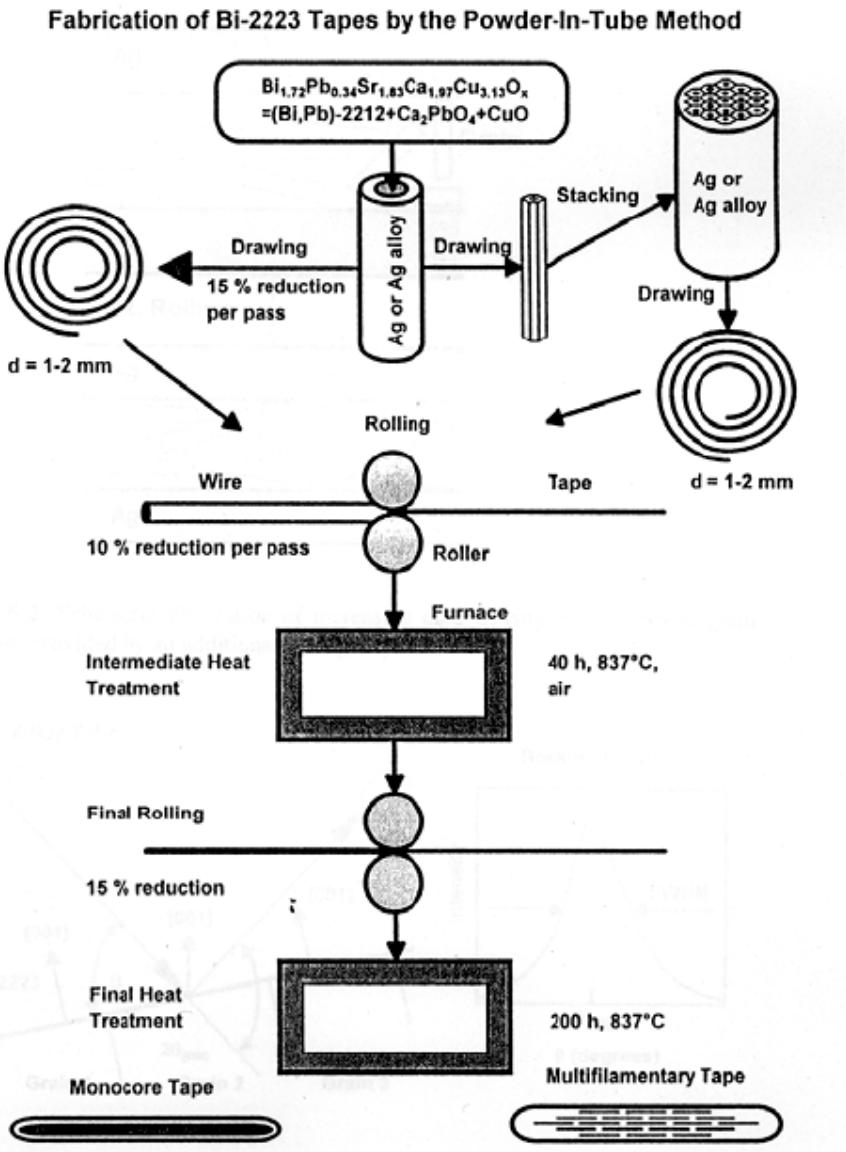

Fig. 3.13 – Production process of BSCCO-based wires by PIT method[25]

3.5.2 Coated Conductors

The basic architecture of a Coated Conductor composite (CC) is founded on a thin film of HTS material (very often YBCO) deposited on a flexible metallic substrate buffered with various intermediate layers to match and avoid ion diffusion from metal to YBCO and vice versa. The multi-layer by an overcoat of a noble metal also useful for current transport

in case of any superconductor breaks. Variations exist in adopted materials, in the number of buffer layers, in types and in the deposition methods for the buffer and superconducting layers, but the general architecture is similar. The possibility of applying thin film technology to the fabrication of HTS conductors is attractive from the point of view of very high critical currents that are a particular feature of the biaxially textured films.

Among HTS materials for Coated Conductors, YBCO resulted the best choice because it shows a very strong current carrying ability in magnetic field and high critical current density in self field. For comparison Tl- and Hg- based materials have a relatively high T_C and higher H_{irr} but low J_C values, due to the existence of weak-link dominated intergrain coupling problems. In addition, both Tl and Hg are toxic.

YBCO can achieve Jc values > 10^7 A/cm^2 at 4 K, and > 10^6 A/cm^2 at 77 K and has a very high irreversibility field (7÷10 T) at 77K. As we said before, a complex and careful growth is needed to obtain a good YBCO thin film avoiding Jc reduction caused by grain boundaries misorientation. The only way to obtain good transport properties is by orienting both c-axis and a-b basal planes of all grains.

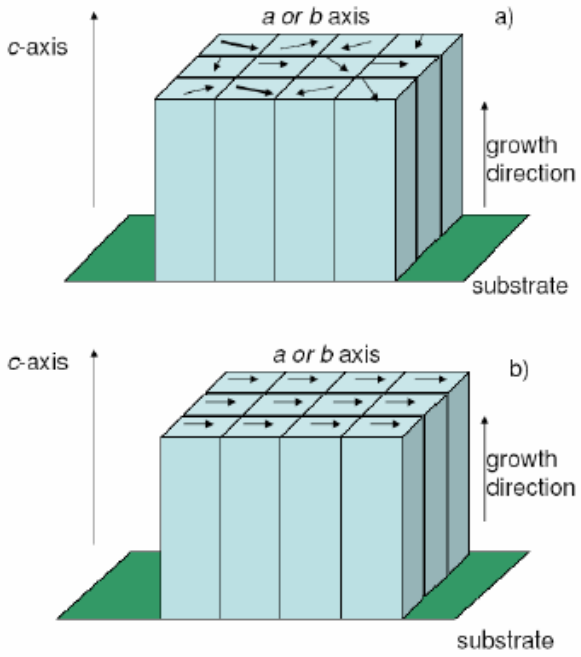

Fig. 3.14 – Uniaxial (a) and biaxially textured (b) growth of YBCO grains [26]

Another drawback in fabricating YBCO thin films is their mechanical brittleness. It is very difficult to produce long-length YBCO tapes without appropriate mechanical properties because these types of superconductors are ceramic materials. In order to enhance the mechanical resistance of long-length YBCO tapes, the superconducting layer must be deposited onto a flexible metal substrate and the thickness of the film must be very small. The direct deposition of the superconducting layer onto metal tape is forbidden, due to the poisoning effect of the metal, which degrades YBCO superconducting properties. The metal tape must be buffered with one or, more often, several intermediate films to create an appropriate structural matching between the metal and the biaxial YBCO and to exclude the poisoning of the YBCO or the de-oxygenation of itself. Not least, the buffer layers must provide a good adhesion with the substrate.

In brief, the economic success of Coated Conductors and the production of large amounts of these devices necessary for power application are made possible only if high quality and low cost techniques are used to prepare the biaxially textured superconducting layers as well as the epitaxially grown buffer introducing a simplified architecture.

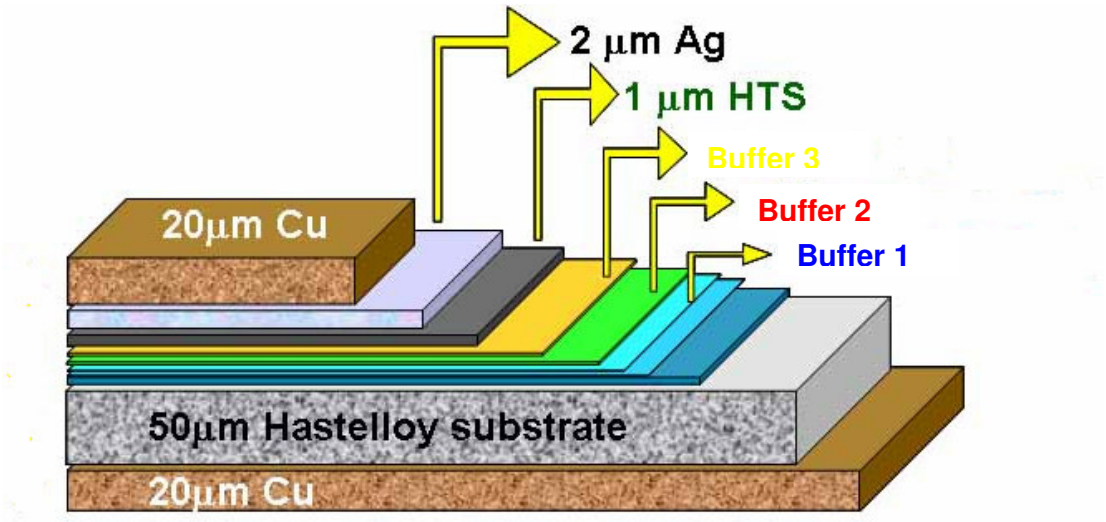

Fig. 3.15 – Typical Coated Conductors architecture based on multi-buffer layers sequence

3.6 Second generation HTS applications

YBCO-based coated conductors bring significant advantages such as their ability to carry up to many times greater current and power capacity per cross section than corresponding conventional copper cables, leading to reduced system weight and size. Additionally these systems reduce the environmental impact because no heat or electromagnetic fields are emitted. These unique features allow for very compact and low-cost installations in urban environments with crowded underground infrastructure.

HTS cables also have low series inductance, opening up economic ac power flow control in conjunction with phase angle regulators. However, handling fault currents requires a significant amount of high conductivity copper in parallel with the superconductor wires, and this reduces the size and weight advantages. HTS cables can also provide an alternate transmission path at lower voltage to increase transfer capacity.

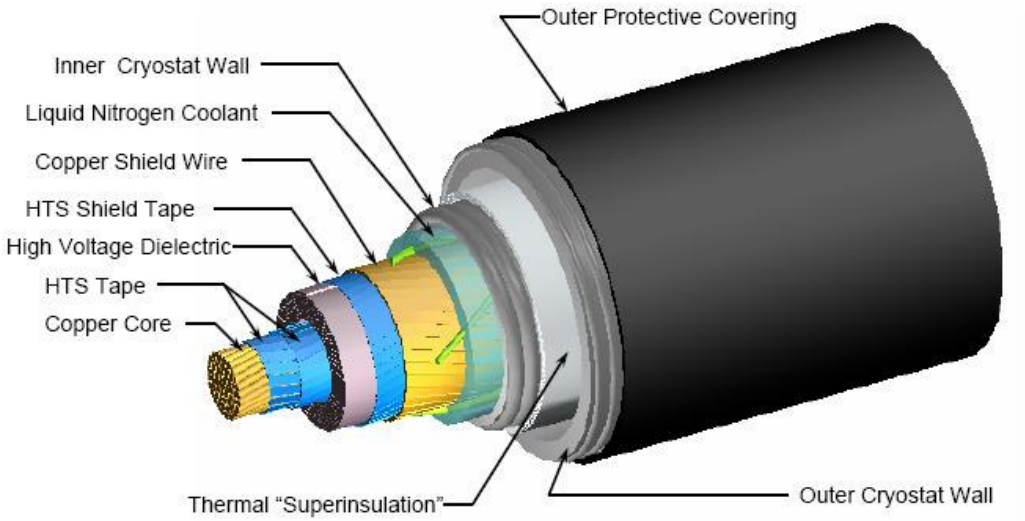

Fig. 3.16 – HTS cable used in high efficiency current transport grid prototype

HTS compound allow to realize also devices for electricity storing via persistent currents in a coil called superconducting magnetic energy storage (SMES) or persistent rotation with a magnetic bearing or flywheel energy storage systems (FESS). These materials can give the opportunity to produce compact, high-efficiency and low-environmental impact transformers with a high degree of safety because they could not contain any type of oil or lubricant.

In magnetic application, the only means of achieving magnetic fields high enough to meet the levels needed in medical applications such as nuclear magnetic resonance (NMR) was to base machines on LTS but magnets that incorporate HTS wires offer a significant set of benefits and improvements over them. Advantages of HTS magnets stem from:

- a simpler cooling systems often based on cryogen-free technology offering more design flexibility, simpler manufacturing processes, fewer moving parts and compact. These factors are also cost-effective on transportation and installation;
- a higher thermal stability than LTS magnet and coils that are more vulnerable to quenching (sudden loss of superconducting properties) because they operate at very low temperature. In addition, most LTS coils operate much closer to their critical temperature than their HTS counterparts and this means HTS devices can withstand greater temperature change without losing their superconducting properties;
- higher magnetic fields thanks to the high upper critical fields. HTS wire can produce magnetic fields stronger than those possible with LTS wire alone. HTS inserts produce fields up to 25 Tesla when used in LTS generated background fields.

Particularly, greeat advantages in magnetic application can be obtained by using superconducting quantum interference devices (SQUID). They are very sensitive magnetometers used to measure extremely small magnetic fields, based on superconducting loops containing Josephson junctions that are based on the phenomenon (called Josephson effect[29]) of current flow across two weakly coupled superconductors, separated by a very thin insulating barrier. These devices are sensitive enough to measure fields as low as 5×10^{-18}T within a few days of averaged measurements. For comparison, a typical refrigerator magnet produces 10^{-2} T, and some processes in animals produce very small magnetic fields between 10^{-9} T and 10^{-6} T. Since their high sensibility, SQUID's are already used in high sensitive and not invasive medical application such as magnetic resonance imaging (MRI) or magnetic marker monitoring to trace drug path after ingestion.

Not only for power transport but also high efficient and low-noise motors can be produced using CC and could be installed on vessels for ship propulsion or for factory production with increased stability and lower operating costs, considering also the cooling circuit and the liquid. In addition one can make use of HTS for electricity generation.

Several types of power generator have been projected with high efficiency and they are expected to be about 1/2 the size and weight of a conventional machine and to work with very low vibrations production. Since generators based on HTS technology can deliver energy at a considerably higher efficiency (+7%), 15,4 GW could easily be saved "for free" on the global scale without any environmental impact using at the same time HTS devices for energy transport and hydropower or windpower. This would be equivalent to roughly 40 conventional power stations that can be deferred due to the use of efficient HTS technology for renewable resources leading to a significant contribution to the Kyoto-protocol targets[27].

Another important potential contribution of HTS technology are fault current limiters (FCL), devices which will limit the current spike and the mechanical forces in event of a high-current short circuit. FCL is a passive device that requires no external sensing of the current to initiate the transition because the HTS materials smartly provide protection by instantaneously becoming resistive under high current conditions. This event causes a temperature increasing of the device but after some minutes of cool down it will be ready to superconduct again. Thank to its reversible ability, these devices are very different from typical fuses and are designed for high current faults that happen in grid or factory electrical system and must be handled with special devices[28].

A surprising but already concrete use of 2nd generation HTS cable is found in magnetic levitation train. These have been studied since the first 1970s and in advanced Countries, such as Japan, U.S.A. or China, they are daily used by people for travelling. The so-called MAGLEV technology is based on three different levitation system:

1. Electromagnetic suspension (EMS) where the train levitates above a steel rail while superconducting electromagnets, mounted on the train, are oriented toward the rail from below. The electromagnets use feedback control to maintain a train at a constant distance from the track, at approximately 15 mm.
2. In Electro-Dynamic suspension (EDS), both the rail and the train exert a magnetic field, and the train is levitated by the repulsive force between these magnetic fields. The magnetic field in the train is produced by either superconducting electromagnets or by an array of permanent magnets. The repulsive force in the track is created by an induced magnetic field in wires or other conducting strips in

the track. At slow speeds, the current induced in these coils and the resultant magnetic flux is not large enough to support the weight of the train. For this reason the train must have wheels to support the train until it reaches a speed that can sustain levitation. Propulsion coils on the guideway are used to exert a force on the magnets to make the train moving forward and being constrained at the centre of the guideway.

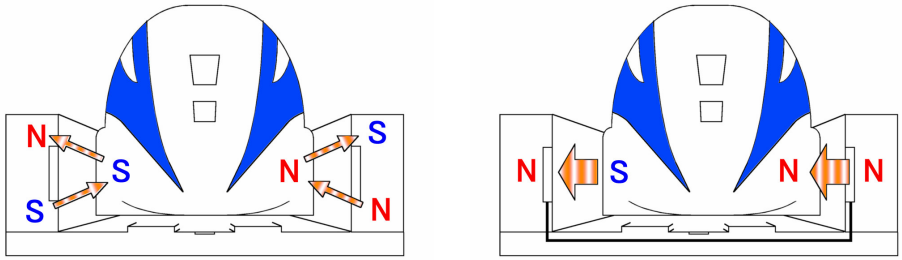

Fig. 3.17 – EDS MAGLEV magnetic field to move, sustain and centre the train

3. Many studies are going on to improve EDS system by testing Stabilized Permanent Magnet suspension (SPM). It differs from EDS maglev in the use of opposing sets of rare earth magnets (typically neodymium alloys or HTS) in the track and vehicle to create permanent, passive levitation. This means that no power is required to maintain permanent levitation. With no current required for levitation, the system has much less electromagnetic drag, thus requiring much less power to move.

Concluding this paragraph, it is possible to assert the great importance that HTS materials have for producing innovative devices to overtake several problems well-known so far. Many progresses have been realized and it could be possible to optimize energy production efficiency, decrease energy waste in current transport and invent new employments for these materials, but several development issues must be faced to reach cost-effective materials and more effective items to better and better HTS-based devices for application.

Moreover, the solution of the energy problem and the subsequent reduction of greenhouse effect might be reached faster and in an optimal way by the contribution of coated conductors and renewable technologies.

References

[1] J. G. Bednorz, K. A. Muller: Zeitschrift fur Physik B-Condensed Matter, **64** (1986)

[2] X. Obradors, T. Puig, A. Pomar, F. Sandiumenge, N. Mestres, M. Coll, A. Cavallaro, N. Romà, J. Gázquez, J. C. González, O. Castaño, J. Gutierrez, A. Palau, K. Zalamova, S. Morlens, A. Hassini, M. Gibert, S. Ricart, J. M. Moretó, S. Piñol, D. Isfort and J. Bock: "Progress towards all-chemical superconducting $YBa_2Cu_3O_7$ coated conductors", *Superconductor Science and Technology,* **19** (2006) S13-S26

[3] M. K. Wu, J. R. Ashburn, C. J. Torng, P. H. Hor, R. L. Meng, L. Gao, Z. J. Huang, Y. Q. Wang, C. W. Chu, *Physical Review Letters*, **58** (1987) pp. 908 – 910

[4] H. K. Onnes: *Leiden Comm.* **120b, 122b, 124c** (1911)

[5] T. P. Sheahen: "Introduction to High-Temperature Superconductivity" (1994) Springer

[6] O. J. Bressan, A. E. Ridner, F. de la Cruz: "T5 law and Matthiessen's rule", *J. Phys. F: Metal Physics*, **5** (1975) pp. 481 – 486

[7] J. Bardeen, L. N. Cooper, J. R. Schrieffer: "Theory of Superconductivity", *Physical Review*, **108**, issue 5, (1957) pp. 1175 – 1204

[8] C. Kittel: "Introduction to Solid State Physics", Chapter 10, 8th Ed., (2005) Wiley

[9] A. A. Abrikosov: "On the magnetic properties of Superconductors of the second group", *Soviet Physics JETP,* **5,** 6 (1957)

[10] W.R. Hudson: "The Mixed State of Superconductors", National Aeronautics and Space Administration (1970)

[11] A. Schilling, M. Cantoni, J. D. Guo, H. R. Ott: "Superconductivity above 130 K in the Hg-Ba-Ca-Cu-O system", *Nature,* **363** (1993) 56

[12] A. Mourachkine: "High-Temperature Superconductivity in Cuprates – The Nonlinear Mechanism and Tunnelling Measurements", (2002) Springer

[13] J. D. Jorgensen, M. A. Beno, D. G. Hinks, L. Soderholm, K. J. Volin, R. L. Hitterman, J. D. Grace, I. K. Schuller, C. U. Segre, K. Zhang, M. S. Kleefisch: "Oxygen ordering and the orthorhombic-to-tetragonal phase transition in $YBa_2Cu_3O_{7-x}$", *Phys. Rev. B.*, **36 (**1987) pp.3608 – 3615

[14] G. Triscone, A. Junod, R. E. Gladyshevskii: "Magnetic and thermal properties of the 116 K superconductor Tl-1223", *Physica C*, **264** (1996) pp.233 – 249

[15] L. M. Fisher, A. V. Kalinov, S. E. Savel'ev, I. F. Voloshin and V. A. Yampol'skii: "Critical current anisotropy in YBCO superconducting samples", *Physica C*, **309** (1998)

[16] S. W. Tozer, A. W. Kleinsasser, T. Penney, D. Kaiser, and F. Holtzberg: "Measurement of anisotropic resistivity and Hall constant for single-crystal $YBa_2Cu_3O_{7-x}$", *Phys. Rev. Lett.* **59**, (1987) p.1768

[17] H. Hilgenkamp, J. Mannhart: "Grain boundaries in high-Tc superconductors", *Reviews of Modern Physics*, **74** (2002)

[18] A. Gurevich, E. A. Pashitskii: "Current transport through low-angle grain boundaries in high-temperature superconductors"*, Physical Review B*, **57** (1998)

[19] E. Sarnelli, P. Chaudhari, J. Lacey: "Residual critical current in high Tc bicrystal grain boundary junctions", *Applied Physics Letters*, **62** (1993)

[20] D. T. Verebelyi, D. K. Christen, R. Feenstra, C. Cantoni, A. Goyal, D. F. Lee, M. Paranthaman, P. N. Arendt, R. F. DePaula, J. R. Groves, C. Prouteau,"Low angle grain boundary transport in $YBa_2Cu_3O_{7-\delta}$ coated conductors", *Applied Physics Letters*, **76** (2000) pp. 1755–1757

[21] D. Larbalestier, A. Gurevich, D. M. Feldmann, A. Polyanskii: "High-Tc superconducting materials for electric power applications" *Nature,* **414** (2001) pp. 368-377

[22] Araki T., Kurosaki H., Yamada Y., Hirabayashi I., Shibata J., Hirayama T.: "Coating processes for $YBa_2Cu_3O_{7-x}$ superconductor by metalorganic deposition method using trifluoroacetates", *Superconductor Science and Technology,* **14**, (2001) pp. 783-786

[23] M. Paranthaman, T. G. Chirayil, S. Sathyamurthy, D. B. Beach, A. Goyal, F. A. List, D. F. Lee, X. Cui, S. W. Lu, B. Kang, E. D. Specht, P. M. Martin, D. M. Kroeger, R. Feenstra, C. Cantoni, D. K. Christen: "Fabrication of long lengths of YBCO coated conductors using acontinuous reel-to-reel dip-coating unit", *IEEE Transactions on Applied Superconductivity*, **11,** (2001)

[24] A. Usoskin, J. Knoke, F. Garcia-Moreno, A. Issaev, J. Dzick, S. Sievers, H. C. Freyhardt: "Large-area HTS-coated stainless steel tapes with high critical currents", *IEEE Transactions on Applied Superconductivity*, **11,** (2001)

[25] G. Grasso, F. Marti, Y. Huang, R. Flükiger "Long Lengths of Bi2223. Superconducting Tapes", *Cryogenics* **37** (1997)

[26] S. Rampino: "Supersonic O_2 Beam Assisted Deposition of Long-Length $YBa_2Cu_3O_7$ Coated Conductors", Ph. D. Thesis, (2007)

[27] Sustainable development commission, "Wind power in UK" (2005)

[28] Swarn S. Kalsi and Alex Malozemoff: "HTS Fault Current Limiter Concept", Power Engineering Society General Meeting (2004)

[29] B. D. Josephson: "The discovery of tunnelling supercurrents", *Rev. Mod. Phys.* **46** (1974)

Doped-CeO_2 for HTS-CC single buffer layer architecture

Introduction

In chapter 3, talking about HTS-Coated Conductors (CC), it has been reminded that one of the most important issue to reduce their production costs of CC in view of an industrial manufacturing is the simplification of the multi-buffer layer architecture toward a structure based on a suitable single buffer layer. Obviously, it must retains the same properties showed by the use of a complex buffer layer architecture.

the single buffer layer must posses the fundamental characteristics listed below:

- intermediate mismatch between substrate and HTS layer in order to have a good adhesion onto the substrate and avoid crack formation on its surface;
- intermediate thermal expansion coefficient between substrate and HTS layer to resist against thermal stresses due to the warm-up and the cool-down necessary for deposition processes of following films;
- powerful barrier ability versus ion interdiffusion (both at work and deposition temperature of other layers) to avoid that YBCO results de-oxygenated by the migrations of oxygen toward the substrate or polluted by metal ion coming from the substrate,
- high bi-axially texturing capability for transmitting it to YBCO deposited in the second step.

As already pointed out, the substrate, the material to use as buffer and deposition technique are key parameters to realize the YBCO-based CC. For our project, Ni-5 at.%W RABiTS^{TM} (see below, for more details) has been chosen as substrate; Cerium oxide (CeO_2), already used in multi-buffer layer architecture, appeared the best candidate for single-buffer CC; e-gun evaporation and PED techniques has been used as deposition method for this layer and thermal co-evaporation and PLD for YBCO films.

4.1 Substrates

In order to enhance mechanical resistance and reach high current density Jc of the ceramic YBCO, metal substrates have to be used. Substrates used in CC production are essentially Ni-based alloys. Indeed the nickel and its alloys are of crucial importance for

modern technology thanks to their ability to operate in a wide range of extreme situations such as corrosive environments, high temperatures, high mechanical stresses. They can be divided into 2 groups: polycrystalline alloys and Rolling Assisted Bi-axially Textured Substrate (RABiTS^{TM}). First types don't present particular structural properties and a seed layer has to be deposited before the real buffer layer to provide the necessary bi-axial texturing. On the contrary RABiTS^{TM} are a Ni-based alloy added with Tungsten (W) in 5% atomic ratio, in which bi-axially texturing is provided by lamination, annealing, rolling and recrystallization processes. Often a sulfurization step is applied because it was noticed that S layer behaves like a template, allowing proper match and optimal oxygen atom arrangement and facilitating the bond formation of cations and (001) epitaxial nucleation of the oxide film[1]. Finally, cleaning and polishing are performed to optimally prepare the surface for buffer depositions (**fig. 4.1**).

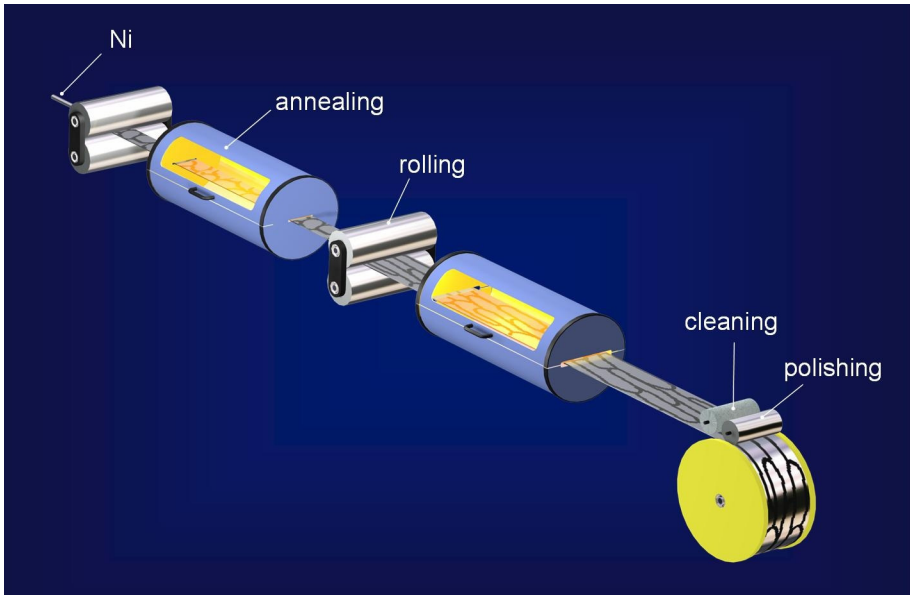

Fig. 4.1 – Scheme of production process of RABiTS^{TM}

Substrates of interest for this application include cubic metal and alloy, such as face-centred cubic (FCC) and body-centred cubic (BCC). While BCC metals, such as Fe-based alloys could be used, for CC application Ni and Cu based alloys are of primary interest. Texturing effect is commonly called cube texture because it can be described by a cube plane parallel to the plane of the sheet and a cube edge parallel to the rolling direction

(**fig. 4.2**). A fully developed cube texture looks like a single crystal with a mosaic of sub-grains[2].

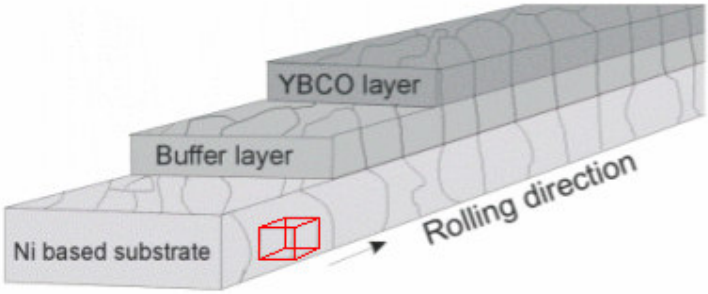

Fig. 4.2 – Detail of cube texturing (red cube) in Ni-alloy polycrystalline tape for CC application

Silver has also been tested as suitable metal for RABiTS™ production but its high vapour pressure created many problems on most oxide films deposited. The layers appeared very rough and with a low out-of-plane orientation. In addition, the high cost of Ag pushed researcher to discard it.

Using this method cube texture has been obtained in binary ant ternary Ni-based alloys, such as Ni-W, Ni-Cr, Ni-Mo, Ni-V, Ni-Cr-Al and Ni-Cr-W. All of this studies were made to improve the performance of the YBCO layer because the cube textured substrates must present other distinctive features: it has to be robust to face the thermal and mechanical stresses of the processes involved in CC production and it must be less magnetic as possible to reduce AC losses. All the ternary alloys and Ni-13 at.%W present absolute non-magnetic behaviour but even low alloying content substrates exhibit significantly reduced AC losses compared to pure Ni substrate[3]. Moreover, all the alloy present higher mechanical strength and higher cube texturing capability than pure Ni.

Material	**Yield strengths**	**Curie Temp**
Pure Ni	340 bar	627 K
Ni-9 at.%Cr	870 bar	124 K
Ni-13 at.%Cr	1640 bar	Non-magnetic
Ni-5 at.%W	1650 bar	335 K
Ni-13 at.%Cr-4%Al	2280 bar	Non-magnetic
Ni-8 at.%Cr-4%W	2020 bar	Non-magnetic

Tab.4.1 – Some alloys of significant interest for RABiTS™ compared with pure Ni[4]

Two additional methods exist to produce highly textured which reduces magnetism and have high mechanical strength: a powder in tube approach, where a Ni or Ni-alloy tube is filled with a mechanically strong and non-magnetic powder and then laminated[5], or a rolled substrate of a composition that can be textured, is laminated with an additional mechanically strong and non-magnetic substrate[6].

Among the substrate listed above, Ni-5 at.%W, used in our project, shows the best compromise between cost and performance.

4.2 Buffer Layers

In order to be an effective barrier against ionic diffusion, the buffer layer must present the absolute absence of cracks, that are usually caused in a fragile material by lattice mismatch and by large differences of thermal expansion with the substrate. Indeed, this fact avoids the same response to thermal stresses creating excessive strain on the buffer which relaxes by cracking. Obviously, the crystallographic orientation of the buffer requires a cube texture which can be copied by the substrate to be perfectly transferred to the YBCO, realizing a superconducting thin film with optimal performances.

Material	**Structure**	**Lattice parameter (Å)**	**Effective parameter (Å)**	**Mismatch with YBCO (%)**	**Mismatch with Ni-W(%)**	**Oxygen diffusivity (cm^2/sec) @ 700°C**	**α (10^{-6}/°C) @ 25 °C**
MgO	NaCl type	4,216	4,216	-9,6	19,4	$2,0x10^{-23}$	8-12
CeO_2	**Fluorite**	**5,411**	**3,826**	**-0,3**	**8,4**	**$2,0x10^{-9}$**	**9,9-13**
Y_2O_3	BCC	10,55	3,723	-3,4	5,5	$2,0x10^{-10}$	8,5
YSZ	Fluorite	5,139	3,636	-5,8	3,0	$7,0x10^{-9}$	8,5
$SrTiO_3$	Perovskite	3,905	3,905	1,4	10,6	$6,0x10^{-11}$	11
YBCO	**Orthorombic**	**3,83x3,88**	**3,85**	**0**	**9,0**	**-**	**10-14**
Ni-W	**FCC**	**3,53**	**3,53**	**-9,0**	**0**	**-**	**13-19**

Tab. 4.2 – Properties of common material used as buffer layers for CC. α is the thermal expansion coefficient [7]

In the case of CC realized using a high-temperature deposition techniques, the employment of a multi-buffer layer architecture is necessary to avoid unwanted oxygen diffusion from the YBCO layer and therefore the subsequent substrate reactions which are

thermally activated[8]. Moreover the multilayer structure is usually applied to gradually reduce the stresses due to lattice mismatch between substrate and YBCO. The multilayer structure is very often obtained by the coupling of two or more of the buffer layers listed in **tab. 4.2** and Ceria (CeO_2) is always present as a seed layer to protect the substrate from oxidation and as cap layer deposited on the "real buffer" layer-series before the deposition of YBCO. For example, MgO presents the lowest oxygen diffusivity value but it exhibits a large lattice mismatch with YBCO and Ni-based substrate, thus introducing excessive strains in the growing layer. For this reason MgO cannot be a suitable candidate to assume the function of single buffer layer for CC.

4.3 Alternative deposition techniques for buffer deposition

Just a little digression about particular deposition technique requested for buffer layers deposition might be useful.

The primary need to obtain a biaxial texturing for the buffer layer can be reached starting from a cube textured substrate (RABiTS^{TM}) or using particular deposition tricks starting from a simple polycrystalline substrate such as Hastelloy, Inconel or stainless steel.

In this case, the biaxial texturing of the buffer can be obtained by using ion-beam assisted deposition (IBAD) or inclined substrate deposition (ISD) technique.

IBAD requires, besides the principal evaporation source, a secondary ion source[9] which makes a substantial rise of the installation costs and complexity of use (**fig. 4.3**). By controlling the beam geometry, the energy and the mass of bombarding ions, one can eliminate the undesired orientations, obtaining a biaxially textured and very compact buffer layer[10]. This method allows a free choice of the desired substrate materials because neither crystalline alignment between buffer layer and substrate, nor epitaxial growth are needed. The mechanism of texturing is based on the different ion sputtering effect from differently oriented grains and as a consequence, a preferential growth of grains with lattice planes parallel to the beam direction occurs[11].

Materials usually grown by IBAD technology are: Yttria-stabilized Zirconia (YSZ), Gd-doped Ceria (GCO) or MgO for insulating buffer layers.

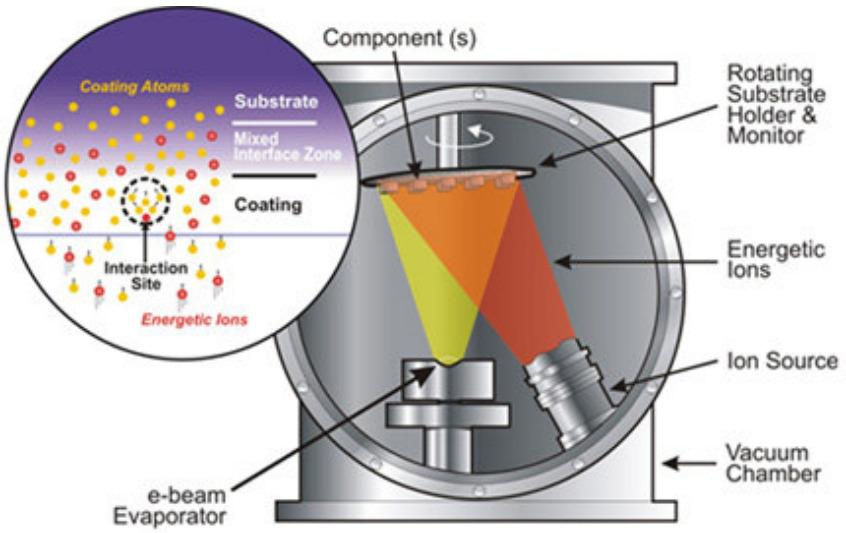

Fig. 4.3 – IBAD system for biaxial textured buffer layer growth on polycrystalline substrates

ISD[12] is a simple technique, differing from other PVD technique only for the angle α formed between the evaporated direction and the normal to the substrate surface. Thanks to this trick, the growth explpoits a sort of self-shadowing effect due to fast growing crystal planes on slower ones. For example, at a given α value of about 55° for MgO, the [200] planes grow faster, leading to a MgO films formed by truncated columns with the [200] planes inclined of an out-of plane angle β with respect to the substrate normal[13-14].

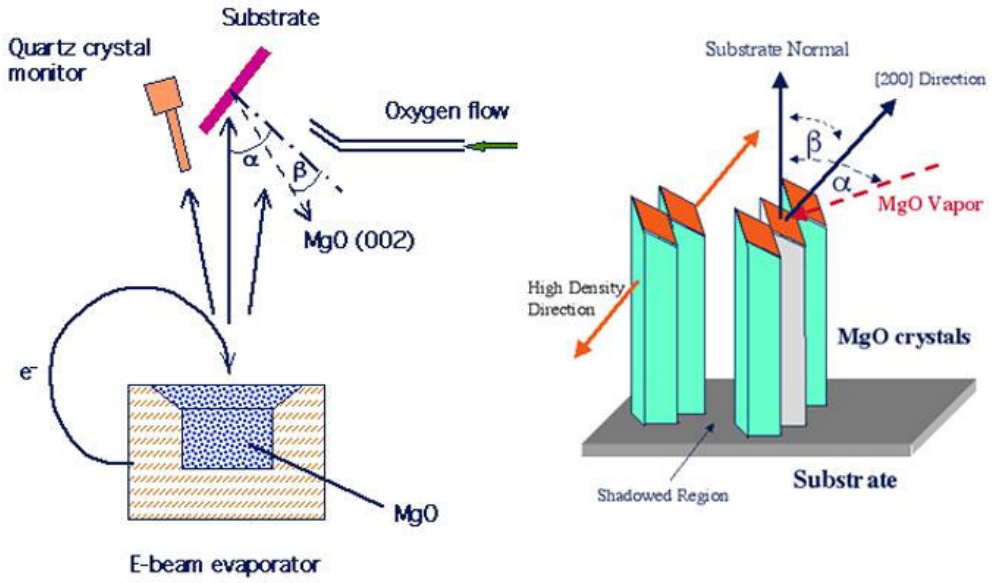

Fig. 4.4 – ISD schematic disposition (on the left) and truncated columns growing process (on the right)

Both techniques are characterized by an in-plane biaxial texture improved by increasing the film thickness. Above 1 μm thickness, the film orientation moves from a random to a perfect in-plane texture. Unfortunately, the implication is that a long deposition time and a high accuracy on the thickness measurement are required; thus, a simpler and faster deposition method is preferable.

4.4 Cerium oxide (CeO_2) as a suitable single buffer layer

The single buffer layer architecture is a great advantage to increase the production rate of YBCO coated conductors. The co-evaporation process, chosen in view of low-cost and long-length CC, allows the use of this simple architecture thanks to weaker diffusion mechanisms occurring at low deposition temperatures. CeO_2 can act as single buffer layer since it exhibits an optimal match with YBCO and a sufficiently low oxygen diffusivity. The latter characteristic can be improved by the growth of film with thickness about 100 nm. However it is well-known that the high mismatch with Ni-5at%W causes formation of a crack network in CeO_2 film just when its thickness exceeds 100 nm. Cracks are obviously undesirable, not only for ion interdiffusion, but also because cracks propagation towards YBCO layer breaks the contiguity between grains and consequently the percolative path of the electric current.

The existence of a critical thickness, t_c, comes out from the relaxation of the elastic energy stored up during the epitaxial growth of the film on the substrate which presents a lattice parameter very different. Even different expansion behaviours between substrate and grown layer due to temperature gradients may increase the strain. Fragile materials as CeO_2 are inclined to crack rather than forming extended defects.

The critical thickness can be described by the following theoretical expression[15]:

$$t_c = \frac{\Gamma E}{Z\sigma^2} \qquad \text{(Eq. 4.1)}$$

where Γ is the fracture toughness, E is the elastic modulus of the material, Z is a constant and σ is the critical stress suffered by the film. It is important to notice that the critical stress can be written as:

$$\sigma = E\frac{\Delta a}{a} - \delta \qquad \text{(Eq. 4.2)}$$

where the relation between σ and the mismatch $\frac{\Delta a}{a}$ is clear. The term δ related to the presence of defects or impurities allows to withstand higher elastic energy before cracking.

Rutherford back scattering (RBS, described in detail in section 4.7.3) data measured at Jülich Forshungzentrum confirm that CeO_2 100 nm thick films don't present an efficient barrier effect to Ni diffusion to the surface (**fig. 4.5**).

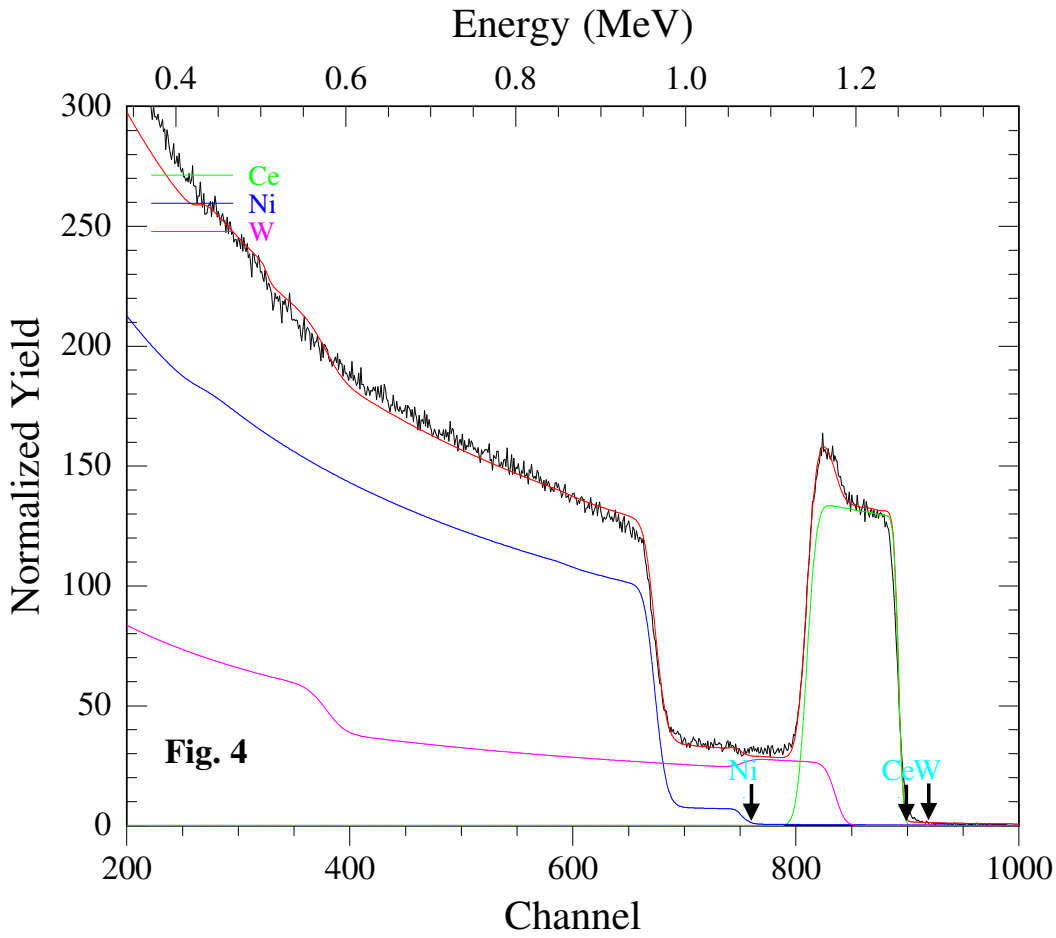

Fig. 4.5 – RBS data for a 100 nm thick CeO_2 film grown by e-gun evaporation

The reported results from RBS analysis clearly demonstrate that 100 nm for CeO_2 film are not sufficient to avoid Ni migration up to the surface, while W is contained within the oxide layer. Indeed, the Ni-presence onto the sample surface is detected by the little edge of the black line exactly corresponding to the theoretical signal for a pure-Ni surface. On

the other hand, scanning electron microscopy (SEM) image show the crack network appearing for CeO_2 film deposited onto Ni-W substrate thicker than the calculated critical limit (**fig. 4.6**).

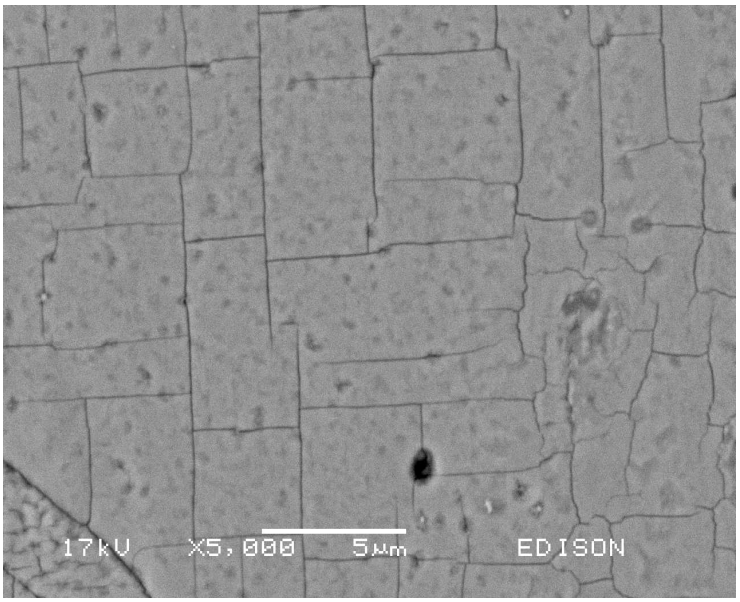

Fig. 4.6 – Typical crack network for a CeO_2 film with a thickness of 120nm

From the SEM image it is clear that the cracks follow preferential directions forming 90° angles when they intersect. This is also an index related to the texturing of the CeO_2 layer because of the fluorite cubic structure of this oxide.

In order to solve this problem we try to insert some different ions, such as Yb^{3+}, Sm^{3+} and Zr^{4+} to enhance mechanical properties of CeO_2 and to reduce the lattice mismatch with Ni-W substrate.

4.5 Doped-CeO_2 to solve the issues of pure CeO_2

The doping effect of doping on structural, mechanical and electrical properties of CeO_2 have been deeply studied by several research group, in particular for the development of solid oxide fuel cells (SOFC)[16-19]. An important property required as the electrolyte of SOFC is the high oxygen-ion conductivity which creates a preferential path for O^{2-} ions. To enhance this ability, oxygen vacancies are introduced by doping the CeO_2 matrix with trivalent Rare Earth (RE) element that, in addition, induce lattice deformations for lower

valence and smaller ionic radius (**fig. 4.7**). Particularly interesting for our goals, is the reduction of lattice parameters due to trivalent ions that substitute Ce^{4+} in the structure. As a macroscopic consequence, the reduction of lattice parameters reduction increases structure toughness improving mechanical properties of the material.

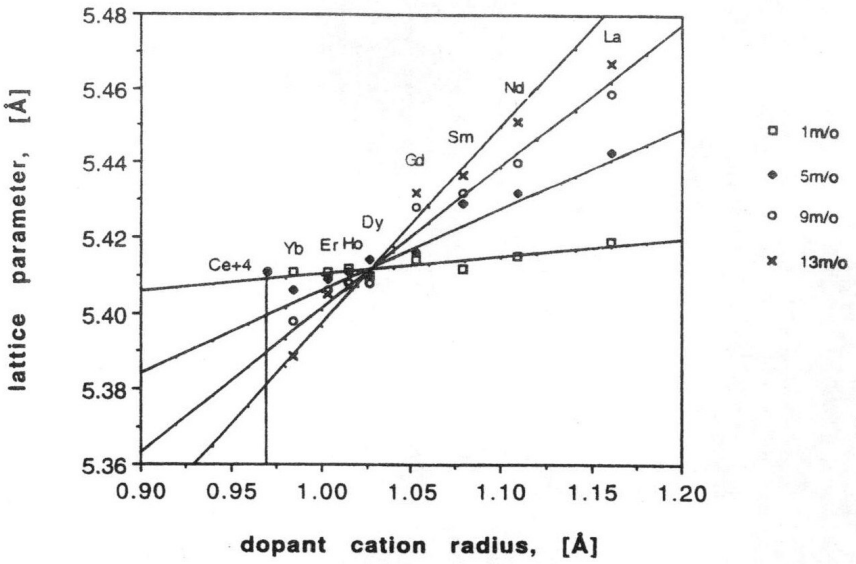

Fig. 4.7 – CeO_2 lattice parameter in function of dopant cation radius and concentration [20]

Dopant cations used in CeO_2 system take the place of Ce^{4+} providing a substitutional doping effect. In this way the fluorite structure of CeO_2 is preserved while lattice parameter undergoes a remarkable variation.

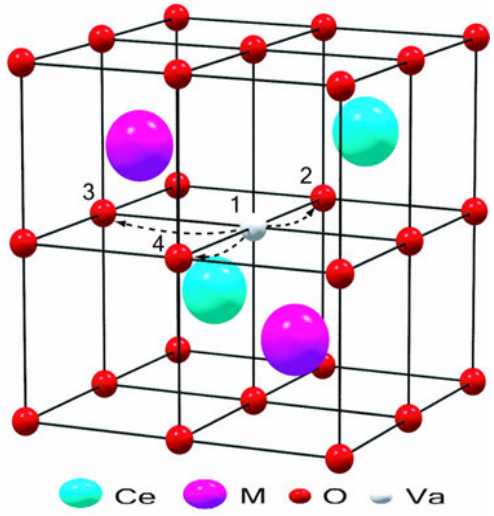

Fig. 4.8 – Cations substitution in CeO_2 fluorite structure

Results from X-ray Absorption Fine Structure (XAFS) analysis about binding energy of doped CeO_2 showed interesting results about the shrinkage of Ce-O bond caused by the introduction of trivalent cations in the structure[18].

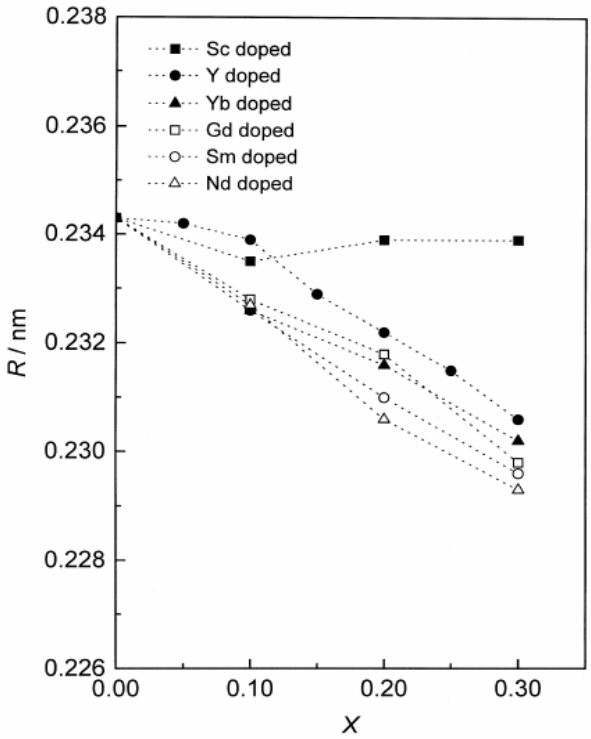

Fig. 4.6 – Ce-O distance in doped CeO_2 with various concentration of different trivalent cation [18]

This effect originates from the introduction of the oxygen vacancies that lead the oxygen atoms in the matrix to shift towards the vacancy, reducing the Ce-O distance.

On the other hand, the larger atomic radius of some trivalent cations induces an enlargement of the structure; this effect usually dominates the oxygen vacancy.

The lattice shrinkage effect can be obtained also by introducing in the ceria matrix iso-valent 4+ doping atoms with the same coordination number and a lower ionic radius than the Ce one[21]. In example, by substituting Ce^{4+} atoms (ionic radius = 0,97 Å) with Zr^{4+} ones (ionic radius 0,84 Å), the lattice dimensions can be strongly reduced.

In order to calculate the critical thickness enhancement occurring by doping the Ceria layer, one can take the equations written above (**Eq. 4.1**) and (**Eq. 4.2**) obtaining:

$$t_c \propto \frac{\Gamma}{E(\Delta a / a)^2} \qquad \text{(Eq. 4.3)}$$

For example, a Zr(15% at.)-doped ceria leads to a lattice reduction from 5,41 Å to 5,35 Å (**fig. 4.6**). This corresponds to a reduction of lattice mismatch from ~8,9% to ~7,1%. From equation **4.2**, we can calculate that the stress reduction is of about 20%, and from **4.3** a critical thickness enhancement from 100 nm to ~150 nm is expected. For our project we simply try to apply this theoretical model to grow thick and crack-free ceria layer.

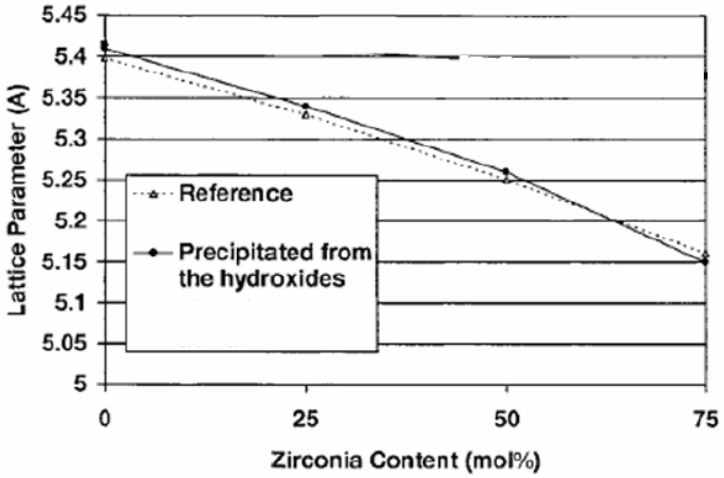

Fig. 4.6 – CeO_2 lattice parameter reduction in function of ZrO_2 content [19]

4.6 Experimental procedure: doped-Ceo_2 grown by e-gun evaporation

Target of doped-CeO_2-based compounds have been prepared by mixing CeO_2 and the oxide of the dopant atom in stoichiometric ratios, pressing the pellets with 70÷80 bars (at ambient temperature for 5 minutes) and sintering at 1300 °C for 8 hours (heating rate of 180 °C/h). Since these doped-ceria targets have a high melting point (>2300 °C), no evaporation from the tungsten crucibles of the TCE system occurs. The deposition of doped-ceria films onto Ni-W substrates has been carried out by using a continuous electron beam source because colliding electrons are able to evaporate targets with a melting point up to 3000°C.

The principles of this technique have been described in section 2.1.2. and the specific features of the apparatus used for these experiments will be reported. In this system the electrons are emitted from a tungsten filament located under the crucible at the bottom of the chamber, and then accelerated by a 8 KV voltage. A permanent magnet is utilised to bend of 270° and focus the electron beam, ensuring that the beam collide on the crucible

maintaining the filament protected by evaporated material, coating debris and erosion caused by the bombardment. This prolongs filament life and ensures beam stability during evaporation then a magnetic field deflects it towards the crucible. The latter is a copper water-cooled crucible to prevent the reaction of the molten material with the copper and to ensure high purity, contaminant-free deposition. The evaporation rate is controlled by the a micro balance based on an oscillating quartz which control the growth rate by means the variation of its oscillating frequency in function of the thickness of the growing layer. This is possible for a high number of materials simply by selecting the desired compound from a database stored in the controller.

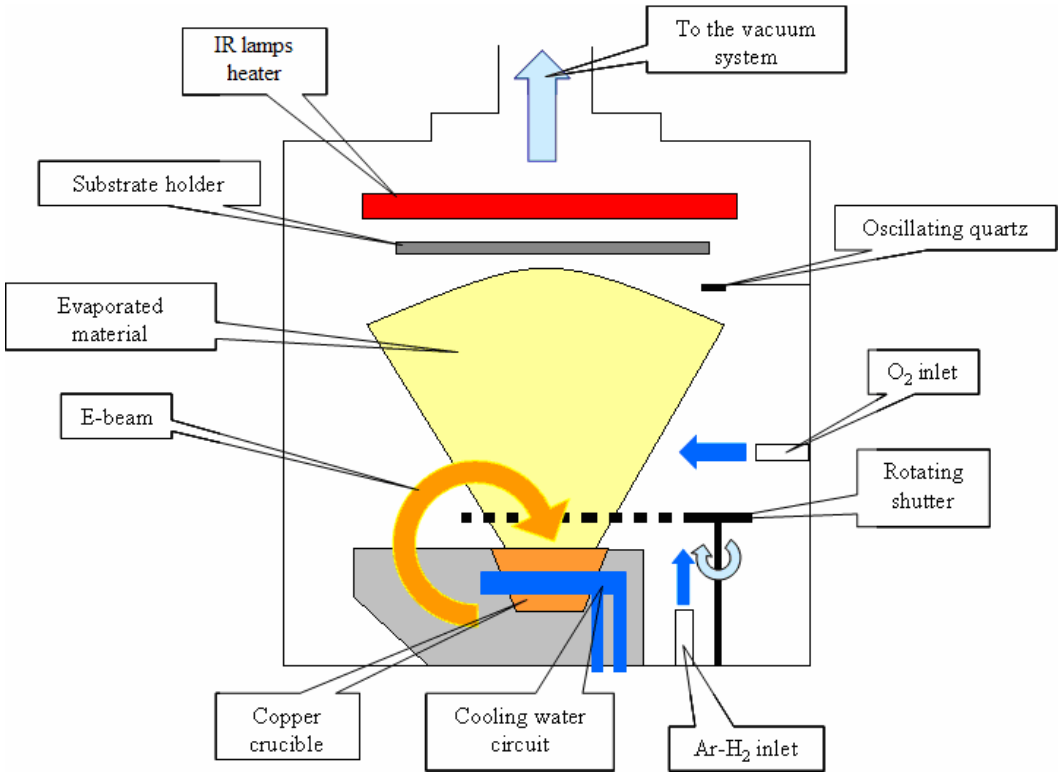

Fig. 4.9 – Deposition chamber equipped with e-gun evaporation system used for doped ceria growth (R&D laboratories of EDISON s.p.a. in Trofarello (TO)

Biaxially cube-textured Ni-5at.%W alloy substrates have been placed on a sample holder close to a halogen lamp heater. The metal tapes were pre-annealed in 10 mbar of a Ar/H_2(5%) forming gas mixture at 600 °C for 60 minutes to eliminate the NiO formed on the surface.

The occurring reaction is:

$$NiO(s) + H_2(g) \leftrightarrow Ni(s) + H_2O(g) \qquad \text{(Eq. 4.5)}$$

In a second step doped-CeO_2 targets were evaporated by the e-gun, in the same reducing atmosphere at $8x10^{-5}$ mbar. Every doped-ceria target has been deposited at various temperatures between 400 and 700 °C, to test the thermodynamic conditions to achieve the best film texture. Moreover, we have systematically varied the thickness of the doped-ceria layer to determine the critical thickness.

4.7 Characterization techniques

Before the illustration of the results obtained in this part of the project, a brief explanation about the characterization techniques used to study doped-CeO_2 film will be reported.

4.7.1 X-Ray Diffraction (XRD)

X-ray diffraction is a multi-function technique used to identify the crystalline phases of material and to analyze structural properties. In particular it has been proved to be very useful in thin film growth to verify the in-plane and out-of-plane orientation of grains, their size and phase composition. With high resolution facilities it is also possible to detect strain fields due to heteroepitaxial growth and defect presence.

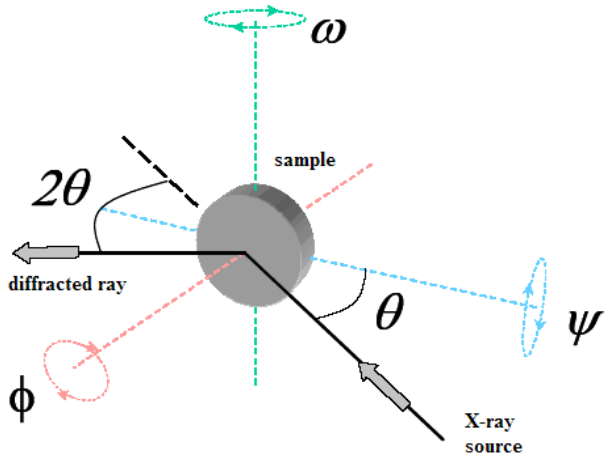

Fig. 4.10 – Geometry of X-ray diffractometry

Three types of measurements were made with XRD: θ/2θ-scan, ω-scan and φ-scan.

Conventional θ/2θ XRD pattern provides several information about the dimension of the elementary cell, the content of elementary cells, the crystallite dimension and hints about

out-of-plane orientation of the thin film analyzed. from the diffraction pattern, the lattice relative parameter (d) can be calculated by the Bragg's law: $d = n\lambda/a\ sen\theta$ where λ is the X-ray wavelength.

The ω-scan XRD measurements (known as rocking curves) quantifies the out-of-plane orientation of the film by tilting of a very small angle ω (within the diffraction plane) once selected the diffraction peak (at a fixed 2θ angle). By measuring the full width at half maximum (FWHM) value of the profile, $\Delta\omega$, we obtain information about the degree of the out-of-plane orientation.

The pole figures reveal the in-plane texture of thin films. The measure is taken at a fixed scattering angle and consists of a series of φ-scans (in-plane rotation around the ϕ–axis passing from the centre of the sample) at different tilt angles around ψ-axis. For this technique, we can obtain information about the grain alignment on the plane parallel to the substrate surface.

The presented $\theta/2\theta$-scan and ω-scan measurements have been carried out at IMEM-CNR on a Siemens D500 while the pole figures have been performed at University of Trento (Siemens D500T).

4.7.2 Scanning Electron Microscopy (SEM) and Energy Dispersive X-Ray Spectroscopy (EDS)

The SEM is an instrument that produces a magnified image by using electrons instead of light to form an image. A beam of electrons is produced at the top of the microscope by an electron gun. The electron beam follows a vertical path through the microscope, in vacuum. The beam travels through electromagnetic fields and lenses, which focus the beam down-ward the sample. Once the beam hits the sample electrons will scatter through the specimen within a defined area called the interaction volume. During the electron beam-sample interactions, secondary products like secondary electrons, backscattered electrons, X-rays, heat and light will be formed. Detectors collect backscattered electrons and secondary electrons and convert them into a signal that is sent to a screen where the image is formed.

The backscattered electrons are primary electrons coming out from the surface because of scattering events without significantly changing their original energy. The backscattering yield depends on the atomic number of the interacting atom, thus an image contrast show different phases made with different atoms. Another type of contrast can be created from topographic irregularities (i.e. the surface roughness) which deviates the primary electrons towards different directions. The spatial resolution of backscattered electrons is about 1μm. Secondary electrons are emitted from excited atoms. Since their energy is much smaller than that of backscattered electrons, only those electrons within 100 Å from the surface can be collected. The Energy Dispersed X-ray Spectroscopy (EDS) studies the X-ray radiation produced by the interaction between electron beam and atoms of the sample. When an excited core electron decays, a x-ray with a specific wavelength is emitted. The wavelength of the radiation depends on the transition level and it is a fingerprint of the emitting atom. By analyzing the X-ray emission one can semi-quantitatively analyze the film stoichiometry and the composition of secondary phases on the surface.

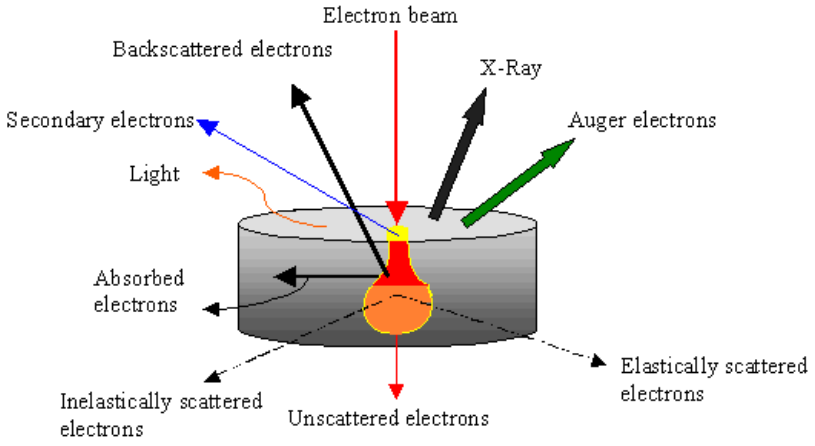

Fig. 4.11 – Interaction between the e-beam and the sample surface

4.7.3 Rutherford Back Scattering (RBS)

The RBS is an ion scattering technique that is used for compositional thin film analysis. RBS allows quantification without the use of reference standards. During an RBS measurement, high-energy (0,1 – 3 MeV) He^{2+} ions are directed onto a sample and the energy distribution and yield of the backscattered He^{2+} ions at a given angle is recorded. Since the backscattering cross section for each element is known, it is possible to obtain

qualitative and quantitative depth profiles from the RBS spectra (for thin films that are less than 1mm thick). It is based upon the elastic two-particle scattering of energetic ions with sample atoms via the repulsive Coulomb force of the positively charged atomic nuclei. The ions penetrate into the matter and lose their kinetic energy, at the beginning mainly in collisions with electrons until they come to rest in a depth of several micrometers. At the surface a very small fraction of the ions approach atomic nuclei close enough to be scattered at large angles. Backscattered ions can leave the sample and reach a particle spectrometer, where their energy is analysed.

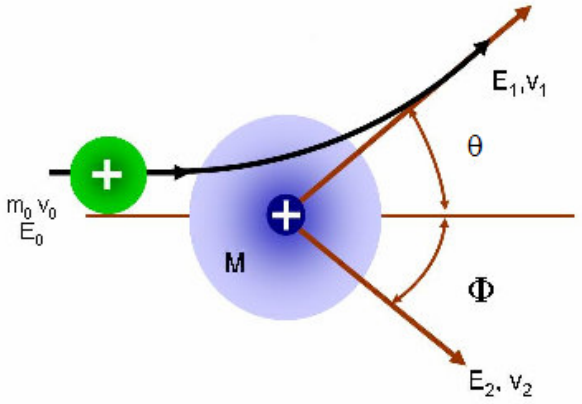

Fig. 4.12 – schematic interaction between ions and atoms of thin film in RBS system

For scattering at the sample surface, the only energy loss is due to momentum transfer to the target atom. The ratio of the projectile energy after and before a is defined as the kinematic factor:

$$K = \frac{E_1}{E_0} = \left(\frac{m_0 \cos\theta + \sqrt{M^2 - m_0{}^2 sen^2\theta}}{m_0 + M} \right)^2 \qquad \text{(Eq. 4.4)}$$

where E_1 is the energy of the ion after the impact, E_0 is the incident ion energy, m_0 is the mass of the projectile ion and M is the mass of the atom target. Knowing the geometry of the system, one can draw the mass (and hence the type) of the atom hit by the projectile.

Besides atom identification, the RBS can also detect the depth profiling of the atoms in the sample. This is due to the energy that a particle loses when it backscatters from an element at some depth in a sample. When probing particles penetrate to some depth in a dense medium, projectile energy dissipates because of interactions with electrons (electronic stopping) and glancing collisions with the nuclei of target atoms (nuclear

stopping). Effectively, these particles have measurable less energy than a particle which backscatters from the same element on the sample surface. The amount of energy a projectile loses through the sample depends on the projectile type, its velocity, the chemical composition and the density of the sample material. Dedicated application program have been studied to calculate and simulate different stopping power in order to interpret the very intricate data collected from multi-layer systems.

4.8 Results on doped-CeO_2 deposited by e-gun

In order to study the effect of both iso-valent (4+) and hetero-valent (3+) substitutional atoms on the properties of CeO_2 layer, four doped-ceria series with different amounts of the doping species have been tested:

1) $Ce_{1-x}Sm_xO_2$, x = 0,03 and 0,06
2) $Ce_{1-x}Yb_xO_2$, x = 0,10; 0,15; 0,25 and 0,45
3) $Ce_{1-x}Zr_xO_2$, x = 0,10 and 0,15

4.8.1 Structural properties

The structural features have been studied by XRD. The out-of-plane orientation has been analyzed by the θ/2θ XRD pattern and rocking curves, while the biaxial orientation degree has been evaluated by pole figures. In **tab. 4.3** a summary of crack-free sample results is presented (in bold the most attractive).

Composition	**Mismatch with Ni-W**	**(200) Orientation degree**	***Out-of-plane (Δω FWHM)***	***In-plane (Δφ FWHM)***	**Critical thickness (t_c)**
Pure-CeO_2	8,4 %	100%	4,8 °	6,0 °	≤ 100 nm
CeO_2 (Sm 3%)	8,5 %	**99,7%**	5,2 °	7,0 °	> 210 nm
CeO_2 (Sm 6%)	8,6 %	**98,7%**	5,9 °	**6,0** °	**> 260 nm**
CeO_2 (Yb 10%)	8,2 %	**99,4%**	6,2 °	6,5 °	150 nm
CeO_2 (Yb 15%)	8,2 %	**99,9%**	6,2 °	6,5 °	125 nm
CeO_2 (Yb 25%)	8,1 %	**99,9%**	5,0 °	6,5 °	150 nm
CeO_2 (Yb 45%)	**7,5 %**	**99,5%**	**2,7** °	**5,0** °	**> 200 nm**
CeO_2 (Zr 10%)	8,3 %	**99,6%**	5,0 °	7,0 °	> 100 nm
CeO_2 (Zr 15%)	8,2 %	**99,9%**	**4,0** °	8,0 °	> 250 nm

Tab. 4.3 – Summary of doped-ceria best samples

The orientation degree of the (200) direction relative to the others eventually present is calculated by means the ratio between the (200) intensity line and the sum of the latter and the other peaks taken into consideration. Every peak-line is normalized to a reference XRD powder spectrum of the compound analyzed. In the table above it is clear that the doping permits degree of orientation along (200) direction as high as in pure-Ceria compound.

The values of critical thickness showed in the last column might be underestimated since they are not theoretical calculation but values measured by alpha-step profilometer in our laboratories evidencing no cracks formation for the reported layer thickness. They highlight that critical thickness enhancement has been reached by CeO_2 doping.

As well-know in many research works presented in paragraph **4.5**, also for our deposition tests, the reasons for the critical thickness behaviour as a function of type and amount of doping have been verified. Structural improvement plays a key role in these compounds, but mechanical properties are not less important. Indeed, using Yb^{3+} as dopant, the mismatch with the substrate decreases from 8,4% to 7,5% varying the doping proportion.

The same effect has been found in the compound doped with Zr^{4+}. Although in this case it is limited to only one tenth of a percentage point and cannot justify the great increase in *tc*.

Surprisingly, in the case of Sm doping the opposite phenomenon occurs: the mismatch with Ni-W is slightly higher moving up to 8,6% but the highest critical thickness (more than 260 nm) is reached. We can attribute this effect to the increased fracture toughness which is therefore related to an increase in mechanical properties of the material, probably generated by the crystal lattice of defects provided by oxygen vacancies. These defects allow the growing layer to accumulate greater amounts of elastic energy, thanks to a higher "flexible ability" given by a different distribution of bonding energies.

Returning to, It is important to emphasize that the change of the lattice parameter is consistent with the bibliographic data presented for all the three dopant. The experimental measures were made on the basis of the diffraction pattern obtained by X-ray Bragg-Brentano geometry, taking as reference peak (200) of ceria, as shown in **fig. 4.13**. The shift of this peak toward higher angles corresponds to a crystalline cell contraction and then to a smaller mismatch with the substrate for Yb^{3+} and Zr^{4+}, while Sm^{3+} doping involves a reduction of the diffraction angle corresponding to an enlargement of the elementary cell and subsequently a mismatch increase with Ni-W substrate.

The calculation of the (200) peak shifts of doped-CeO_2 relative to pure CeO_2 has been measured fixing the (200) Ni-W peak as reference and normalizing the other peaks.

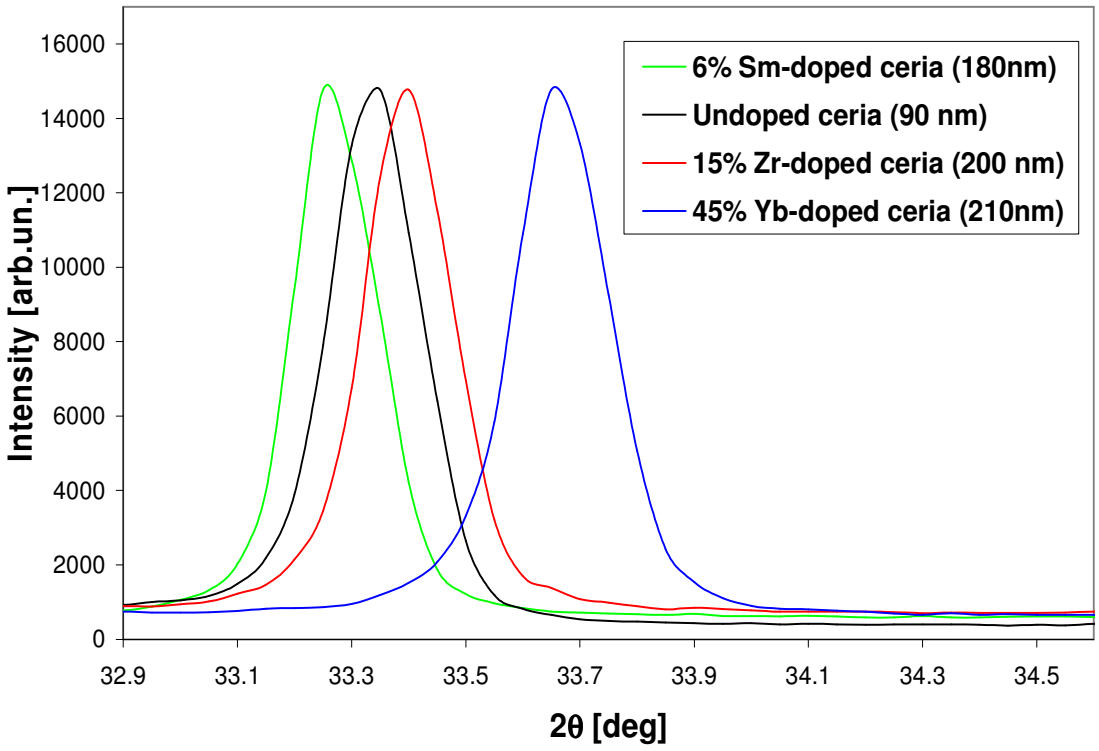

Fig. 4.13 – Peak shifts taken from θ/2θ XRD pattern of doped CeO_2 relative to pure CeO_2 compound

The most interesting results were obtained for 6at.%Sm^{3+}, 45at.%Yb^{3+} and 15at.%Zr^{4+} doping which permit to grow samples characterized by very good values of bi-axial texturing and high thickness, maintaining a compact crack-free structure.

The spectra of X-ray diffraction in θ/2θ geometry of these tapes, shown in **fig. 4.14, 4.15 and 4.16**, confirmed that (h00) plans of the buffer layer are correctly parallel-aligned to the surface of the tape.

The analysis of these data indicates also that in most cases the addition of trivalent and tetravalent cations to CeO_2 compound allows to keep the fluorite-type crystalline structure of Ceria and does not lead to the formation of unwanted secondary phases, which would prevent optimal epitaxial growth of YBCO superconducting layer. In only one case a secondary phase of ZrO_2 has been noticed after the growth at low temperature but thanks

to a brief annealing treatment at 600°C in oxygen atmosphere it disappeared. This might be due to the solubility limit of the Zr^{4+} in CeO_2 system and will be deepen in next studies.

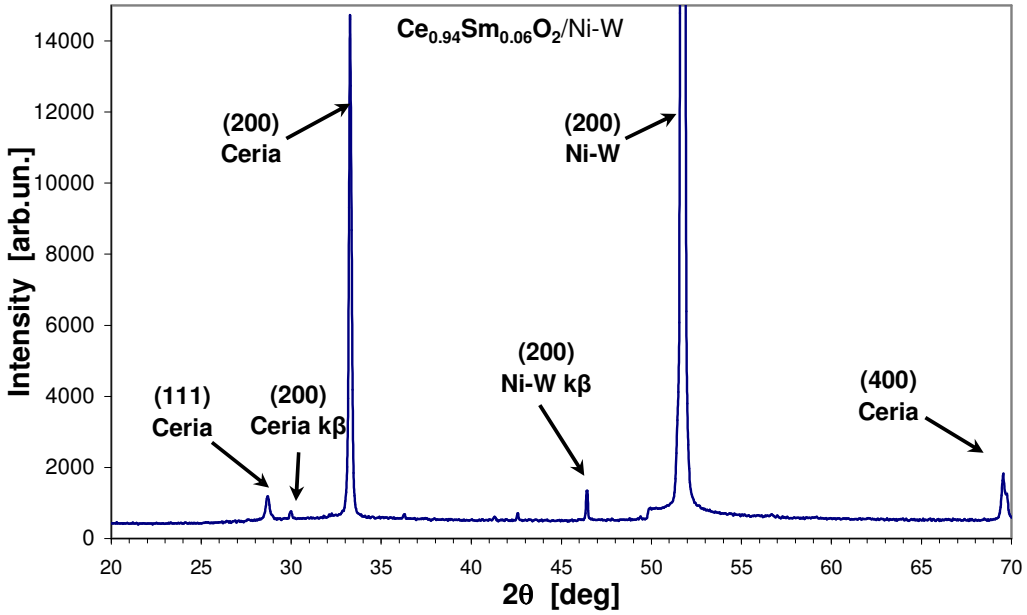

Fig. 4.14 – θ/2θ XRD pattern of Sm-doped CeO_2 ($Ce_{0,94}Sm_{0,06}O_2$)

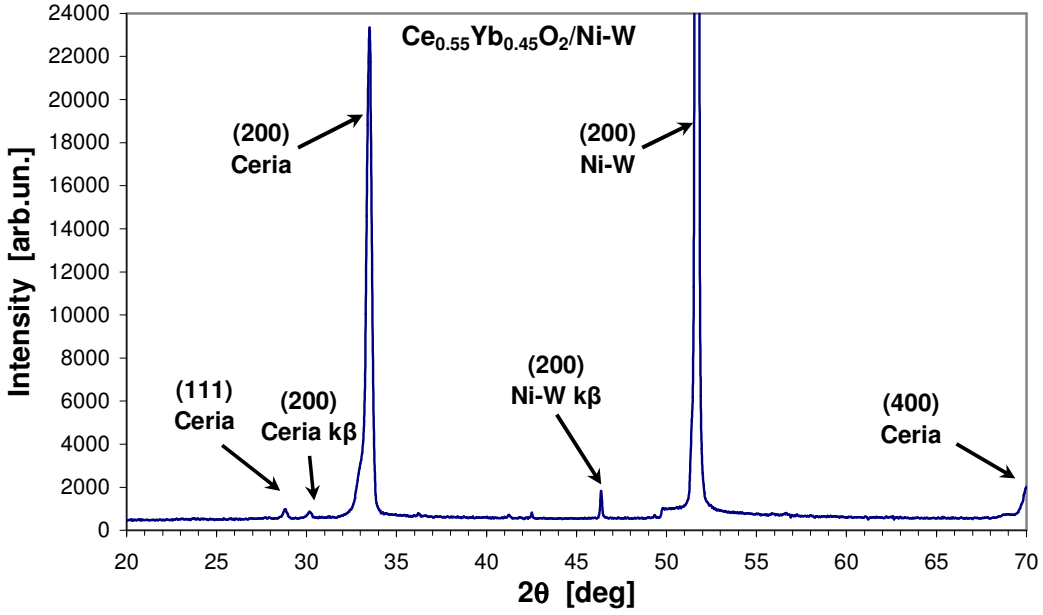

Fig. 4.15 – θ/2θ XRD pattern of Yb-doped CeO_2 ($Ce_{0,55}Yb_{0,45}O_2$)

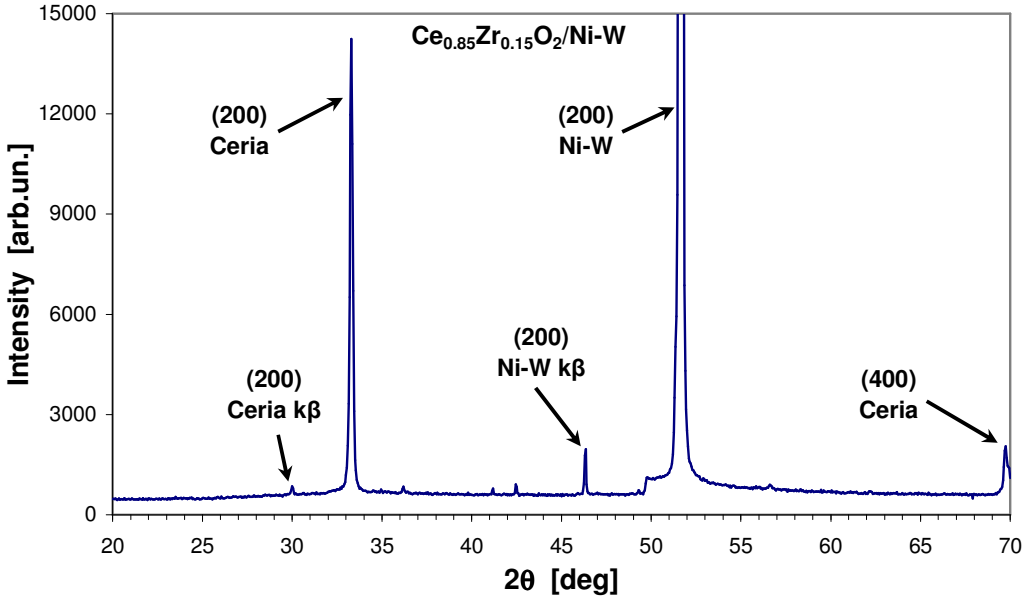

Fig. 4.16 – θ/2θ XRD pattern of Zr-doped CeO_2 ($Ce_{0,85}Zr_{0,15}O_2$)

The values on the orientation in-plane and out-of-plane have been derived from rocking curves and pole figures (**fig. 4.17, 4.18, 4.19**) that show a high degree of bi-axial texturing, expressed by the Δω and Δφ average below 5° and 6,5°, with a minimum at 2,75° and 4° respectively for Yb^{3+} and Zr^{4+} doped samples. These features are particularly significant in order to guarantee the optimal texturing properties that the buffer layer have to transmit to the next layer of YBCO. Indeed, only in this case superconducting layer can reach the ideal shape to achieve high critical current values.

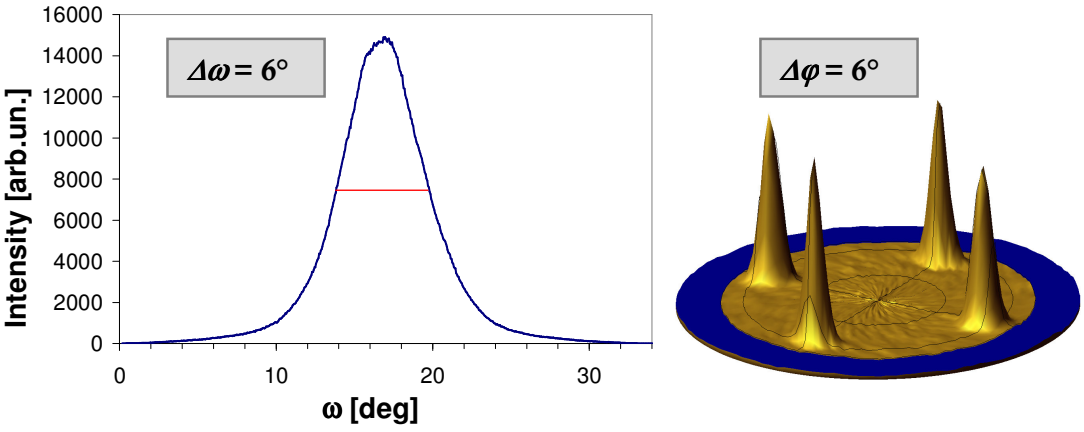

Fig. 4.17 – Rocking curve (on the left) with a Δω = 6° and pole figure (on the right) with Δφ = 6° of a $Ce_{0,94}Sm_{0,06}O_2$ grown on Ni-W RABiTS™ tape

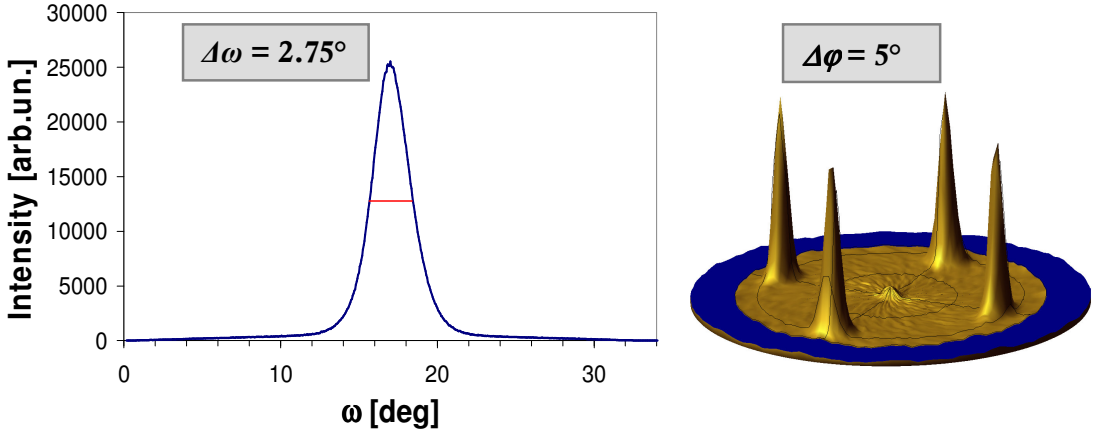

Fig. 4.18 – Rocking curve (on the left) with a Dw = 2,75° and pole figure (on the right) with Dj = 5° of a $Ce_{0,55}Yb_{0,45}O_2$ grown on Ni-W RABiTS^{TM} tape

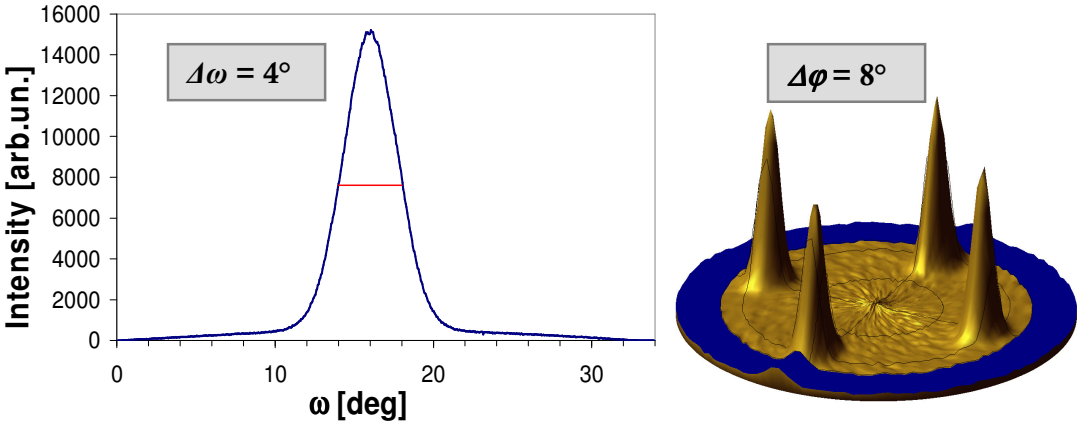

Fig. 4.17 – Rocking curve (on the left) with a Δω = 4° and pole figure (on the right) with Δφ = 8° of a $Ce_{0,85}Zr_{0,15}O_2$ grown on Ni-W RABiTS^{TM} tape

4.8.2 Morphological and compositional properties

SEM analysis show that the doped-CeO_2 layer grew highly homogeneous and compact as can be seen from the figures **4.18 to 4.20**. Few flaws can be noticed such as micro-pores and longitudinal grooves onto the surface. They are already present in the substrate likely produced during the rolling process of the tape. In samples with a thickness less than 150 nm one can also glimpse the pattern of bi-axial texturing typical of the RABiTS^{TM}.

Measurement has been made at IMEM-CNR (Parma) using a Philips-515 equipped with microanalysis EDAX system and a JEOL JSM-5009 LV located at R&D laboratories of EDISON s.p.a. in Trofarello (TO).

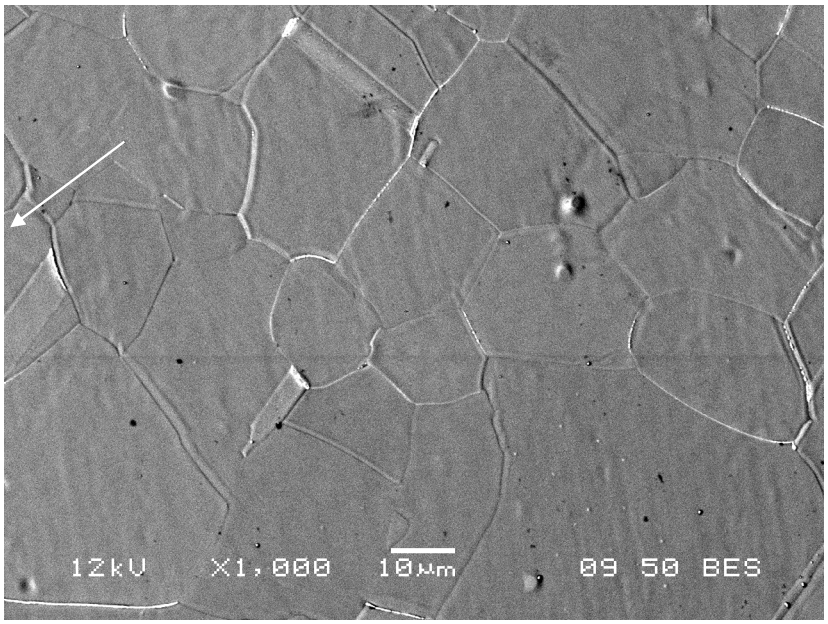

Fig. 4.18 – SEM image of 180 nm thick $Ce_{0,94}Sm_{0,06}O_2$ sample grown on Ni-W RABiTS^{TM} tape

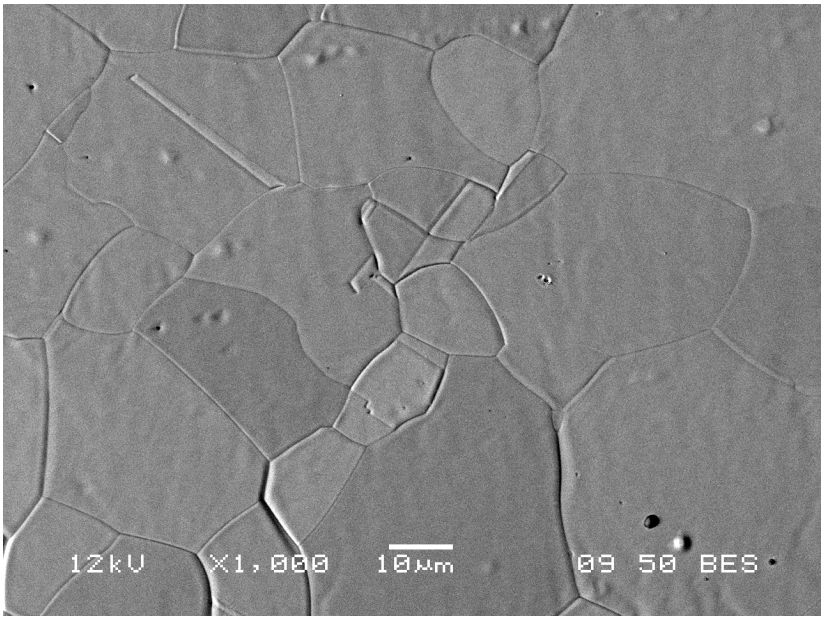

Fig. 4.19 – SEM image of 200 nm thick $Ce_{0,55}Yb_{0,45}O_2$ sample grown on Ni-W RABiTS^{TM} tape

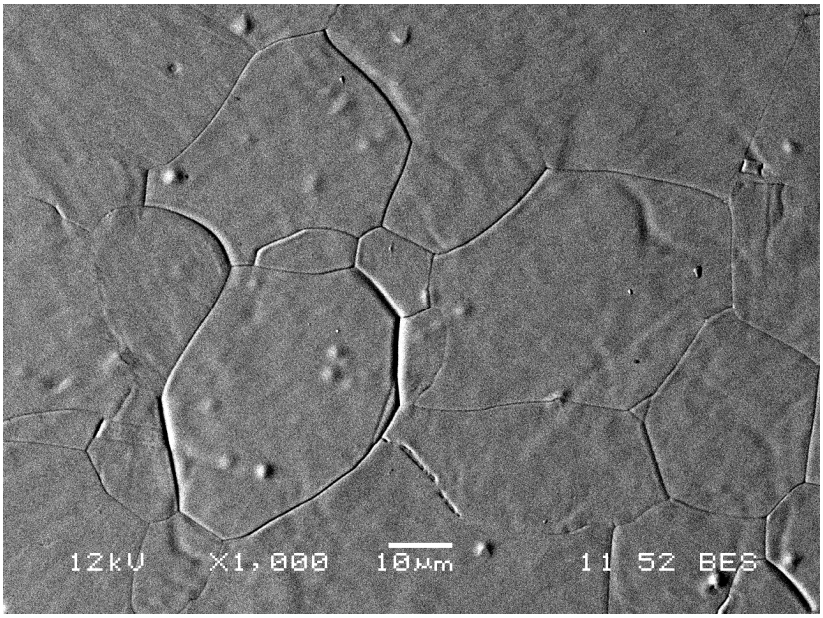

Fig. 4.20 – SEM image of 120 nm thick $Ce_{0,85}Zr_{0,15}O_2$ sample grown on Ni-W RABiTS^{TM} tape

All the SEM images presented show a smooth and crack-free deposited layer demonstrating the goodness of the doping method choice to enhance the critical thickness of CeO_2 to obtain a single buffer layer architecture for low-cost CC.

Some problems related to the stoichiometric control have been revealed by EDS analysis: all the samples showed a remarkable difference on dopant concentration compared with the target. This is due to the different melting point (Mp) of the oxides mixed and sintered in the target. Hit by the e-beam, the oxide with the lower melting temperature evaporates before the other, leading to a non-optimal stoichiometric transfer from the target to the film. Indeed, ZrO_2 presents a Mp of 2750°C, 450°C higher than CeO_2, explaining the low percentage of Zr in the film which is around 5% starting from a target prepared with 10%. An opposite case occur in Yb-doped CeO_2 films where Yb appears in little excess because of its lower Mp (2200°C) than Ceria.

To better the control of the stoichiometry of the film deposited the novel technique PED, described in **paragraph 2.2**, will be used for the next series of deposition. Based on high energy density of deposition process, this technique can perform an optimal chemical composition transfer from target to the substrate.

4.8.3 Effective barrier ability

The possible diffusion of Ni through the buffer layer has been analyzed by RBS analysis. As reported in section 4.4, Ni can easily diffuse into thin layers of pure ceria grown with a thickness lower than 100 nm. The main risk is related to the Ni diffusion up to the buffer surface where it can "touch" YBCO layer polluting it and deteriorating its superconducting properties. On the contrary, RBS data confirm that no traces of Ni have been found on the surface of doped-CeO_2 layer (thickness ~150 nm), revealing the excellent performance of this material as a barrier against chemical interdiffusion between the substrate and the superconductor layer. Such behaviour may be due to the introduction of defects that prevent the passage of Ni or drive metal atoms along privileged path, for example, toward the grain boundaries. Further analysis of the structure crystalline buffer layer, for example Transmission Electron Microscopy (TEM) or high resolution XRD, are necessary to clarify the mechanism on which high critical thickness and high barrier effect find their origin.

From the spectra reported in **fig. 4.21** it is interesting to note the distribution of Ni for different buffer layer of pure ceria film with a thickness of 100 nm (crack-free) and one of about 200 nm (cracked), respectively. In the blue and red circles, the diffusion of Ni-atoms into the buffer is detected as a little edge of the signal (in red circle). As one can see, the sample called Parma A (black line) show the presence of Ni atoms in surface because the Ni signal is exactly as the theoretical one, defined as a pure-Ni surface. The Parma B sample (red line) show the typical Ni-edge (blue circle) at a lower energy indicating the presence of Ni inside the buffer but not up to the surface. In conclusion, Ni spreads within the layer in both cases but without reaching the surface in the thicker film. Therefore one can assume that these cracks do not form during the deposition of CeO_2 layer but later, when the tape is cooling down and Ni-atoms do not have enough mobility to diffuse through the cracks of the material and to reach the surface of the buffer. This could provide an explanation about the crack formation mechanism. In this case the latter will be related to different thermal expansion coefficient rather than the existing mismatch between Ni-W and CeO_2. Further evidence, carried out by setting different ramps drop in temperature or in-situ high esolution XRD or SEM analysis , will clarify this behaviour.

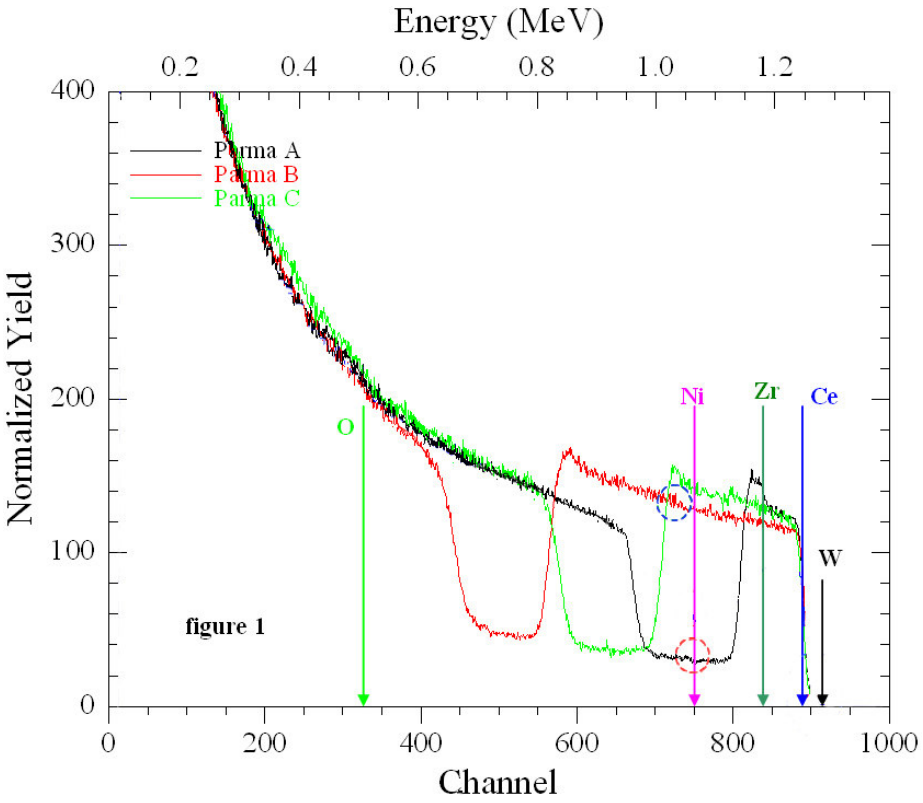

Fig. 4.21 – RBS analysis results for three samples: in black, Parma A is 100 nm thick sample of pure-CeO_2, in red, Parma B is a 250 nm thick and cracked sample of pure-CeO_2 and in green Parma C is a 150 nm thick sample of $Ce_{0,85}Zr_{0,15}O_2$

4.8.4 The final test: properties of YBCO grown on the single buffer

Obviously, high performance YBCO layer deposited onto doped-Ceria is the crucial test to demonstrate that the single buffer layer is a reliable template for low-cost HTS-CC. In this way the buffer layer has to support all the mechanical and thermal stresses due to the deposition process of the whole Coated Conductor. The growth technique chosen in our project is the thermal co-evaporation because allow a low temperature and large area deposition process for long length CC.

After the annealing and the deposition of doped-Ceria buffer layer, the deposition step of the superconducting layer is realized thanks to the simultaneous evaporation of Y, Ba and Cu from ultra-pure metal chips located in three different Molybdenum crucibles heated by Joule effect (described in section 2.1.2)

The optimal ratio of co-evaporated material is controlled by an Atomic Absorbance Spectroscopy (AAS) system that allow the automatic regulation of electric power necessary to keep the 1:2:3 ratio of the atomized metals (**fig. 4.22**).

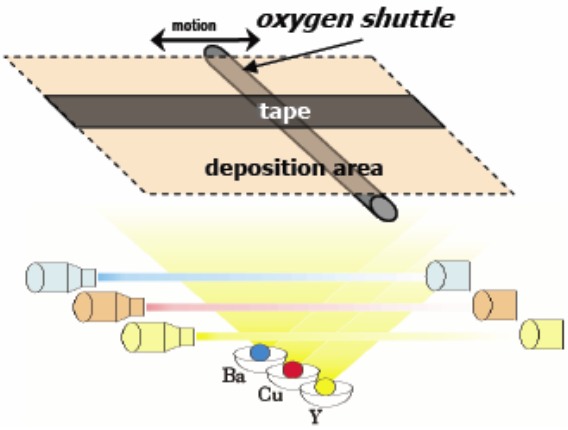

Fig. 4.22 – Schematic thermal co-evaporation (TCE) system for depositing YBCO layer

In addition to the evaporated metals, an oxygen supply has to be provided close to the growing YBCO layer in order to obtain the Tetragonal phase that will be transformed in the Orthorombic I after the last cooling process in 500 mbar of O_2 (**fig 4.23**)[22].

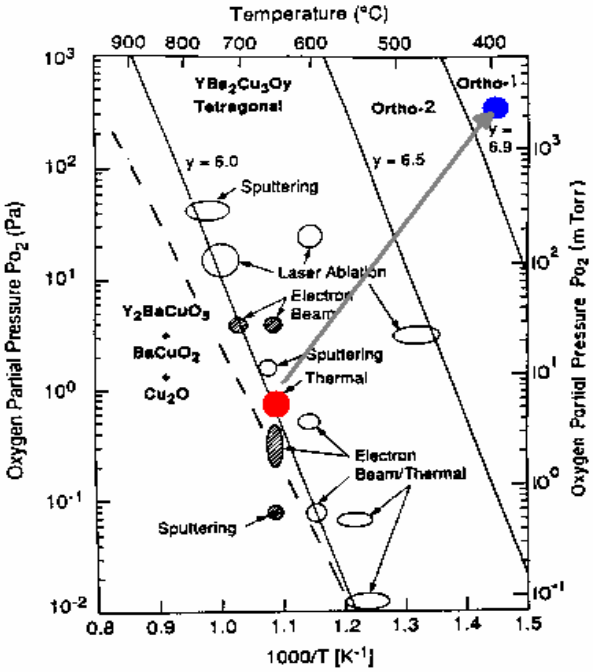

Fig. 4.23 – Phase diagram of tetragonal YBCO deposition by TCE (red circle) and cooling in O_2 atmosphere to obtain Ortho I HTS phase (blue circle)

The main problem of the oxygenation is related to the oxygen partial pressure that must be kept during the YBCO deposition. According to the phase diagram presented in **fig. 4.23**, the oxygen partial pressure should be about 10^{-2} mbar[23], too high for molecular regime of epitaxial deposition which can be maintained up to 10^{-4} mbar. This value has been achieved thanks to a little moving device placed nearly the tape where the oxygen pressure can be enhanced up to 10^{-2} mbar leaving the background pressure unchanged at 10^{-5} mbar. In our laboratory great efforts have been spent to modify this devices and excellent results will be shown. Indeed, the old "oxygen pocket[24]" developed by Theva GmbH showed different mechanical issues related to its excessive proximity to the tape (0,2 mm). This was necessary to obtain an effective oxygenation during the growing YBCO, but the relatively high temperature in that area caused expansion and arching of the devices that often hit the substrate, or its holder, during the back and forward movement. This item has been improved to enlarge the distance from the substrate and, at the same time, keeping the oxygen supply ability by means the study and the applications of supersonic gases expansion. With the novel system called SNEO (**fig. 4.24**) (Oxygenation Enhancement by a Supersonic Nozzle)[25,26], the distance between the oxygen supply and the tape has been increased without varying the effectiveness of the oxygenation process. Indeed, SNEO can effectively work up to 1 cm far from the substrate, thus avoiding the issues relative to the old oxygen pocket.

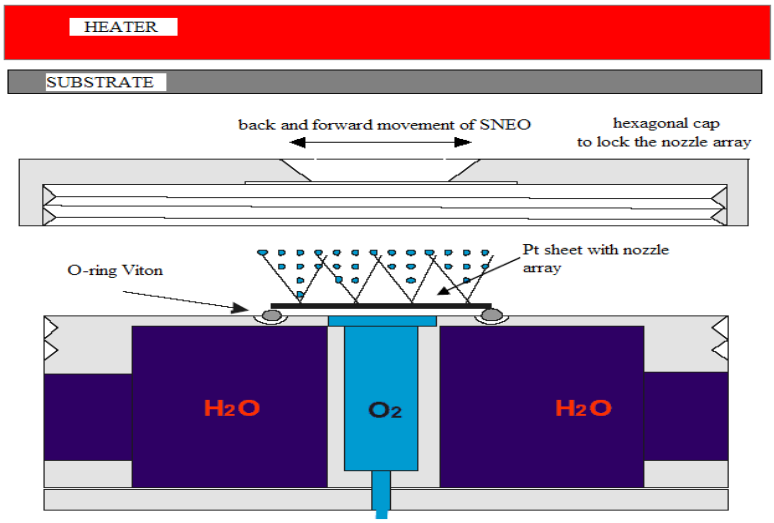

Fig. 4.24 – SNEO devices for YBCO oxygenation during the growth
(patent application no. WO/2005/024088)

Further studies on SNEO led to some modification in gas-type used and better results have been obtained with a He-O_2 mixture for oxygenation. The simultaneous use of SNEO with 30%He-O_2 and doped-Ceria single buffer layer, led to astonishing results. Analyzing on a short sample of 5 cm, structural properties of YBCO showed high orientation degree and high out-of-plane growth direction. The presence of only CeO_2 and YBCO peaks confirms the absence of undesired secondary phases. In addition, the absence of Ni or NiO peaks reveals the maintained goodness of the doped-CeO_2 single buffer layer also during the YBCO growth process. Moreover, from quantitative analysis extracted by XRD, an excellent oxygenation degree has been reached obtaining an YBCO phase optimally doped: $YBa_2Cu_3O_{7-\delta}$ where δ=0,12.

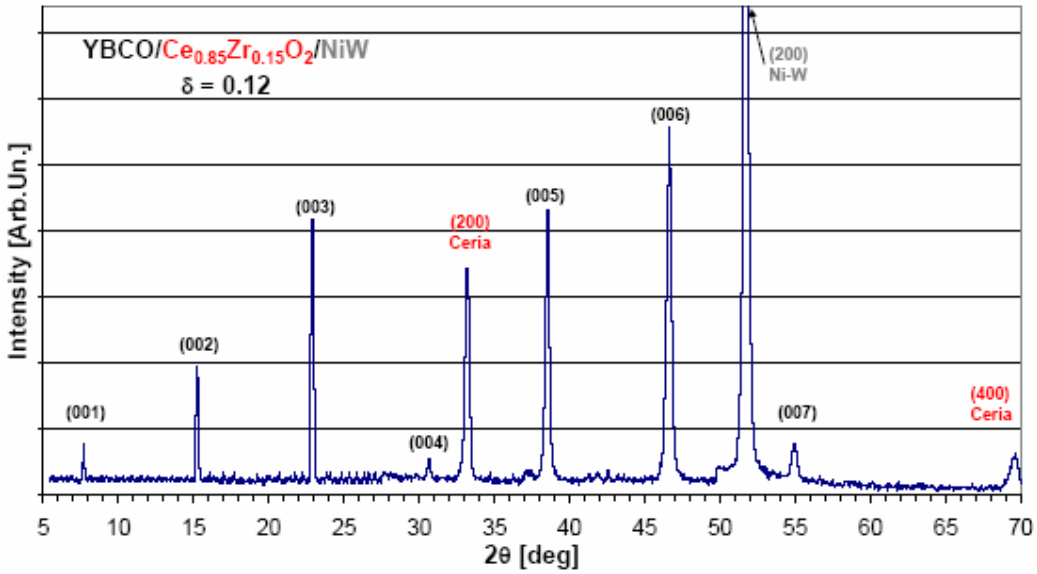

Fig. 4.25 – XRD pattern of YBCO/$Ce_{0,85}Zr_{0,15}O_2$/NiW short CC

Remarkable electrical properties have been measured on this sample showing a Tc_0 value of 90,5 K (the highest obtained over all the samples produced in this 8 years-project) by typical van der Paw four probes contact measurements[27]. The R-T graph reported below (**fig. 4.26**) show other interesting information, such as the ΔTc, i.e. the range where the transition occurs, of only 1 K and the RRR parameter (Residual Resistance Ratio, defined as the ratio between resistance value at 300 K and at 100 K) with a value of 3, index of a perfect metallic behaviour in function of the temperature.

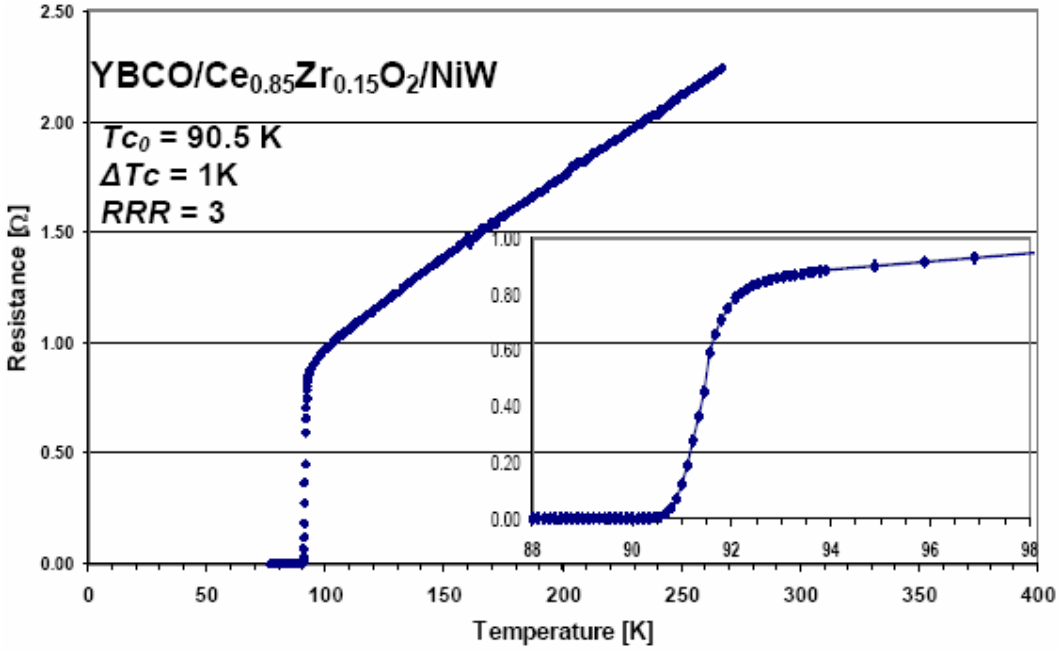

Fig. 4.26 – Four contact probes R-T graph shows a Tc_0 of 90,5 K for a YBCO/$Ce_{0,85}Zr_{0,15}O_2$/NiW

The inductive measurements provide an estimate of the critical current density, Jc, in the YBCO films. Typical values are in the 0,6 MA/cm^2 range at 77 K self field but this feature appears underestimated because of the sizable magnetic response of the Ni-W substrate.

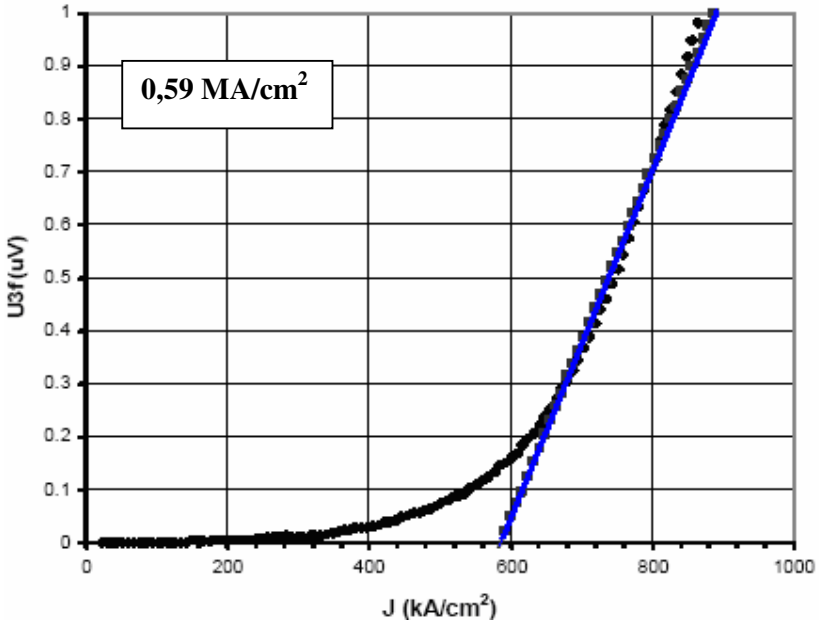

Fig. 4.27 – Inductive measurements of Jc for a YBCO/$Ce_{0,85}Zr_{0,15}O_2$/NiW

Very good electrical properties have been measured on another HTS-CC sample fabricated on a Ybat.45% -Ceria doped buffer layer, keeping the same growth and oxygenation condition for YBCO layer.

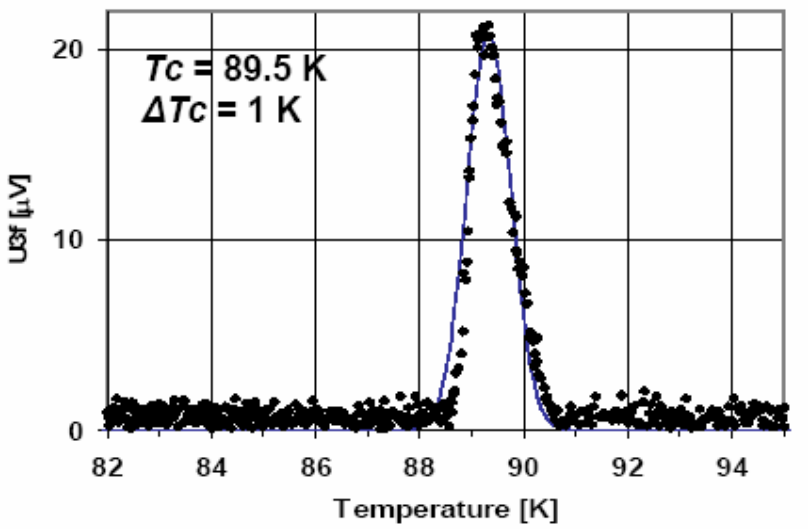

Fig. 4.28 – Inductive measurements showing a Tc_0 value of 89,5 K for a YBCO/$Ce_{0,55}Yb_{0,45}O_2$/NiW

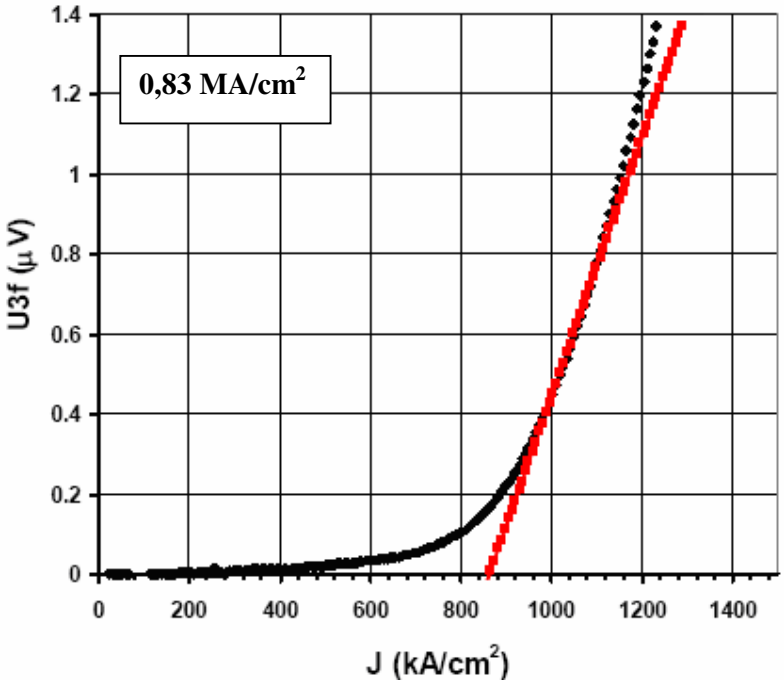

Fig. 4.29 – Inductive measurements of Jc for a YBCO/$Ce_{0,55}Yb_{0,45}O_2$/NiW

From **figures 4.29 and 4.29**, The critical temperature (Tc) reached a value of 89,5 K (obtained by conductive measurements) with a ΔTc of only 1 K. Inductive measurements gives a Jc value of 0,83 MA/cm^2. Considering the thickness and the width of YBCO layer, 0,6 μm and 6 mm respectively, the Ic value obtained is 36A.

By applying an external magnetic field (B) perpendicular to YBCO surface, we evaluated the behaviour of critical current flowing in YBCO/$Ce_{0,55}Yb_{0,45}O_2$/NiW short sample in function of increasing B.

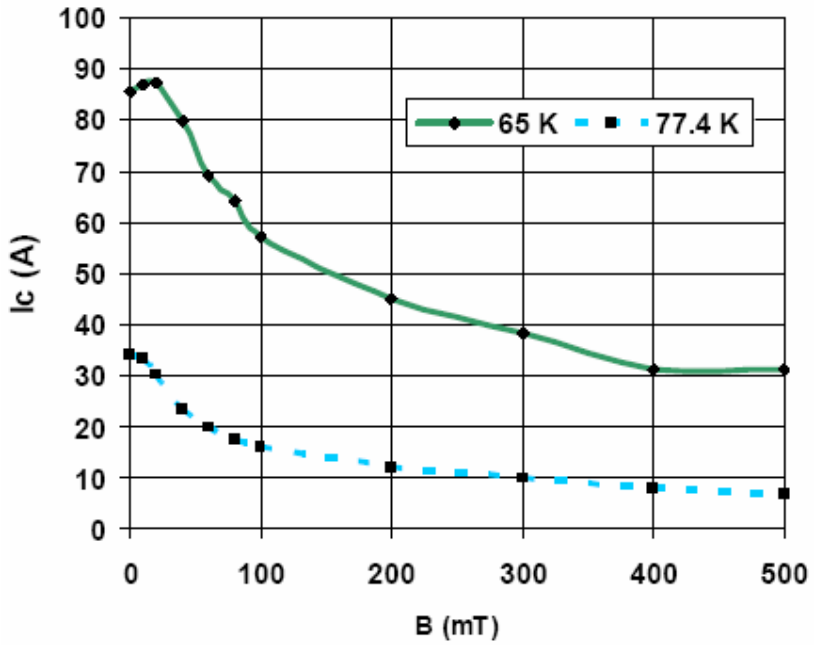

Fig. 4.30 – Critical current trend as a function of external magnetic field applied long YBCO c-axis at 65 K and 77 K

Cooling-down the samples by pumping liquid Nitrogen, a temperature of 65 K has been reached and Ic value of 87 A has been measured[28-30]. Once applied the external field the decrease of Ic as a function of B followed the typical trend of state-of-the-art samples realized by other research group.

4.9 Experimental procedure: doped-Ceo_2 grown by PED

In order to improve the deposition rate and the stoichiometric transfer from the target a novel deposition technique has been chosen for long length and low cost Coated Conductors. This is called Pulsed Electron Deposition (PED) and it has been deeply explained in chapter 2. The main features of this technique are the relative low installation and running costs and the excellent stoichiometric transfer from target to the growing film. Starting from the remarkable results obtained with e-gun thermal evaporation, we tried to further improve the doped-Ceria single buffer layer by optimizing the doping transfer using a different deposition technique. In addition, the same pulsed source could be used to deposit YBCO layer, as made by other research groups[31-33].

First, we designed and realized a more compact and efficient graphite heater and installed it and the source for PED in the deposition chamber already present in our laboratory[34]. Then we prepared new type of doped-CeO_2 target pressing the mixed powders at higher pressure (up to 280 bar) with larger diameter (18-25 mm) to reach greater toughness to face the high energy electron pulses and larger area to hit. The sintering step was then defined with lower slope and a longer high temperature (1300°C) time to avoid through-passing crack formation during heating and cooling.

The pre-annealing step has been performed as in e-beam evaporation experiments: biaxially textured Ni-5 at.%W alloy substrates are annealed in 10 mbar of forming gas at 600 °C for 60 minutes. Depending on the different targets, the experiments have been realized with an electron beam accelerating voltage of 14-18 kV, a discharge current of 1-2 mA and pulse frequency in the range of 2-8 Hz. PED operates with O_2 as discharge source and in a O_2 background pressure of 10^{-4} mbar. All the doped-CeO_2 deposition have been performed in the range of 650-700°C followed by a post-oxygenation treatment at 10^{-4} mbar during the cooling.

For these series of deposition, the composition that brought the best results in e-beam evaporation (with Yb and Zr), the deposition of pure ceria and Ta-doped have been tested:

1) $Ce_{1-x}Yb_xO_2$, x = 0,45
2) $Ce_{1-x}Zr_xO_2$, x = 0,10 and 0,15
3) pure CeO_2
4) $Ce_{1-x}Ta_xO_2$, x = 0,10 and 0,20

The new added test shas been performed to evaluate both pentavalent ion dopant like Ta^{5+} to improve dielectric properties[35] of CeO_2 and pure Ceria grown by PED to test a different deposition technique on its critical thickness.

4.10 Results for doped-CeO2 grown by PED

4.10.1 Structural properties

The structural features have been studied by XRD. As previously discussed, the out-of-plane orientation has been analyzed by the θ/2θ XRD pattern and rocking curves, while the biaxial orientation degree has been evaluated by the polar figures.

The **table 4.4** reported below summarizes the best results obtained by doped-Ceria grown via PED, bold emphasizes remarkable results.

Composition	**Mismatch with Ni-W**	**(200) Orientation degree**	***Out-of-plane (Δω FWHM)***	**Dielectric strength @ 77 K (MV/cm)**	**Critical thickness (t_c)**
CeO_2 (Yb 45%)	**7,3%**	**99,8%**	**5,2 °**	5,0	**700 nm**
CeO_2 (Zr 10%)	7,5%	**99,3%**	7,8 °	5,2	500 nm
CeO_2 (Zr 15%)	7,5%	**99,7%**	6,2 °	**> 5,9**	> 500 nm
CeO_2 (Ta 10%)	7,6%	98,6%	6,7 °	4,1	550 nm
CeO_2 (Ta 20%)	7,6%	95,6%	7,8 °	3,9	400 nm
Pure CeO_2	8,4%	**99,8%**	5,5 °	0,3	**150 nm**

Tab. 4.4 – Summary of some properties measured on doped-CeO_2 samples

As remarked in 4.8 paragraph, doped-CeO_2 proved to be a suitable material for single buffer layer architecture in new development of Coated Conductors. By varying the deposition technique even more interesting results are showed in **table 4.4**. Critical thicknesses increase up to the remarkable value of 700 nm without any cracks. Also in the case of undoped Ceria PED allows the growing of crack-free buffer layer with larger thickness (~ 150 nm) compared to other deposited by different techniques, suggesting the presence of some peculiar effects of the PED technique.

In addition, a further reduction of the lattice mismatch with Ni-W substrate can be calculated by XRD pattern (**fig. 4.31**) despite the use of the same doping elements (Yb and Zr). This could be explained by the better stoichiometric transfer from the target to the film and from the relaxation of mechanical energy stored up during the growth by means disorder and defects. Recalling equation **4.2**, critical stress was written with an inverse proportion respect to the term δ related to the amounts of impurities and defects. Indeed, layers grown by PED, and in general by high energy technique, present some particulate (visible in SEM images presented in next paragraph) on the surface and inside the film that could create active defects in mechanical stress relaxation mechanism. Probably this is the cause of so large thickness reached by these layers.

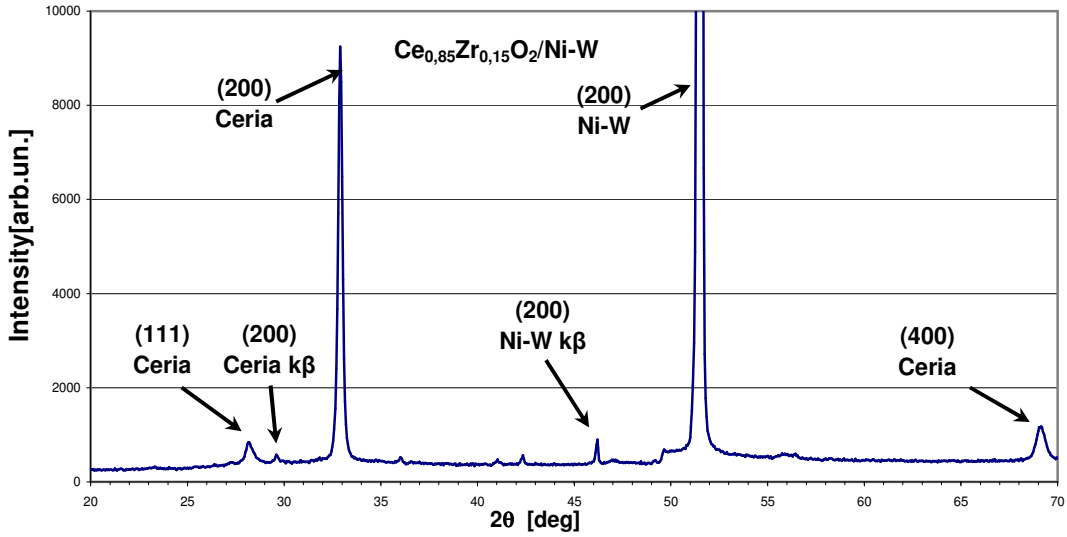

Fig. 4.31 – XRD pattern of $Ce_{0,85}Zr_{0,15}O_2$/Ni-W grown by PED

The test conducted by using Ta^{5+} as dopant did not show the expected results. Observing the **table 4.4** the two Ta-doped samples while keeping the 99% of orientation degree, present a high value of $\Delta\omega$, emphasizing the not optimal out-of-plane orientation. Nevertheless, these samples reached very large thickness of the layers thanks to their very low lattice mismatch with the substrate.

Not so good results are shown in pole figures: for all of the short samples deposited and analyzed the results were those illustrated in **fig. 4.32A**.

The solution that we found was very simple: we start moving a long substrate back and forward with the reel-to-reel system mounted at the ends of the tri-chamber to keep a better uniformity of temperature and deposition area. Contrary to thermal evaporation, PED shows a smaller deposition area and we thought to use the movement to uniform the deposition layer onto the substrate. With this simple but effective idea, we partially solved the in-plane orientation obtaining the pole figure in **fig. 4.3B.** Moreover, we noticed an improvement of orientation percentage in moved tapes respect to the static-way deposition.

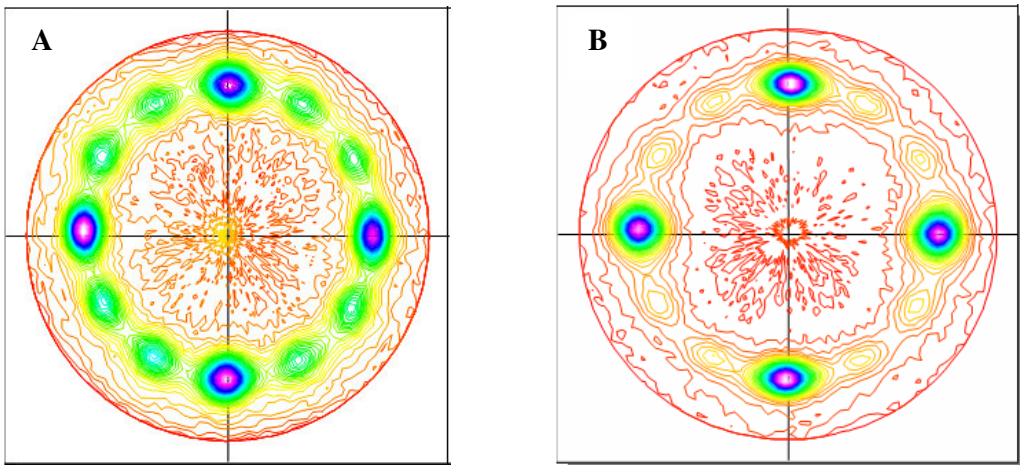

Fig. 4.32 – **A:** pole figure of a short sample of doped-CeO_2 grown by PED in static mode;
B: pole figure of a long sample of the same doped-CeO_2 grown by PED motion mode

The back and forward motion turned out to be very useful also in reducing the amount of particulate on the sample surface due to a dilution on higher length of the tape.

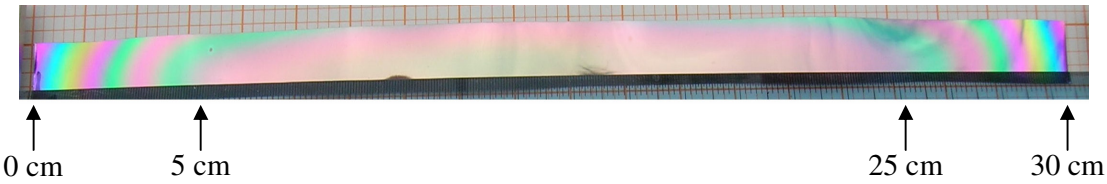

Fig. 4.33 – 30 cm long buffered Ni-tapes. The uniformity region is comprised in the central 20 cm

At the same time, we tested the concrete possibility of long deposition by using PED to fabricate long-length CC. for the duration of the process, we observed the high stability of the plume, adjusting only the background pressure and the oxygen supply to the e-gun.

Some depositions has been performed on long tapes showing a good colour uniformity of the film, index of the thickness uniformity, as we can see in **fig. 4.33**.

4.10.2 Morphological and compositional properties

The SEM images presented in this section show the typical presence of particulate on the surface of layer grown by high energy technique. Moreover the absolute absence of cracks can clearly noticed, despite the very large thickness of the layer grown.

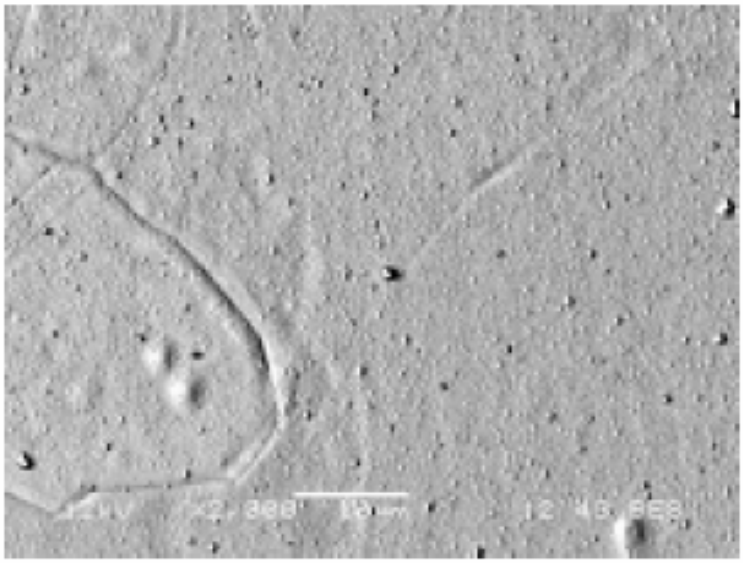

Fig. 4.34 – SEM image of the surfece of $Ce_{0,85}Zr_{0,15}O_2$/Ni-W grown by PED

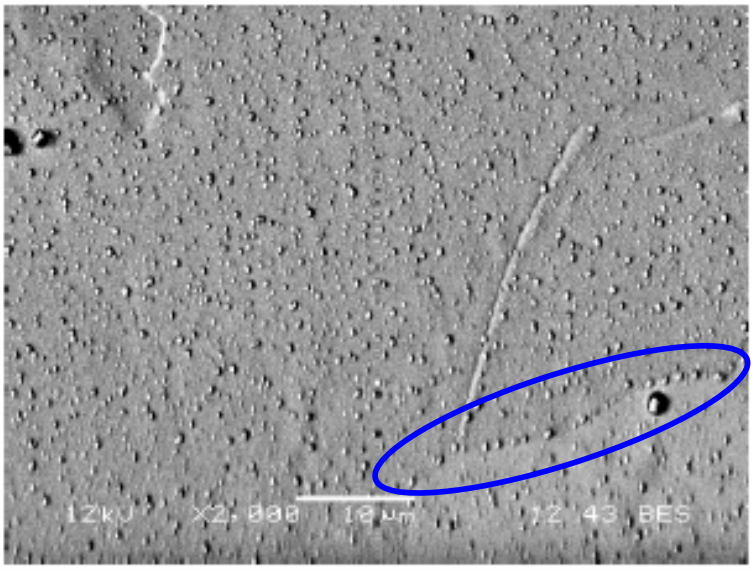

Fig. 4.35 – SEM image of the surface of $Ce_{0,55}Yb_{0,45}O_2$/Ni-W grown by PED. In the blue circle, particulates segregate along a grain boundary

Independently from the dopant type, the presence of particulate on the surface is evident in every sample and it seems to follow the line traced by grain boundaries where one can see a higher droplet density (**fig. 4.35**).

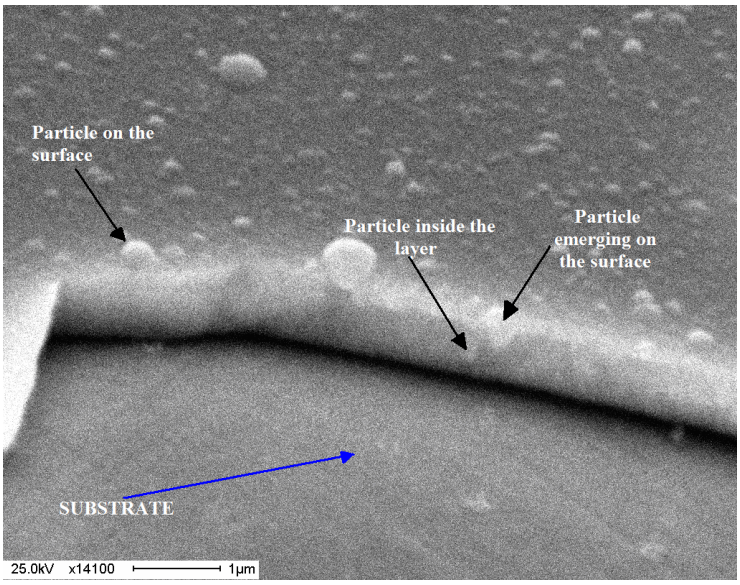

Fig. 4.36 – SEM image of a fracture edge of $Ce_{0,85}Zr_{0,15}O_2$/Ni-W grown by PED to highlight the particle presence inside the layer

4.10.3 Dielectric properties

Another interesting analysis we made on these samples, has been applied to study the dielectric properties of the buffer layer. This feature appears very useful for AC application in Coated Conductors field[36] reducing hysteresis and AC losses in current flow.

By using a home-made device we tested dielectric strength of our samples in liquid Nitrogen by applying an increasing voltage at the ends of the sample. The latter assumes the function of a capacitors and from the value of the voltage that breaks the surface we can calculate the dielectric strength reported in **table 4.4**. In **fig. 4.37** a picture and the electric scheme of the device are shown. The buffered tape is placed between the Cu electrodes connected to the voltage generator and then, the whole item, is put into a cryostat. This is slowly immersed in liquid Nitrogen and at 77 K we increase the voltage step by step. When it reaches the maximum value withstood by the film, suddenly, the latter cracks letting flow the current trough (**fig. 4.38**)

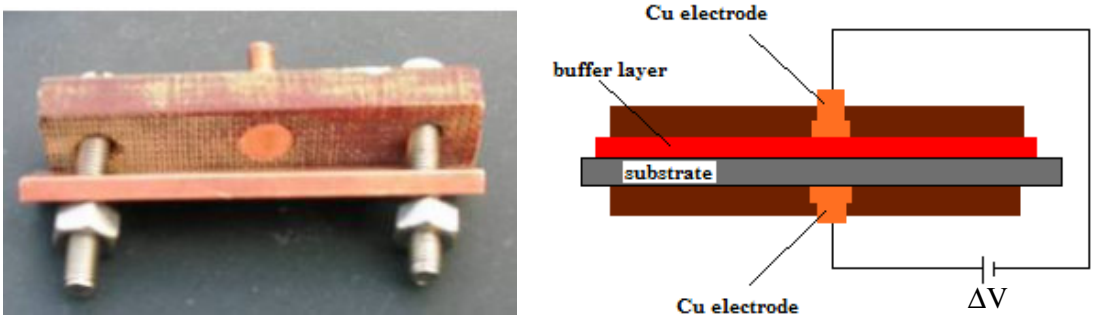

Fig. 4.37 – Dielectric strength measurement device and its schematic electric circuit

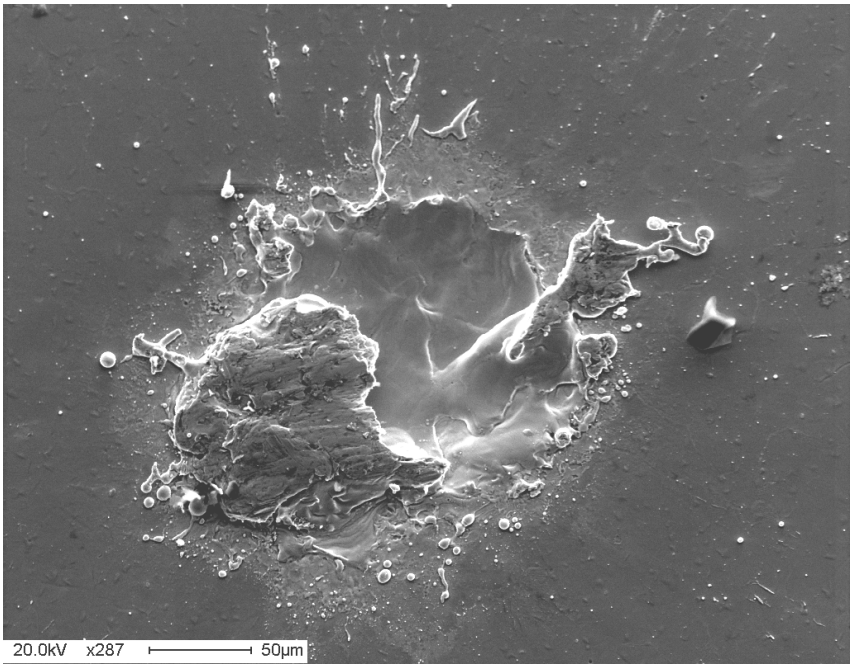

Fig. 4.38 – SEM image of the effect caused by the current exceeding the maximum withstood voltage

The high value reported confirm the goodness of the buffer layer from the electrical properties point of view, particularly suitable for the AC application.

Compositional properties have been analyzed at IMEM-CNR laboratories confirmed the higher ability of good stoichiometric transfer from the ablated target to the substrate. Measures are averaged over several sampling along the same specimen and confirmed the goodness of the PED choice to substitute e-beam evaporation technique for doped-Ceria. Thanks to the out of equilibrium operative way due to the high energy impact, the ablation

of the materials results relatively independent from the melting point of the compounds in the target (section 2.2.2).

Composition	**Film** Ce/dopant at.%	**Target** Ce/dopant at.%
CeO_2 (Yb 45%)	54 : 46	56 : 44
CeO_2 (Zr 10%)	92 : 08	89 : 11
CeO_2 (Zr 15%)	87 : 13	83 : 17
CeO_2 (Ta 10%)	88 : 12	87 : 14
CeO_2 (Ta 20%)	78 : 22	75 : 25

Tab. 4.5 – Summary of compositional analysis performed on films and targets used in PED process

In **tab. 4.5**, one can notice the optimal stoichiometric in PED growth. Actually, a little effect of the different melting point can be seen for Ta-doped samples. The other samples (Yb and Zr-doped) show a composition in the film very similar to that calculated during target preparation (in first column). The column of measures made on the target (the third) shows the elementary ratio obtained after several deposition. Also in this case, an optimal stoichiometric-maintenance behaviour is confirmed for Yb and Zr-doped specimens, while a higher deviation has been detected for Ta doped targets. This result indicates that Ta might be not so suitable as Yb or Zr for long-time deposition in view of long-length CC industrial production.

4.10.4 Mechanical properties of doped-CeO_2

Recently, some interesting results about mechanical properties of PED-grown doped-Ceria layer have been found at DIOPMA centre, a spin-off company of the Barcelona University. A particular apparatus for nanoindentation has been used on our samples and its effect are shown in **fig 4.40**. Nanoindentation is a functional and fast method, providing information about the mechanical properties of different materials at nanometric scale. Different loads has been applied from 0,5 to 0,9 mN to evaluate the plastic deformation within the layer thickness avoiding the contribution of mechanical properties of the substrate.

Two samples have been analyzed: Zr and Ta-doped Ceria. Also for this case, the addition of Ta to CeO_2 does not contribute to remarkable improvement to mechanical properties.

Indeed, this sample shows a high density of cracks near the indented zone, revealing the poor elastic feature of the film. On the other hand, Zr-doped sample owns higher elastic characteristic, despite his ceramic nature, confirming the remarkable improvement due to Zr ions substituting Ce in the crystal structure. Furthermore this layers does not present any crack or fracture within the indentation region.

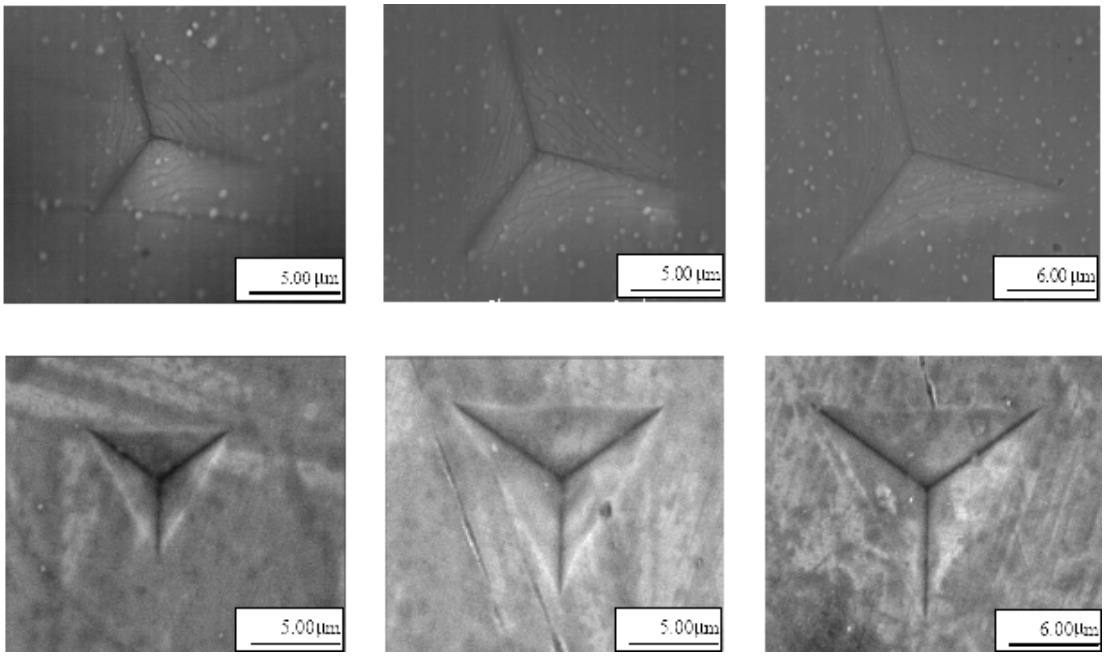

Fig. 4.40 – Ta (1st line of images) and Zr-doped (2nd line) samples examined with SEM after different nanoindentation loads effect

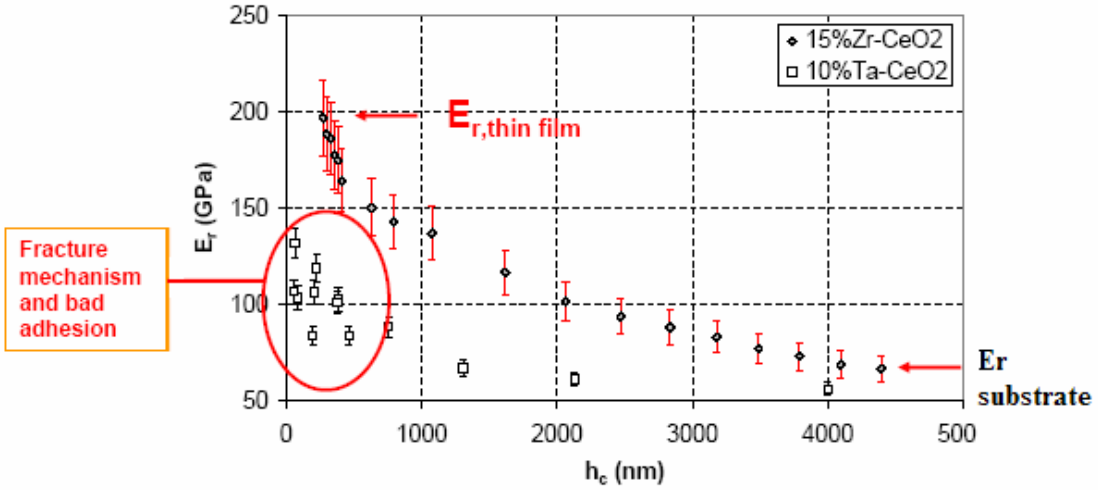

Fig. 4.41 – Ta and Zr-doped CeO_2 nanoindentation test results

In **fig.4.41** the graph of Young's Modulus (Er) vs. penetration depth (hc) is shown. By applying theoretical model, it is possible to extrapolate the Young's modulus for the film that resulted in the range of 235-250 GPa for Zr-doped film and between 136-152 GPa for the Ta-doped[37].

4.10.5 The final test: properties of YBCO grown on the single buffer

For a number of problems occurred at the EDISON S.p.A. R&D laboratories it has not been possible to test all the samples obtained by PED and very few YBCO depositions have been made onto PED-grown single buffer layer. A few samples have been used to adjust YBCO composition and hence, only one XRD pattern (**fig. 4.42**) and a resistance measure (**fig. 4.43**) will be presented for Thermal Co-Evaporation -YBCO deposition.

Other samples have been sent to ENEA laboratories in Frascati (RM) to grow YBCO by PLD, in order to test the goodness of the PED-single buffer layer coupled with different growth-techniques. This is one of the most important group in HTS-CC development in Italy. Besides the YBCO deposition by PLD, they are particularly specialized in advance substrate preparation by using Ni-based alloy with Pd, Co and Cu.

XRD pattern and conductive measures of YBCO deposited by PLD onto a single buffer layer based on Yb-doped CeO_2 grown by PED are reported in **fig. 4.44 and 4.45**

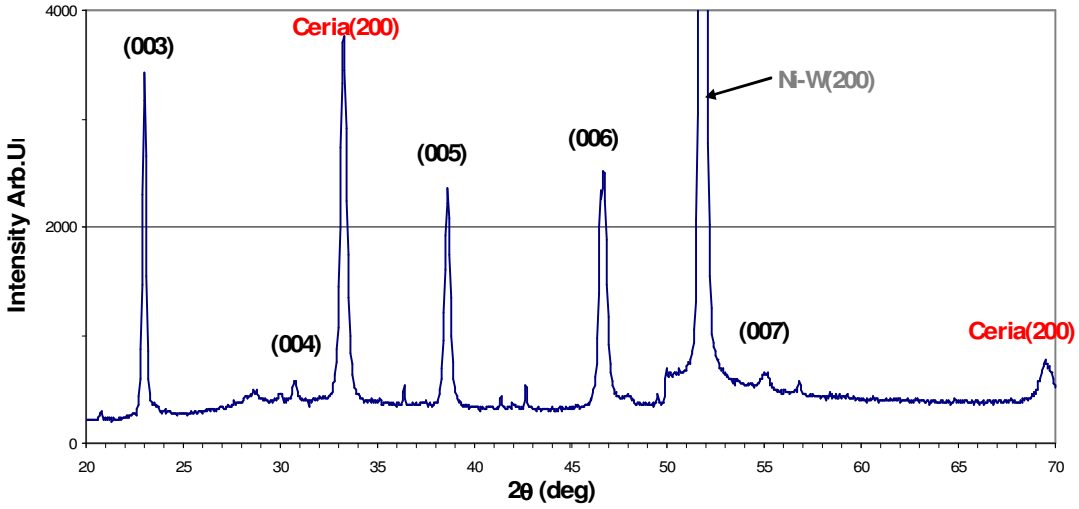

Fig. 4.42 – XRD pattern of YBCO/$Ce_{0,55}Yb_{0,45}O_2$/NiW short sample

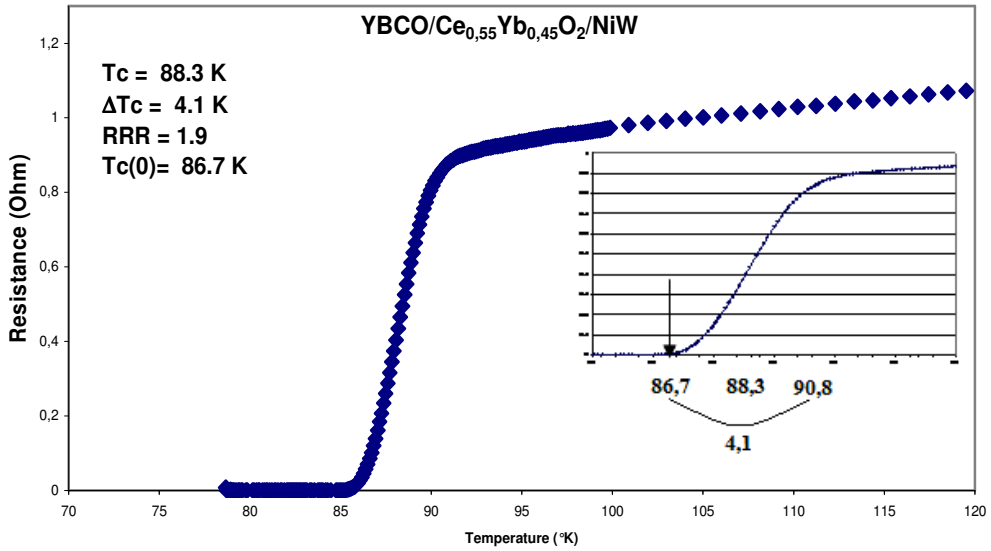

Fig. 4.43 – Four probes R-T graph of YBCO/$Ce_{0,55}Yb_{0,45}O_2$/NiW short sample

These promising results show a good performance of HTS-CC based on template grown by PED system but further improvement can be reached testing other deposition technique to realize long-length and low-cost HTS-CC.

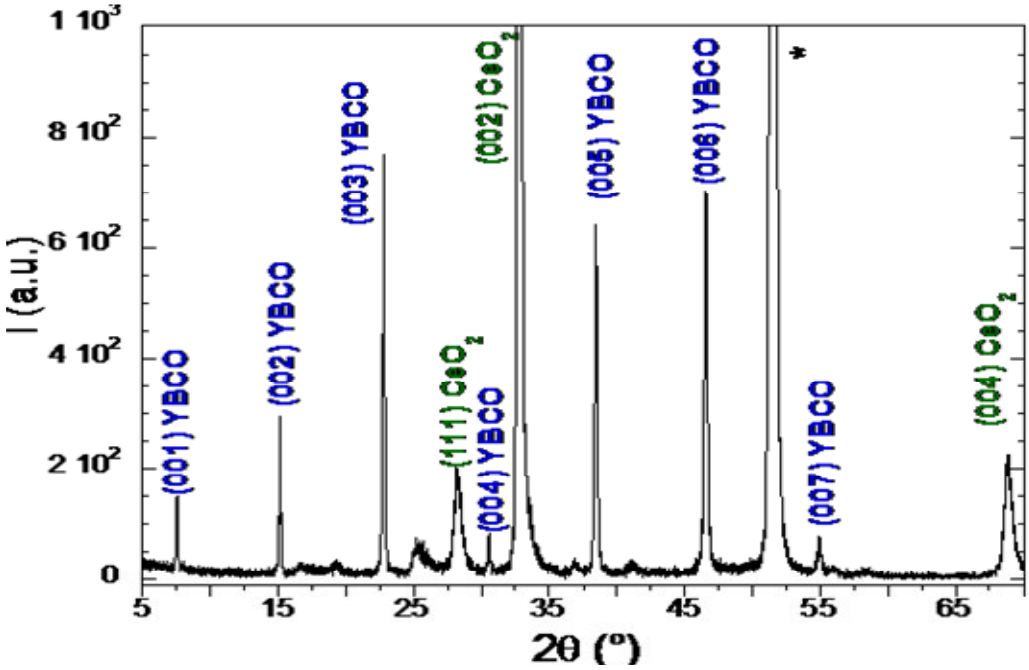

Fig. 4.44 – XRD pattern of (PLD)YBCO/$Ce_{0,55}Yb_{0,45}O_2$/NiW short sample

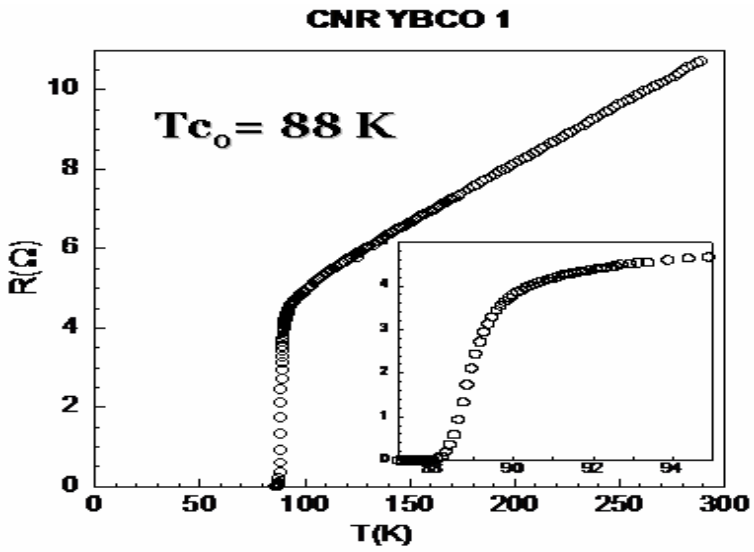

Fig. 4.45 – Conductive measures on (PLD)YBCO/$Ce_{0,55}Yb_{0,45}O_2$/NiW short sample

Observing the XRD pattern and the value of Tc_0, we can really support our choices in superconducting field: doped-Ceria single buffer layer grown by PED allowed the sequential grow of YBCO superconducting layer with high (00l) orientation degree without any presence of secondary phases, and without any trace of polluting Ni or NiO inside it. Transport properties measured by van der Paw four contacts probe confirm the high quality of YBCO revealing a Tc_0 of 88 K and a ΔT of 1,7 K. In summary, the high performances shown by YBCO grown by PLD at high substrate temperature (850°C) demonstrate that single doped-CeO_2 buffer layer can be considered a suitable template for low cost and long length HTS-CC, by using different deposition techniques. Moreover, high quality YBCO layers grown by PED have been reported[38,39], opening new perspectives about the concrete possibility to produce a complete HTS-CC by PED (patent application MI2007A001531)[40].

In conclusion, HTS Coated Conductors technology found a remarkable improvement by using doped-Ceria as effective single buffer layer to reach high cost-effective solution for long length production tapes. Secondly, but not less important, the developing of PED system for doped-Ceria layer showed the great potential of this technique applied to CC and generally in oxide deposition allowing the realization of robust, thick layer characterized by high effective-barrier ability. Further proves will be carried on to obtain an all-PED CC depositing also the HTS layer with this technique.

References

[1] C. Cantoni, D. K. Christen, R. Feenstra, A. Goyal, G. W. Ownby, D. M. Zehner, and D. P. Norton: "Reflection high-energy electron diffraction studies of epitaxial oxide seed-layer growth on rolling-assisted biaxially textured substrate Ni(001): The role of surface structure and chemistry", *Appl. Phys. Lett*. (2001) **79**

[2] B. Kad and A. Goyal: "Report n°9 for the Metals Information Analysis Centre" (1996)

[3] J. R. Thompson, A. Goyal, D. K. Christen, D. M. Kroeger: "Ni–Cr textured substrates with reduced ferromagnetism for coated conductor applications", *Physica C: Superconductivity* (2002) **370**

[4] A. Goyal: "Second generation HTS-conductors", Kluwer Academic Publishers (2005)

[5] A. Goyal, US Patent 6375768, April 23

[6] A, Goyal, US Patent 6106614, August 22

[7] H. C. Freyhardt: "Panorama of the CC development in Europe", Plenary sessions, WAMS, Geneve, 2004

[8] J. Yang, D. Shi, X. Wang, A. Lui and G. Yuan: "Epitaxial YSZ/CeO. and YBCO on cube textured nickel" *Physica C* (2000) **337**

[9] Y. Iijima, M. Hosaka, N. Tanabe, N. Sadakata, T. Saitoh, O. Kohno, K. Takeda: "Growth structure of yttria-stabilized-zirconia films during off-normal ion-beam-assisted deposition", *J. Mater. Res.,* (1998) **13**

[10] J. Dzick, J. Wiesmann, J. Hoffmann, K. Heinemann, F. Garcia-Moreno, A. Isaev, H. C. Freyhardt, W. Lechner: "YSZ buffer layers on large technical substrate", *IEEE Transactions on Applied Superconductivity*, (1999) **9**

[11] S. Foltyn, P. Arendt, P. Dowden, R. DePaula, J. Groves, J. Coulter, Q. Jia, M. Maley, D. Peterson: "High-Tc coated conductors-performance of meter-long YBCO/IBAD flexible tapes" *IEEE Trans. Appl. Supercond.*, (1999) **9**

[12] M. O. Aboelfotoh, "Crystal Structure of Evaporated MgO Films on Amorphous and Polycrystalline Substrates," *J. Vac. Sci. Technol.* (1973) **10 [5]**

[13] M. Bauer, R. Semerad, and H. Kinder: "YBCO films on metal substrates with biaxially aligned MgO buffer layers," *IEEE Trans. Appl. Supercond*. (1999) **9**

[14] M. P. Chudzik, R. E. Koritala, Z. P. Luo, D. J. Miller, C. R. Kannewurf, U. Balachandran: "Mechanism and processing dependence of biaxial texture development in

magnesium oxide thin films grown by inclined-substrate deposition", *IEEE Trans. Appl. Supercond.*, (2001) **11**

[15] V. K. Yang, M. Groenert, C. W. Leitz, A. J. Pitera, M. T. Currie, and E. A. Fitzgerald: "Crack formation in GaAs heteroepitaxial films on Si and SiGe virtual substrates" *Journ. Appl. Physics* (2003) **93**

[16] M.Mogensen, N.M.Sammes, G.A.Tompsett: "Physical, chemical and electrochemical properties of pure and doped ceria", *Solid State Ionics* (2000) **129**

[17] S. Zha, C. Xia, G. Meng: "Effect of Gd (Sm) doping on properties of ceria electrolyte for solid oxide fuel cells", *Journal of Power Sources* (2003) **115**

[18] S. Yamazaki, T. Matsui, T. Ohashi and Y. Arita: "Defect structures in doped CeO_2 studied by using XAFS spectrometry", *Solid State Ionics* (2000) **136–137**

[19] C. E. Hori, H. Permana, K. Y. S. Ng, A. Brenner, K. More, K. M. Rahmoeller and D. Belton: "Thermal stability of oxygen storage properties in a mixed CeO_2-ZrO_2 system", *Applied Catalysis B: Environmental*, (1998) **16**

[20] S. J. Hong and A. V. Virkar: "Lattice Parameters and Densities of Rare-Earth Oxide Doped Ceria Electrolytes" *J. Am. Ceram. Soc.* (1995) **78**

[21] R. D. Shannon: "Revised effective ionic radii and systematic studies of interatomic distances in halides and chalcogenides", *Acta Cryst.*, (1976) **A32(5)**

[22] L. Gianni, A. Baldini, M. Bindi, A. Gauzzi, S. Rampino and S. Zannella: "High-Jc coated conductors with a simple buffer layer architecture", *Physica C* (2005) **426**

[23] R. H. Hammond and R. Borman. "Correlation between the in situ growth conditions of YBCO thin films and the thermodynamic stability criteria", *Physica C* (1989) **162**

[24] W. Prusseit and M. Yoshida "YBCO coating developments and applications in Europe", FSST News 85 (2001)

[25] A. Gauzzi, A. Baldini and S. Zannella, patent application no. WO/2005/024088 (2005)

[26] S. Rampino: "Supersonic O_2 Beam Assisted Deposition of Long-Length $YBa_2Cu_3O_7$ Coated Conductors", Ph.D thesis (2006)

[27] L.J. van der Paw: "A Method of Measuring Specific Resistivity and Hell Effects of Discs of Arbitrary Shape", *Phil. Res. Rep*., 13,1 (1958)

[28] Gilioli E., Baldini M., Bindi M., Bissoli F., Pattini F., Rampino S., Ginocchio S., Gauzzi A., Rocca M., Zannella S: "Co-evaporated YBCO/doped-CeO2/Ni-W coated conductors oxygen improved using a supersonic nozzle", *Physica C* (2007) **463-5**

[29] Gauzzi A., Baldini M., Bindi M., Bissoli F., Gilioli E., Ginocchio S., Pattini F., Rampino S., Zannella S: "Progress in Single Buffer Layer Coated Conductors prepared by Thermal Evaporation", *Ieee Transactions On Applied Superconductivity,* (2007) **17**

[30] Gilioli E., Gauzzi A., Bindi M., Rampino S., Pattini F., Bissoli F., Ginocchio S., Baldini M., Zannella S: "Progress in the Continuous Depostition of YBCO Coated Conductors by Thermal Co-Evaporation", *Advances in Science and Technology* (2006) **47**

[31] M. Strikovski and K. S. Harshavardhan: "Parameters that control pulsed electron beam ablation of materials and film deposition processes", *Appl. Phys. Lett.* (2003) **82**

[32] V. Dediu, and F.C. Matacotta: "Oxygen diffusion in epitaxial $GdBa_2Cu_3O_{7-d}$ thin films", *Phys. Rev. B* (1996) **54**

[33] H. Y. Zhai, H. M. Christen, R. Feenstra, F. A. List III, A. Goyal, K. J. Leonard, Y.Xu, D. K. Christen, K. Venkataraman, and V.A. Maroni: "Pulsed Electron Deposition for Coated Conductor Applications", *Mat. Res. Soc. Symp. Proc.* (2004)

[34] Bindi M., Canetti M., Gangini F., Gauzzi A., Gianni L., Gilioli E., RampinoS. and Zannella S: "Multi-chamber deposition system for continuous production of YBCO coated conductors by thermal co-evaporation", *Journal of Physics: Conference Series* (2006) **43**

[35] J. Lin, N. Masaaki, A. Tsukune and M. Yamada: "Ta_2O_5 thin films with exceptionally high dielectric constant", *Applied Physics Letters* (1999) **74**

[36] A. V. Narlikar: "Frontiers in superconducting materials", Springer Berlin Heidelberg (2005)

[37] J. J. Roa, E. Gilioli, F. Bissoli, F. Pattini, S. Rampino, X. Capdevila, M. Segarr,; *Thin Solid Film* (2008) *Submitted*

[38] H.Y. Zhai, H. M. Christen, R. Feenstra, F. A. List III, A. Goyal, K. J. Leonard, Y. Xu, D. K. Christen, K. Venkataraman, and V. A. Maroni "Pulsed Electron Deposition for Coated Conductor Applications", *Materials Research Society Symposia Proceedings,* 2004

[39] J. E. Mathisa, H. M. Christenb "Factors that influence particle formation during pulsed electron deposition of YBCO precursors" *Physica C: Superconductivity* (2007) **459**

[40] Zannella S., Gilioli E., Bindi M., Pattini F., Bissoli F, Rampino S., Baldini M., patent application n° MI2007A001531

Thin films solar cells

Introduction

Recent years have seen rapid growth in the number of installations of photovoltaic (PV) modules onto buildings connected to the electricity grid. This type of demand has been stimulated in part by government programmes, especially Japan and Germany, and by green pricing policies of utilities or electricity service providers like in Switzerland and the USA. The central driving force can be found in the desire of people and companies to obtain their electricity from a clean, non-polluting, renewable source and above all without high costs related to electricity grid purchase. Another solar's great benefit is its high reliability and little maintenance needs becoming ideal in places difficult to access.

For example, on an office building, atria can be covered with glass/glass PV modules, which can be semi-transparent to provide shaded light. On a factory, large roof can be some of the best location for solar modules and also skylights or building walls can be covered partially with PV.

Considering off-grid homes or other remote buildings such as schools, community halls, and clinics can all benefit from electrification with solar energy. This can power TV, video, telephony, refrigeration equipment or medical tools. PV Systems can be used to pump water in remote areas as part of a potable-water supply system. Solar energy could be a great resource for under-developed and developing countries, but production costs must be appreciably reduced and better efficiency must be reached with 2nd and 3rd generation PV cells (**fig. 5.1**).

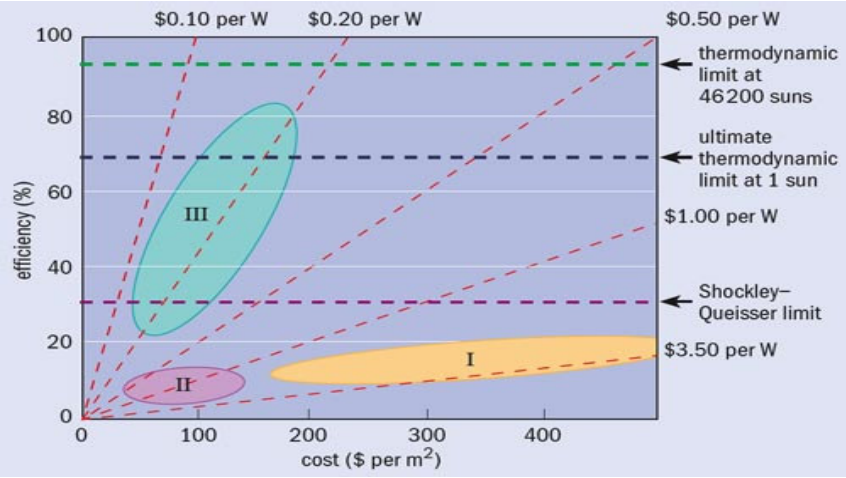

Fig. 5.1 –Cost vs. efficiency graph for the I, II and III generation of photovoltaic solar cells

5.1 Materials for photovoltaic devices

Three key elements in a solar cell form the basis of their manufacturing technology. The first is the semiconductor, which absorbs light and converts it into electron-hole pairs. The second is the semiconductor p-n junction, which separates the photo-generated carriers (electrons and holes) and the third is the contacts on the front and back of the cell that allow the current to flow trough the external circuit (**fig. 5.2**).

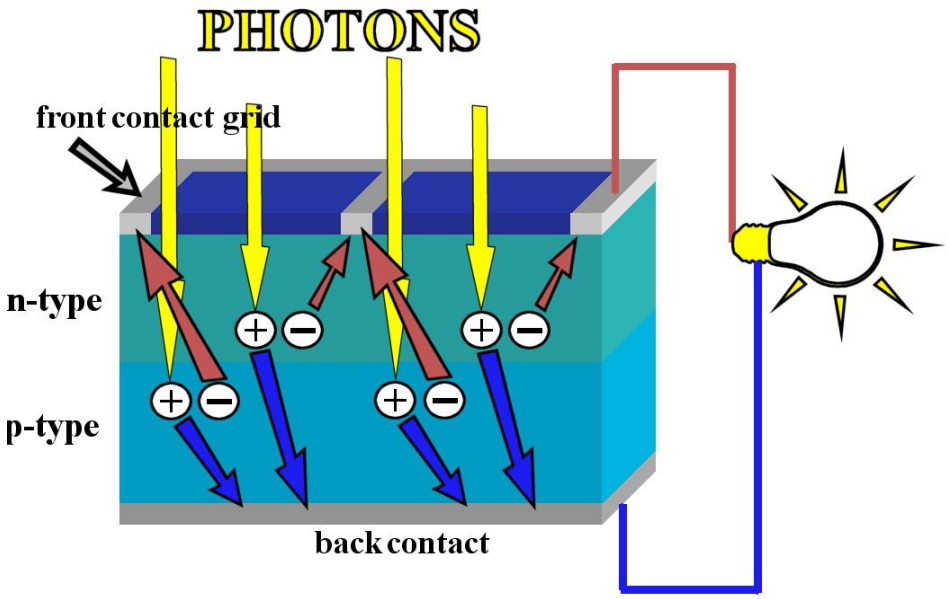

Fig. 5.2 – Electron-hole pair formation by the interaction with photons and consequent charge separation and current flow in external circuit

Every type of cell is characterized by a series of parameter which describe it and allow the comparison among diferent samples (**fig.5.3**):

- *Isc* is the short circuit current (low resistance) obtained by the intersection of current-voltage behaviour with current axis
- *Voc* shows the value of the voltage at opened circuit (high resistance) defined by the intersection of current-voltage function with the voltage axis
- The fill factor (FF) is the ratio of the maximum power point (*Pm*) divided by the open circuit voltage (*Voc*) and the short circuit current (*Isc*):

- The efficiency (η) of a solar cell is the percentage of power converted (from absorbed light to electrical energy) and collected when a solar cell is connected to an electrical circuit. It can be calculated by the formula (Eq. **5.1**):

$$\eta = \frac{Pm}{E \times Ac} \qquad \text{(Eq. 5.1)}$$

Where *Pm* is the maximum power point (in W) obtained by the product of *Isc* and *Voc*, *E* the input light irradiance (in W/m^2) under standard test conditions (STC), that must be defined for every measures, and *Ac* is the surface area of the solar cell (in m^2).

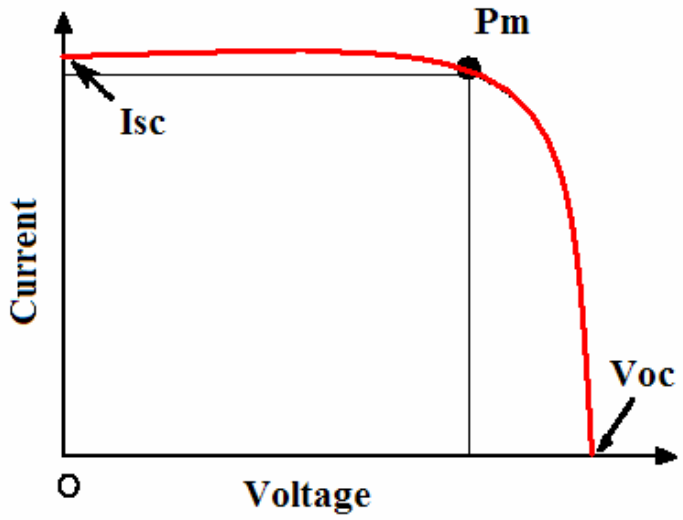

Fig. 5.3 - A typical representation of an I-V curve for a photovoltaic cell

The two main categories of technology are defined by the choice of the semiconductor: either crystalline silicon in a wafer form or thin films of silicon or other materials.

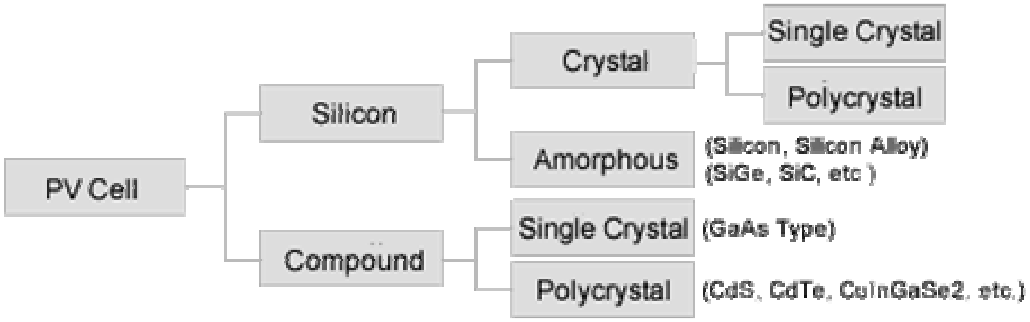

Fig. 5.4 – Schematic representation of solar cell types

Great improvement are made from the first solar cell produced and lots of research group are studying and projecting different and more cost-effective solar cell type. Germany, Japan and U.S.A. are on the cutting edge about technologies and market share of PV.

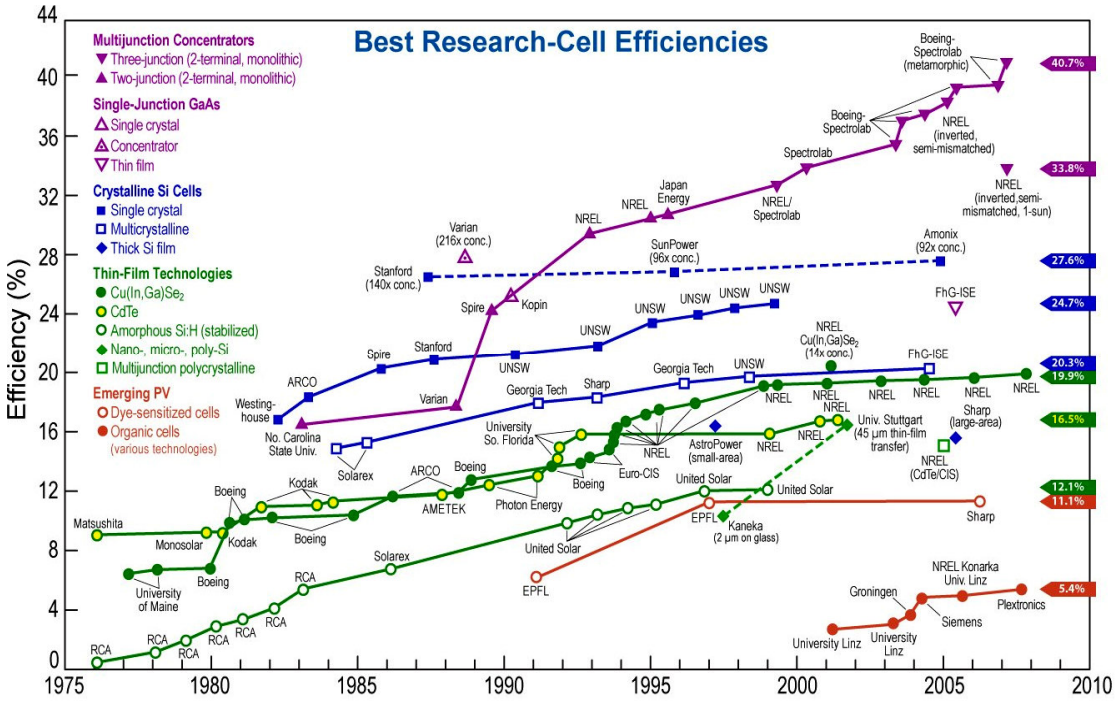

Fig. 5.5 – History of best efficiency solar cell up to first months of 2007 [1]

Lots of effort has driven to higher and higher efficiency of solar cells and just after the publication of the records displayed in the graph above (**fig. 5.5**) a new record of η= 42,8% for three junctions cells under concentrated sun has been reported by a consortium led by the University of Delaware[2] (UD). This surprising results have been achieved by using a novel technology that adds multiple innovations to a very high-performance crystalline silicon solar cell platform. This result demonstrates an important milestone on the path to the 50% efficiency goal set by the Defense Advanced Research Projects Agency (DARPA) in U.S.A. The project, started in November 2005, and DARPA financed the UD-led consortium with approximately $13 million in funding for the Very High Efficiency Solar Cell (VHESC) program to develop affordable and portable solar cell battery chargers for military uses. These recent results put the pieces in place for a solar cell module with a net efficiency 30% greater than any previous devices and twice the efficiency of state-of-the-art silicon solar cell modules.

5.1.1 Silicon solar cells

Historically, crystalline Silicon (c-Si) has been used as the light-absorbing semiconductor in most solar cells, although its low light-absorber ability obliges to grow a considerable thickness (several hundred microns) of material. Nevertheless, it has proved cost-effective because it yields stable solar cells with efficiencies about 11-16% (the theoretical maximum of 33% was calculated by Tiedje in 1984 [3]) and uses process technology developed from the huge knowledge base of the microelectronics industry.

For Silicon-based solar cells, a semiconductor homojunction is formed by diffusing Phosphorus (an n-type dopant) into the top surface of the Boron doped (p-type) Silicon. Screen-printed contacts are applied to the front and rear of the cell, with the front contact pattern specially designed to allow maximum light exposure of the Si material with minimum resistive losses in the cell.

Two types of crystalline silicon are used in the industry. The first is monocrystalline, produced by slicing wafers (up to 150 mm diameter and 350 microns thick) from a high-purity single crystal ingot. The second is multicrystalline silicon, made by sawing a cast block of silicon first into bars and then sliced in wafers. The main trend in crystalline silicon cell manufacture is toward multicrystalline technology, a less expansive and based on a simpler method to obtain lower than c-Si-based but still good efficiency solar cells.

In 1974, researchers began to realize that they could use amorphous silicon in PV devices by properly controlling the conditions under which it is deposited and by carefully modifying its composition. In recent years, amorphous Silicon has taken off and it is common in solar-powered consumer devices that have low power requirements, such as wristwatches and calculators.

Amorphous silicon absorbs solar radiation many times more efficiently than single-crystal silicon, hence a film of about 1 micrometer thick can absorb almost the total of the usable light energy shining on it reaching a maximum efficiency $\eta = 24{,}7\%$. This is one of the main reason for amorphous silicon to reduce the cost of photovoltaics. Other economic advantages are due to a lower temperatures fabrication and the possibility to deposit on low-cost substrates such as plastic, glass, and metal.

The cells are hermetically sealed under toughened and high transmission glass to produce highly reliable and weather resistant modules that may be warranted for up to 25 years[4].

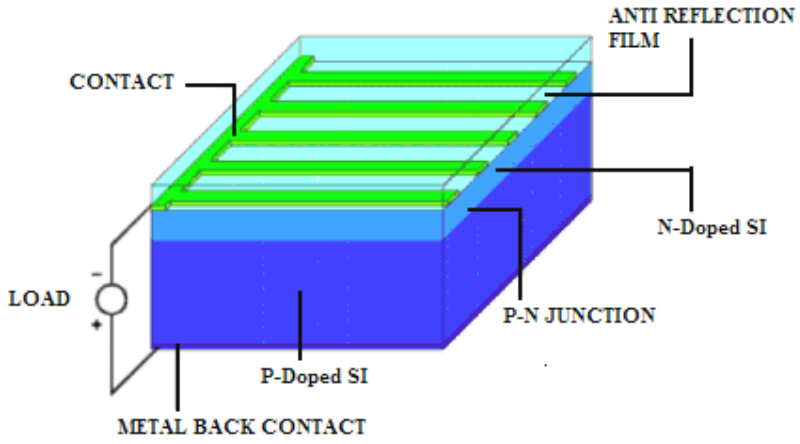

Fig. 5.6 – Silicon solar cell scheme

5.1.2 Gallium arsenide solar cells

Gallium arsenide (GaAs) is a semiconductor compound obtained by the mixture of two elements, Gallium and Arsenic. Gallium is a by-product of the smelting of aluminium and zinc, and it is rarer than gold. Arsenic is not rare, but it is poisonous. Bridging from 50's to 60's, Gallium arsenide was studied for light emitting diode and at the same time was developed for use in solar cells. The principal limit to GaAs terrestrial use is due to the high production cost of single crystals. This cost will be low enough to make GaAs cells competitive, only by assuming that module efficiencies can reach over 25% and the cost of the rest of the system can be reduced.

Nowadays, GaAs appears especially suitable for multi-junction (**fig. 5.7**) and high-efficiency solar cells, for many reasons:

- its bandgap (Eg) reaches the value of 1.43 eV, nearly ideal worth for single-junction solar cells;
- GaAs shows a high absorbance capacity requiring a thickness of only a few microns to absorb sunlight;
- unlike silicon cells, GaAs cells are relatively insensitive to heat and this is the reason for their effective use in concentrator applications
- GaAs is highly resistant to radiation damage. This, in parallel with its high efficiency, makes GaAs desirable for space applications.

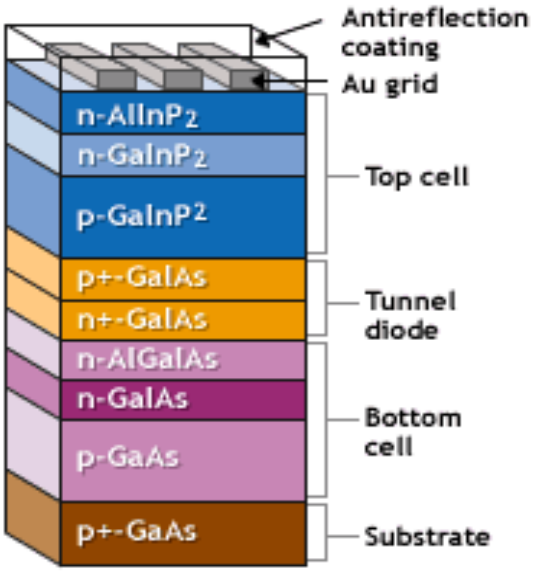

Fig. 5.7 – Multijunction solar cell based on GaAs

One of the greatest advantages of GaAs and its alloys as PV cell materials is that it's open to a wide range of designs. A cell with a GaAs base can have several layers of slightly different compositions leading to a cell designing to accurately control the generation and collection of electrons and holes[5].

Multi-junction topic is worthwhile discussing just a little bit more. The structure, also called “a cascade” or “tandem” cell, can achieve a higher total conversion efficiency by capturing a larger portion of the solar spectrum by the stacking on top of one another based on two or more individual cells with different bandgaps. The individual cells are stacked with a precise order so that sunlight falls first on the material having the largest bandgap. Photons not absorbed in the first cell are transmitted to the second, which then absorbs the higher-energy portion of the remaining solar radiation remaining, at the same time, transparent to the lower-energy photons. These selective absorption processes continue through to the final cell, which has the smallest bandgap (**fig. 5.8**). A multi-junction cell can be made in two different ways. In the mechanical stack approach, two individual solar cells are made independently and then they are mechanically stacked, one on top of the other. In the monolithic approach, one complete solar cell is made first and then the layers for the second cell are grown directly on the first.

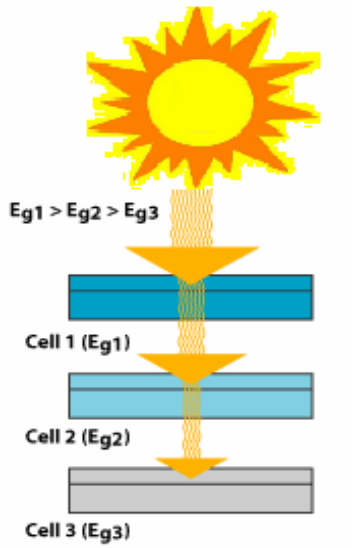

Fig. 5.8 – Multi-junction solar cells schematic operation

5.1.3 Cadmium telluride solar cells

Thin-film cadmium telluride (CdTe) solar cells are the basis of a significant technology with major commercial impact on solar energy production. Large-area monolithic thin-film modules demonstrate long-term stability, competitive performance and the ability to attract production-scale capital investments[6]. CdTe is a II-VI compound semiconductor with a direct optical band gap nearly the optimally matched to the solar spectrum for photovoltaic energy conversion. The direct band gap, Eg = 1,5 eV and the absorption coefficient higher than 5×10^5/cm of CdTe means that high quantum yield can be expected over a wide wavelength range. CdTe emerged as a new electronic material in 1947 and after about ten years it was discovered that simply varying the composition of the two elements one can obtain n-doped or p-doped semiconductor: Cd excess yields n-type while Te excess leads to p-type conductivity[7].

Thin-film CdTe/CdS heterojunction solar cells have been fabricated in two different configurations: substrate and superstrate. In both configurations, light enters the cell through the transparent conducting oxide (TCO) that can be In_2O_3:Sn (ITO), ZnO, SnO_2, and CdS films. In the substrate configuration, the CdTe film is typically deposited first onto a suitable substrate, followed by deposition of CdS and the TCO in backward order. However, this configuration results less efficient, primarily because of poor CdS/CdTe

junction quality and secondly for the poor ohmic CdTe contact realized by the back contact polluted by atoms originated from Cu, one of the most used metal substrate. Therefore, all high-efficiency CdTe solar cells to date, have essentially the same superstrate structure[8].

In the superstrate cell, the TCO, CdS, and CdTe layers are sequentially deposited onto glass, which has the function of mechanical support for the cell. However, light must pass through the supporting glass before reaching the CdS/CdTe junction, so it must be very smooth and highly transparent (**fig. 5.9**).

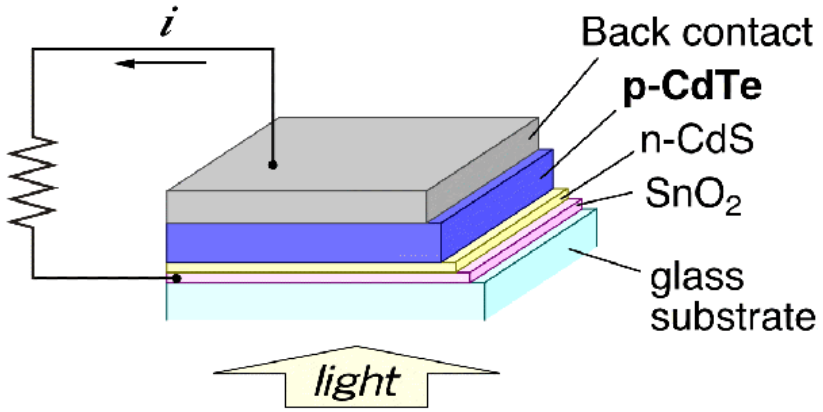

Fig. 5.9 – Superstrate configuration of a thin film CdTe solar cell

The first step in the fabrication of a superstrate CdTe cell is to coat the glass with a transparent conducting oxide (TCO), which allow light transmission and has the function of front contact. To obtain high current density, onto TCO must be deposited a thin layer of CdS as buffer for CdTe. A problem related to this intermediate growth is linked to the poly-crystalline form of the layer that creates more possibility of local shunting or excessive forward current. It has been found that the deposition of a second, highly resistive, transparent oxide layer (ZnO) can remove this hurdle improving junction quality and uniformity. Once grown the absorber layer of CdTe another problem rises: interdiffusion between CdTe and CdS resulting in a shift of the window-layer's bandgap that reduce the light transmission to the absorber. This effect can be minimized either by heat treatment of the CdS with $CdCl_2$ to recrystallize the film or by optimal control of device processing to reduce the CdS thickness. This creates additional environmental and handling problem. Indeed $CdCl_2$ is deposited in a variety of non-vacuum ways, such as dipping the CdTe layer in a $CdCl_2$:CH_3OH or $CdCl_2$:H_2O solution followed by drying to

precipitate a $CdCl_2$ film[9]; by treatment in $CdCl_2$ vapour[10]; by exposure to HCl[11] or Cl_2 gas. The effect of $CdCl_2$ treatment on cell operation is to increase photocurrent, open-circuit voltage and reduced shunting.

Fundamental issues that greatly influence the development of highly efficient CdTe/CdS thin-film solar cells are still present, such as the effective role of doping efficiency in CdTe and the implications of sudden or graded CdTe-CdS junctions.

But the main problem related to the industrial production of this type of thin films solar cells is the necessary use of toxic elements like Cd and chlorinated compounds that generate high environmental impact. This causes increasing cost in planning industrial production for preventing polluting emissions and toxic waste disposal.

5.2 Thin films solar cells based on Copper Indium Gallium Selenide

Copper Indium Selenide ($CuInSe_2$, also called CIS) solar cells have been long considered among the most promising technologies for cost-effective power generation. In particular, thanks to the substitution of Indium with Gallium in the structure, it is possible to obtain a semiconductor with the formula: $Cu(In,Ga)Se_2$ (CIGS). This compound shows very high efficiencies demonstrated both in cells and in modules; indeed this is a remarkable result because the efficiency loss caused by cells assembling in modules is generally too high. Currently, the highest solar cell efficiency is 19,9%, reported by the National Renewable Energy Laboratory (NREL)[12]. Furthermore, several companies have demonstrated large area modules with efficiencies higher than 12% including a confirmed 13,4% efficiency on a 3459 cm^2 module by Showa Shell[13]. Finally, $Cu(In,Ga)Se_2$ solar cells and modules have shown excellent long-term stability[14] in outdoor testing. In addition to its potential advantages for large-area terrestrial applications, $Cu(In,Ga)Se_2$ solar cells showed high radiation resistance, compared to crystalline silicon solar cells[15], and can be very lightweight when grown onto flexible substrates, making them promising for space applications.

High-efficiency CIGS-based solar cells have been fabricated by at least 10 groups around the world. While these groups employ a variety of processing technologies, all the solar cells have the same basic cell structure built around a $Cu(In,Ga)Se_2$/CdS junction in a

substrate configuration with a Mo back contact. This structure utilizes a soda lime glass substrate, coated with a sputtered Mo layer as a back contact. After $Cu(In,Ga)Se_2$ deposition, the junction is formed by chemical bath–deposited CdS with thickness around 50 nm. Then a high-resistance ZnO layer and a doped high-conductivity ZnO layer are deposited, usually by sputtering or chemical vapor deposition. CIGS deposition is the main critical issue of this type of thin films solar cells because it frequently needs a second step of selenization to adjust the stoichiometric composition.

5.2.1 Structural properties

The understanding of CIGS thin films, as used in photovoltaic (PV) devices, is primarily based on studies of its base material, i.e. pure CIS[16]. Moreover, 0,1% of Sodium is often added to CIGS and even though the behaviour of CIS provides a good basis for the understanding of device-quality material, there are pronounced differences when Ga and Na are present in the films[17].

$CuInSe_2$ and $CuGaSe_2$ have the chalcopyrite lattice structure (showed in **fig. 5.10**).

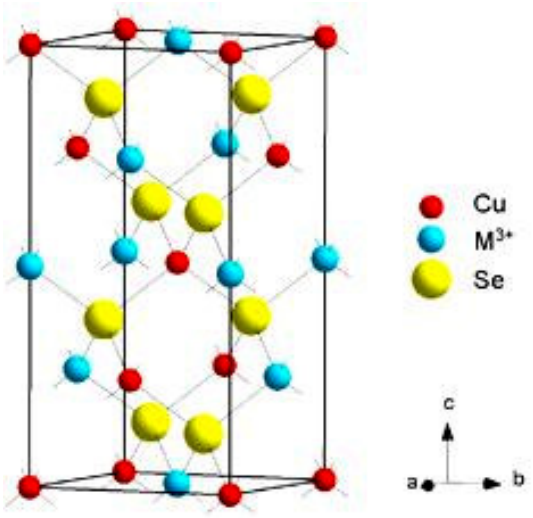

Fig. 5.10 – Chalcopyrite structure of CIS and CIGS compounds

This is a diamond-like structure similar to the sphalerite structure but with an ordered substitution of the group I (Cu) and group III (In or Ga) elements on the group II (Zn) sites of sphalerite. This gives a tetragonal unit cell with a ratio of the lattice parameters **c/a** close

to 2. The deviation from **c/a** = 2 is called the tetragonal distortion and stems from different strengths of the Cu–Se and the In–Se or Ga–Se bonds.

Thin films of Cu–In–Se prepared under an excess supply of Se, that is, normal conditions for thin-film growth of $Cu(In,Ga)Se_2$, have compositions that fall between Cu_2Se and In_2Se_3. Chalcopyrite $CuInSe_2$ is located on this line as well as a number of phases called ordered defect compounds (ODC), because they have a lattice structure described by the chalcopyrite structure with an ordered insertion of intrinsic defects (**fig. 5.11**)[18].

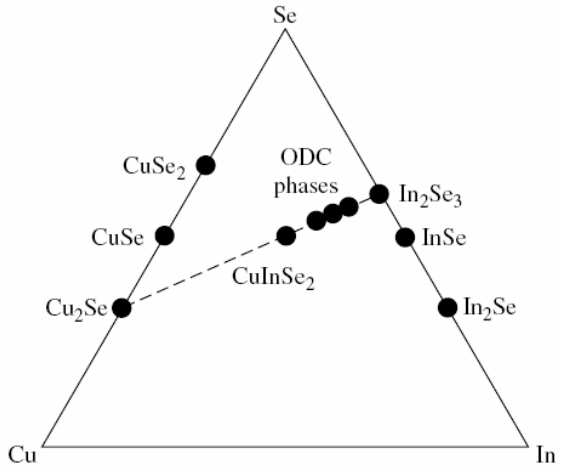

Fig. 5.11 – Ternary phase diagram of Cu-In-Se compounds [18]

The tie-line that link Cu_2Se and In_2Se_3 will be better understood by the pseudo-binary phase diagram that describe it (**fig. 5.11**) where α is the CIS chalcopyrite structure, δ is a high-temperature (HT) phase with the sphalerite structure, and β is an ODC phase. It is interesting to note that the single phase field for CIS at low temperatures is relatively narrow and the Cu percentage is less than the ideal 25%.

At temperatures around 500°C, where thin films are grown, the phase field widens toward the In-rich side. Typical average compositions of device-quality films have 22 to 24 at.% Cu, which fall within the single-phase region at growth temperature. The ability to accommodate large variations in composition without appreciable differences in optoelectronic properties is one of the central characteristics of Cu-In-Se compounds. This is also showed by the mixing of $CuInSe_2$ in any proportion with $CuGaSe_2$, thus forming the alloy $Cu(In,Ga)Se_2$ that is the best high-performance absorber for PV devices when Ga/(In + Ga) ratios is included in the range between 0,2 to 0,3.

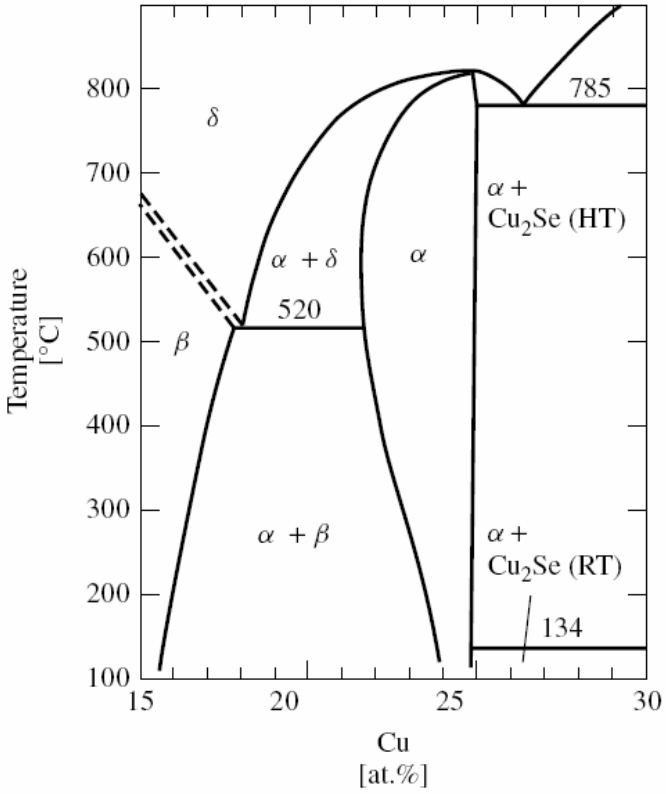

Fig. 5.12 – Pseudobinary In_2Se_3–Cu_2Se equilibrium phase diagram for compositions around the $CuInSe_2$ chalcopyrite phase, α is the CIS chalcopyrite structure, δ is a high-temperature (HT) phase with the sphalerite structure, and β is an ODC phase

This property can be understood from theoretical calculations that show that the defect complex $2V_{Cu} + In_{Cu}$, that is, two Cu vacancies with an In on Cu antisite defect, has very low formation energy[19]. Moreover, the chalcopyrite phase field is increased by the addition of Ga or Na [20]. This can be explained by a reduced tendency to form the ordered defect compounds owing to higher formation energy for Ga_{Cu} (in $CuGaSe_2$) than for In_{Cu} (in $CuInSe_2$). This causes a destabilization of the $2V_{Cu} + In_{Cu}$ defect cluster related to the ODC phases [21]. The effect of Na in the $CuInSe_2$ structure has been calculated by Wei et al.[22], with the result that Na replaces In_{Cu} antisite defects, reducing the density of compensating donors. The calculated effect of Na is therefore consistent with the experimental observations of increased compositional range in which single-phase chalcopyrite exists and increased conductivity.

5.2.2 Optical properties

For a typical direct band-gap semiconductor the absorption coefficient is described by the following equation[23]:

$$\alpha = A(E - Eg)^2 / E \qquad \text{(Eq. 5.2)}$$

From many studies it appeared valid for CIS system too.

The proportionality constant *A* depends on the density of states associated with the photon absorption. From this relation, a band gap value of Eg = 1,02 ± 0,02 eV can be obtained[24].

Ellipsometric measurements of carefully prepared single-crystal samples were carried out and the dielectric functions were obtained together with the complex refractive index for different polarizations. From these measurements a band gap value for CIS of 1,04 eV was determined.

A similar study was also made on bulk polycrystalline ingots of $Cu(In,Ga)Se_2$ having different compositions from x = Ga/(Ga + In) = 0 to 1 and the fundamental transitions for the different compositions were fit to an equation describing the band gap for $CuIn_{1-x}Ga_xSe_2$ as[25]:

$$Eg = 1{,}010 + 0{,}626x - 0{,}167x(1 - x) \qquad \text{(Eq. 5.3)}$$

In this equation, the so-called bowing coefficient is 0,167, but a value of 0,21 was obtained by theoretical calculations as compared to varying from 0,11 to 0,26 determined in several experiments[26]. The optimal Eg value of 1,4 eV has been detected in the range of $0{,}2 < x < 0{,}3$.

5.2.3 Electrical Properties

CIS electrical properties heavily depend from the composition of the material. Indeed, with an excess of Cu, it is always p-type but In-rich films can be made p- or n-type[27]. By annealing in a selenium overpressure, n-type material can be converted to p-type, and conversely, by annealing in a low selenium pressure, p-type material becomes n-type[28]. It is believed that this affects the concentration of Se vacancies, V_{Se}, which act as compensating donors in p-type films. Device-quality $Cu(In,Ga)Se_2$ films, grown with the excess Se available, are p-type with a carrier concentration of about $10^{16}/cm^3$.

Concerning the carriers mobility of CIGS, in several experiments very different values have been collected in a wide range. The highest values of hole mobility have been

obtained for epitaxial films, where 200 cm^2/Vs has been measured for CIGS with about $10^{17}/cm^3$ in hole concentration.

Single crystals have yielded values in the range of 15 to 150 cm2/Vs. Electron mobility determined from single crystals falls in the range from 90 to 900 cm^2/Vs[29].

In addition a large number of intrinsic defects are possible in the chalcopyrite structure and several experiments revealed a great number of electronic transitions. However, it is difficult to assign transitions to specific defects on an experimental basis while theoretical calculations of transition and formation energies provide a basis for the right identification of the different intrinsic active defects in CIGS.

The effect of Ga on the electronic and defect properties is discussed by Wei et al.[21]. In their calculations, acceptor levels did not differ very much between CIS and CIGS, but the donor levels are deeper in the Ga-doped compound. This is consistent with observations of increased p-type conductivity at high Ga-concentrations[25]. At typical device compositions, Ga/(Ga + In) < 0,3, provide the best performance/Ga-content while higher Ga concentration does not contribute to enhance the device efficiency.

A summary of selected properties of CIS are collected in the table below (**tab. 5.1**):

Property	Value
Lattice constant *a*	5,78 Å
Lattice constant *c*	11,62 Å
Melting temperature	986°C
Thermal expansion coefficient long *a*	$8{,}32*10^{-6}$ 1/K
Thermal expansion coefficient long *c*	$7{,}89*10^{-6}$ 1/K
Energy gap	1,02 eV

Tab. 5.1 – Summary of selected properties of CIS semiconductor

5.2.4 Morphology and polycrystalline issues

As it is typical for thin films deposition the grain size and the morphology greatly depend on growth technique and conditions applied.

It has been frequently shown by X-ray photoelectron spectroscopy (XPS) that the free surfaces of CIS films with slightly Cu-poor composition have a composition close to $CuIn_3Se_5$[30]. It merely seems that the composition gradually changes from the bulk to the surface of the films owing to the band bending induced by surface charges[20]. This effect

drives migrating Cu into the bulk leaving the surface depleted of Cu and the depletion is stopped when the composition reaches $CuIn_3Se_5$, since further depletion requires a structural change of the material. It seems to be a typical concentration evolution of the chalcopyrite structures[31]. The band bending as well as the $CuIn_3Se_5$ composition of CIS surfaces disappears when the material is exposed to atmosphere for some time and oxides form on the surface. The surface oxidation is enhanced by the presence of Na[32]. The compounds detected on the surface after oxidation have been identified as In_2O_3, Ga_2O_3, SeO_x, and Na_2CO_3[33]. For this reason it has been common practice to post-treatment CIS or CIGS devices in air usually at 200°C. When devices were fabricated using vacuum-evaporated CdS or (Cd,Zn)S to form the junction, they were annealed for several hours to optimize the device performance[34]. The main effect associated with oxygen is explained as a such passivation of selenium "surface" vacancies on the grains[35]. The V_{Se} at the grain boundaries can act as a recombination centre reducing the effective hole concentration and at the same time preventing the intergrain carrier transport. When oxygen substitutes for the missing selenium, these negative effects are cancelled.

The beneficial effect of the presence of Na on the PV performance of CIGS thin films still lacks a complete explanation. Some researchers proposed that Na assumes a catalytic effect on oxidation enhancing dissociation of molecular oxygen into atomic oxygen which is more effective for the passivation of V_{Se} on grain surfaces. This model is consistent with the observation that Na and O are predominantly found at the grain boundaries rather than in the bulk of the grains in CIS thin films[36].

5.3 Future of CIGS solar cells

Considering the works reported about CIGS and related materials, there has been enormous progress in second generation of solar cells based on this material. It has been evidenced by the high module and cell efficiencies fabricated by several groups, the growth mechanism and characterization studies reported in a great number of publications and the improved engineering knowledge and processes of these materials. There is good reason to be optimistic that cell efficiencies greater than 20% will be achieved in brief and performances and yield will continue to improve. Still, there is a lack of understanding

related to the critical problems associated with semiconductor processing. It is necessary to devote time and research focus at both the laboratory scale, to address fundamental issues, and on the pilot line, to address equipment and scale-up problems to validate processes for a major industrial production. Unfortunately, after more than 25 years of research and development of CIS, manufacturing has only recently started a manufacturing production of efficient PV modules. Thus, developing of more effective deposition technique and more reliable diagnostic and process control is a necessary pass in the direction of this goal.

Basic research cannot be overlooked because many challenges must be faced, such as the understanding of the role of Sodium and the nature of the grain boundaries or free surface; a better comprehension of the role of the CdS layer and the chemical bath process to enable alternative materials that do not contain cadmium and have wider band gap to be utilized with greater efficiency and reproducibility; more efficient TCOs to facilitate the charge carrier extraction in external circuit.

Innovative researches can be explored starting from CIS and CIGS absorber, for example the realization of a tandem cell with an efficiency greater than 25% where CIS alloy system is ideally suited for a new structure since its Eg = 1,0 eV might be an ideal bottom cell, with any of its other alloys characterized by a band gap up to 1,7 eV, for the top cell.

Another improvement can be reached by the use of different substrates that could be polymer-based lighter and more flexible than typical soda-lime glass to improve building integration and window coatings. But the use of these type of substrates is subordinate to low-temperature deposition process which would be useful also for reducing thermally induced stress on the substrate, allowing faster heat-up and cool-down, and decreasing the heat load and stress on the entire deposition system. Similarly, there may be significant cost and processing advantages connected to a cell structure that enables the use of a CIGS layer smaller than 1 μm. When last issues will be solved, the high efficiency, demonstrated stability, and tolerance to material and process variations will give great impulse to thin films PV modules production and it will be one of the major contributor to the solar electric future.

References

[1] Internet Public Library - Carbon Reduction, www.internet-public-library.org/carbon-reduction/painless-carbon-reduction.htm

[2] A.M. Barnett; D.E. Carlson; W.A. Doolittle; C.B. Honsberg; D.A. Kirkpatrick, patent application n°WO/2008/091290

[3] T. Tiedje, E. Yablonovitch, G.D. Cody, B.G. Brooks:" Limiting efficiency of silicon solar cells", *IEEE Trans Electronic devices,* **31** (1984) pp.711-716

[4] U.S. Department of Energy - Energy Efficiency and Renewable Energy, Solar Energy Technologies Program

[5] SANDIA National Laboratory - Photovoltaic Systems Research & Development

[6] A. Luque and S. Hegedus: "Handbook of Photovoltaic Science and Engineering" (2003) WileyBlackwell

[7] F. Kruger, D. de Nobel, *J. Electron*., **1** (1955) 190-202

[8] Bonnet D, Rabenhorst H, *Conf. Rec. 9th IEEE Photovoltaic Specialist Conf*. (1972) pp.129-132

[9] P. Meyers, C. Leng, T. Frey, U.S. Patent 4.710.589 (1987)

[10] B. McCandless, H. Hichri, G. Hanket, R. Birkmire, *Conf. Rec. 25th IEEE Photovoltaic Specialist Conf.*, (1996) pp.781-785

[11] T. Zhou, *Conf. Rec. 1st WCPVSEC,* (1994) pp.103-106

[12] I. Repins, M.A. Contreras, B. Egaas, C. DeHart, J.Scharf, C.L. Perkins, B. To, R, Noufi: "19.9%-efficient ZnO/CdS/CuInGaSe2 solar cell with 81.2% fill factor", *Progress in Photovoltaics: Research and Applications* (2008) **16**

[13] Tanaka, *Proc. 17th Euro. Conf. Photovoltaic Solar Energy Conversion* (2001) pp.989-994

[14] R. Wieting, *AIP Conf. Proc.* (1999) **462**, pp.3-8

[15] A. Jaseneka, U. Raua, K. Weinerta, I. M. Kötschaua, G. Hannaa, G. Voorwindenb, M. Powallab, H. W. Schocka and J. H. Wernera: "Radiation resistance of Cu(In,Ga)Se_2 solar cells under 1-MeV electron irradiation", *Thin Solid Films* (2001) **387**, pp.228-230

[16] L. Kazmerski, S. Wagner: "Cu-Ternary Chalcopyrite Solar Cells", in T. Coutts, J.Meakin: "Current Topics in Photovoltaics" (1985) Academic Press, London

[17] A. Rockett, M. Bodegard, K. Granath, L. Stolt: "Na incorporation and diffusion in$CuIn_{1-x}Ga_xSe_2$", *Photovoltaic Specialists Conference, 1996., Conference Record of the Twenty Fifth IEEE* (1996)

[18] Godecke T, Haalboom T, Ernst F: "Phase Equilibria of Cu–In–Se", *Z. Metallkd.* (2000) **91**

[19] S. Zhang, S. Wei, A. Zunger: "Stabilization of Ternary Compounds via Ordered Arrays of Defect Pairs", *Phys. Rev. Lett.* (1997) **78**

[20] R. Herberholz, U. Rau, H.W. Shock, T. Haalboom, T. Gödecke, F. Ernst,C. Beilharz, K.W. Benz, D. Cahen: "Phase segregation, Cu migration and junction formation in $Cu(In, Ga)Se_2$" *Eur. Phys. Journal AP* (1999) **6**

[21] S.Wei, S. Zhang, A. Zunger: "Effects of Ga addition to $CuInSe_2$ on its electronic, structural and defect properties", *Appl. Phys. Lett.* (1998) **72**

[22] S.Wei, S. Zhang, A. Zunger: "Effects of Na on the electrical and structural properties of $CuInSe_2$", *J. Appl. Phys.* (1999) **85**

[23] H. Neumann: "Optical properties and electronic band structure of $CuInSe_2$", Sol. Cells (1986) **16**

[24] M. I. Alonso, K. Wakita, J. Pascual, M. Garriga, and N. Yamamoto: "Optical functions and electronic structure of $CuInSe_2$, $CuGaSe_2$, $CuInS_2$, and $CuGaS_2$", *Phys. Rev. B* (2001) **63**

[25] M.I. Alonso, M. Garriga, C.A. Durante Rincón, E. Hernández and M. León: "Optical functions of chalcopyrite $CuGa_xIn_{1-x}Se_2$ alloys", *Applied Physics A: Materials Science & Processing,* (2002) **74**

[26] S. Wei and A. Zunger: "Calculated natural band offsets of all II–VI and III–V semiconductors: Chemical trends and the role of cation d orbitals", *Appl. Phys. Lett.* (1998) **72**

[27] R. Noufi, R. Axton, C. Herrington and S. K. Deb: "Electronic properties versus composition of thin films of $CuInSe_2$", *Appl. Phys. Lett.* (1984) **45**

[28] H. Neumann, R. Tomlinson, *Sol. Cells* (1990) **28**

[29] D. J. Schroeder and A. A. Rockett: "Electronic effects of sodium in epitaxial $CuIn_{1-x}Ga_xSe_2$", *J. Appl. Phys.* (1997) **82**

[30] D. Schmid, M. Ruckh, F. Grunwald, and H. W. Shock: "Chalcopyrite/defect chalcopyrite heterojunctions on the basis of $CuInSe_2$", *J. Appl. Phys.* (1993) **73**

[31] K. Gartsman, L. Chernyak, V. Lyahovitskaya, D. Cahen, V. Didik, V. Kozlovsky, R. Malkovich, E. Skoryatina, and V. Usacheva: "Direct evidence for diffusion and electromigration of Cu in $CuInSe_2$" (1997) **82**

[32] M. Ruckh *et al*., *Sol. Energy Mater. Sol. Cells* (1996) **41/42**

[33] A. Kilner: "The Chemical Bath Deposited CdS/Cu(In,Ga)Se_2 Interface as Revealed by X-Ray Photoelectron Spectroscopy", *J. of the Electrochemical Society* (1999) **146**

[34] S. Damaskinos, J. Meakin, J. Phillips, *Proc. 19th IEEE Photovoltaic Specialist Conf.*, (1987)

[35] D. Cahen and R. Noufi: "Defect chemical explanation for the effect of air anneal on CdS/Cu$InSe_2$ solar cell performance", *Appl. Phys. Lett.* (1989) **54**

[36] D. Niles, M. Al-Jassim, K. Ramanathan: "Direct observation of Na and O impurities at grain surface of $CuInSe_2$ thin films", *J. Vac. Sci. Technol., A* (1999) **17**

Transparent Conductive Oxide (TCO) for thin film solar cells

Introduction

Transparent Conductors (TCs), oxides as well as non-oxides, play an important role for energy generation and for energy saving. A basic reason why TCs are of concern is that they can show transparency in a limited range, normally encompassing visible light in the $0,4 \leq \lambda \leq 0,7$ μm wavelength interval. In the infrared (IR) zone their metallic property are able to highly reflect the radiation and in the ultraviolet (UV) range, they become absorbing due to excitations across the energy gap. If the reflectance is in the range of thermal radiation, i.e., $3 \leq \lambda \leq 50$ μm at ambient temperature, the emission of heat is impeded. If reflectance prevails at $0,7 \leq \lambda \leq 3$ μm, covering the IR part of the solar spectrum which carries about 50% of the solar energy, one can combine visible transmittance with rejection of a large part of the solar energy having low thermal emittance. It is then obvious that TCs have a number of diverse applications in the fields of solar energy utilization and energy efficiency. Other applications of TCs emerge from their high electrical conductivity, which enables their use as current collectors in solar cells[1].

6.1 Material for Transparent Conductors

6.1.1 Metal-based thin films

Very thin noble metals films have been used as TCs and transparent heat reflectors at least since the early 1950s[2,3]. They provide a good starting point for solar cells development. In principle, a very thin layer of Cu, Ag, or Au, Pt and Al[4,5] is the simplest way to accomplish a TC and transparent IR reflector. Alternative materials are nitrides, such as TiN and ZrN[6,7], that are notable for their hardness and durability.

Some issues related to these materials are due to the growth mechanism that they exhibit. When the above mentioned metals are deposited onto glass or some other dielectric material, the film goes through a series of rather well defined ‘‘growth stages’’ [8,9]. Initially, tiny metallic nuclei are formed at certain sites on the substrate. Continued deposition makes the nuclei grow via surface diffusion and direct impingement until the formation of high columns. Finally, the columns irregularly expand and then coalesce forming the concrete film layer[10].

This growth mechanism creates several issues to the optical properties of the TC limiting the radiation transmittance because of the high number of scattering events which deviate the incident radiation. To obtain a reasonably uniform surface is often needed a film relatively thick (depending on the deposition technique adopted) having, therefore, a high absorbance factor.

But it is possible to boost the transmittance by adding antireflection layers. One can grow dielectric/metal and dielectric/metal/dielectric multi-layers using dielectrics with high refractive indices, such as Bi_2O_3, In_2O_3, SnO_2, TiO_2, ZnO, and ZnS that give the largest enhancement. Some of these products use more than two or three-layers including as many as seven layers, with two metal films. It is remarkable that these TCs are prepared with a careful thickness control (close to atomic precision) in a high-performance production environment handling glass sheets up to $30m^2$ in size. In spite of excellent results reached by these multi-layer both in optical and electrical properties (sheet resistance $R_s = \rho/t = 3$ Ohm), thick-control difficulties, high cost and long time deposition must be considered and new solution are under study in oxide field.

6.1.2 Transparent Conductive Oxide (TCO)

Metal oxide thin films have been used as TCs and transparent heat reflectors since the beginning of the 1900s[11]. The most widely used and studied n-type TCOs are based on Zn, In, and Sn (and sometimes Cd) oxides. Doping is accomplished either by substituting a higher-valent metal, by replacing some oxygen with fluorine or by introducing oxygen vacancies. The fundamental band gap is wide enough to allow very low values of radiation absorbance and doping is necessary to make the materials IR reflecting and electrically conducting. A specific advantage of the TCOs, compared to the noble metal-based counterparts, is the chemical and mechanical stability which allows their use on glass surfaces exposed to the ambience so they are sometimes referred to as ‘‘hard coats’’.

A resistivity of 10^{-4} Ohm*cm is often quoted as a number characterizing optimized films of In_2O_3:Sn (or ITO)[12], In_2O_3:Mo, (IMO), ZnO:Al (AZO), and ZnO:Ga (GZO) and many other compounds. Recent investigations of ITO films have demonstrated resistivities between 7 and $8*10^{-5}$ Ohm*cm and free carrier densities as high as $2{,}5*10^{21}$ cm^{-3} [13].

Particular bi-layers composed by AZO and ZnO showed better conductive and optical properties than the AZO by itself.

Presenting these features, TCOs are becoming an increasingly important element of a variety of thin-film and flat-panel technologies, not only for photovoltaic applications but also for low-emissivity windows, electrochromic windows and flat-panel displays.

Key TCO parameters are summarized in **table 6.1**[14]

Key parameter	Description
Optical Performance	This includes both the transparency in the visible as determined by the band edge, as wellas the infrared transparency as primarily defined by the plasma edge. In addition, it may be desireable to control the reflectivity and refractive index to produce, for example, integrated antireflection coatings.
Electrical conductivity	This is critical, but in many systems, it is desireable to be able to controllably dope the TCO over the full range from conductive to insulating.
Cristallinity	In general high crystallinity is desirable to get the best, but many TCO materials show good properties in the amorphous state. This has some real advantages in terms of process temperatures and, in some cases, interface stability.
Deposition cost and temperature	Clearly, the lower the deposition temperature for the same quality materials, the better in terms of compatibility and cost, for example, the use of ZnO in CIS solar cells primarily allows a low deposition temperatures. This is also true if amorphous materials can be used.
Toxicity of constituents	This is an increasingly important issue, especially with respect to end-of-life considerations. Toxicity is also an issue during the deposition process.
Hardness	Controlling the hardness can be important for applications where mechanical forces may be encountered and if the TCO is the top exposed layer.

Tab. 6.1 – The key TCO parameters that must be considered for the right choice

6.2 ZnO-based transparent conductive oxide

Zinc Oxide (ZnO) has been long studied for a wide area of interesting uses. ZnO is a semiconductor with a direct bandgap energy of about 3,3 eV at room temperature. Thanks to this feature most common applications are in laser diodes and light emitting diodes (LEDs) since it has an exciton and biexciton energies of 60 meV and 15 meV, respectively. Most ZnO has n-type character, even in the absence of intentional doping. Native defects such as oxygen vacancies or zinc interstitials are often assumed to be the origin of this, but the subject is still under discussion[15]. An alternative explanation, based on theoretical calculations, proposes the unintentional substitutional hydrogen responsible for the n-type conductivity[16]. Thin film can be easily n-type doped by introducing aluminium, indium, or excess zinc[17]. P-type doping is difficult and is currently an active area of research, with arsenic as the leading candidate dopant[18]. This could open novel and advantageous perspectives in 2nd generation of solar cells, where one could grow a p-n homo-junction based only on ZnO with different dopants.

Indeed it is a very attractive and common material that can be grown in several forms and phases. It is non-toxic and it show unique optical, semiconducting, piezoelectric, and magnetic properties.

ZnO nanostructures exhibit interesting properties including high catalytic efficiency and strong adsorption ability. Recently, the interest has been focused toward the application of ZnO in biosensing because of its high biocompatibility, and fast electron transfer kinetics. Such features advocate the use of this material as a biomimetic membrane to immobilize and modify biomolecules. But also one-dimensional semiconductor nanowires and nanorods attracted increasing attention due to their physical properties arising from quantum confinement, electronic quantum transport and enhanced radiative recombination of carriers. Nanostructure have promising potentials in extensive applications and are the fundamental for fabricating short-wavelength nanolasers, field-effect transistors, ultrasensitive nanosized gas sensors, nanoresonators, transducers, actuators, nanocantilevers, and field emitters[19].

6.2.1 Structural properties of ZnO

ZnO is polimophic compound that can assume different crystalline structure depending on external conditions. At ambient temperature and pressure, the thermodynamically stable phase is wurtzite. The zinc-blende (i.e. the cubic analog of wurtzite) ZnO structure can be stabilized only by growth on cubic substrates and the rocksalt (NaCl) structure may be obtained applying a relatively high pressure.

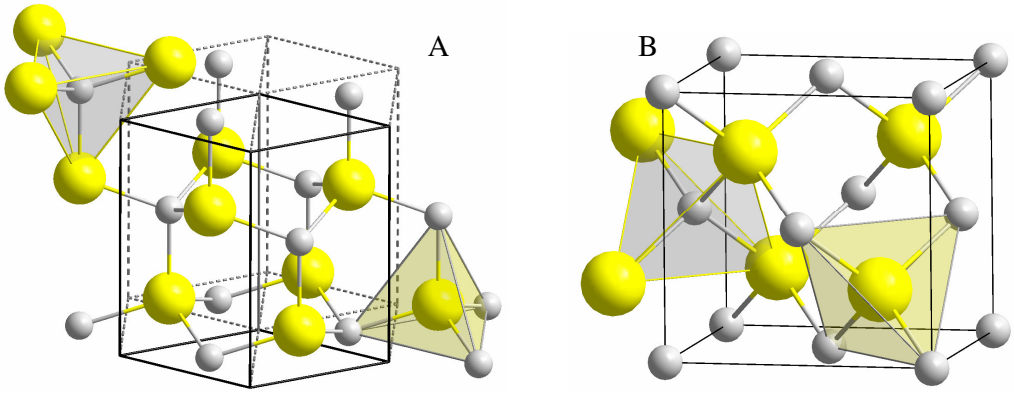

Fig. 6.1 – Wurtzite (A) and zinc-blende (B) are the most useful structure assumed by ZnO

The wurtzite structure has a hexagonal unit cell with two lattice parameters, **a** and **c**, in the ratio of **c/a** = 8/3 = 1,633 and belongs to the space group of P63mc. The structure is composed of two interpenetrating hexagonal-close-packed (hcp) sublattices, each of which consists of one type of atom displaced with respect to each other along **c**-axis. Each sublattice includes four atoms per unit cell and every atom of this type is surrounded by four atoms of the other kind and are coordinated at the edges of a tetrahedron[20].

Like other II-VI semiconductors, wurtzite-phase of ZnO can be transformed to the rocksalt structure applying an external hydrostatic pressures (at about 10 GPa). This is due to the reduction of the lattice dimensions causing higher interionic Coulomb interaction (typical of ionic compounds). The space-group symmetry of the rocksalt-type structure is Fm3m, and the structure is sixfold coordinated. However, the rocksalt structure cannot be stabilized by the epitaxial growth, as in the case of zinc-blende structure. This is a metastable form and can be stabilized only by heteroepitaxial growth on cubic substrates, such as ZnS[21] GaAs/ZnS[22]. In the case of highly mismatched substrates, there is usually a certain amount of the zinc-blende phase of ZnO separated by crystallographic defects

from the wurtzite phase. The symmetry of the structure is given by space group $F\bar{4}3m$ and composed of two interpenetrating face-centered-cubic (fcc) sublattices.

6.2.2 Electrical and optical properties

Pure ZnO films exhibit a low intrinsic defect density and optical properties close to bulk material. Undoped ZnO with a wurtzite structure naturally becomes an n-type semiconductor due to the presence of intrinsic or extrinsic defects. They were generally attributed to native defects, such as the Zn interstitial and the O vacancy[15]. However, recently investigations based on density-functional theory suggest that hydrogen in ZnO occurs exclusively in the positive charge state and it is responsible for the n-type conductivity of ZnO[23]. The highest room-temperature electron mobility for a bulk ZnO single crystal grown by vapor-phase transport method is reported to be about 205 cm^2/Vs with a carrier concentration of $6{,}0*10^{16}$ cm^{-3}, but for thin films grown by different methods (RF magnetron sputtering, MBE, MOCVD or PLD) the electron mobility shows lower values (between 100 and 150 cm^2 /V s) while carrier concentration can reach $7*10^{17}$ cm^{-3}. For example, pure ZnO thin films growth by PLD exhibit a wide range of resistivity value depending on the background oxygen partial pressure. As the n-type feature is related also to the oxygen vacancies, ZnO conductivity follows a direct proportional law between the oxygen pressure and the conductivity. The lowest resistivity obtained in these series of PLD-deposition was in the order of 10^{-1} Ohm*cm, after a growth in a lower than 10^{-3} mbar pressure. On the other hand, the resistivity of the ZnO films grown at the same substrate temperature, but at the oxygen pressure about $6{,}5*10^{-2}$ mbar, achieved values greater than 10^5 Ohm*cm.

In order to enhance the conductivity of ZnO, it is necessary the introduction of dopant element to achieve a larger number of carriers in conduction band. Many works present values of resistivity in the range of $1\text{-}5*10^{-4}$ Ohm*cm for PLD-grown ZnO thin films doped with 2 wt% of Al_2O_3[25,26] or different amount of In_2O_3 and Ga. The electrical resistivity in these films resulted much lower than pure ZnO films because of the contribution of trivalent ions in Zn substitution and interstitial positioning as well as the increase of oxygen vacancies.

The optical properties of a semiconductor are connected with both intrinsic and extrinsic effects. Intrinsic optical properties of undoped ZnO reported in lots of works exhibit high values (90%) for average transmittance calculated in the visible range: 5% higher than in the case of commercial ITO. This appears relatively independent from deposition temperature and deposition technique chosen for the film growing. Considering the doping effect, even if the adding of dopant causes an improvement of over 2 order of magnitude in conductivity measurements, it creates a high number of defects in ZnO structure lowering the high typical value of transmittance for pure ZnO.

6.3 Experimental procedure for ZnO and AZO grown by PED

Many different deposition techniques can be used to grow ZnO and AZO thin films. As written in previous paragraph, the best optical and electrical performances have been achieved either by RF Magnetron Sputtering, MBE, MOCVD and PLD. Also PED, has already been tested to ZnO growth by other research group[27].

As described in the case of CeO_2 and doped-CeO_2, the preparation of the target of ZnO and AZO for PED deposition has been performed following the same method used for those compounds. Since the lower melting point of ZnO, compared to CeO_2, the only difference that we have applied was to the maximum sintering temperature which has been fixed to 1000°C instead of 1300°C. Moreover, in the powder-mixing step, a little amount of isopropanol has been added to amalgamate the compounds and force a more compact pellets during the ambient-temperature uniaxial pressing.

During the deposition process, after the substrate loading in the deposition chamber, the pressure is pumped down to a base value of about $9*10^{-6}$ mbar, then the chamber is filled with O_2 gas to achieve the desired background pressure while the temperature increases up to the desired value (from RT to 700 °C). Before the deposition, keeping the quartz protected by the shutter, the target is pre-ablated at accelerating voltage from 8 kV to 17,2 kV (the optimal value for ZnO deposition) in about 10 minutes in order to stabilize the pulsed e-beam and to uniformly clean the surface. At the end of the process, the shutter is closed, the substrate is cooled to room temperature and the chamber pressure drops back to the base value.

6.4 Characterization techniques

For TCO materials, besides the characterization techniques presented in section 4.7, other methods are necessary to investigate the particular features: UV-VIS and IR transmittance, electrical properties of the film and the surface roughness. In view of successive deposition ("superstrate" configuration, paragraph 5.1.3), low roughness values are needed while higher are desirable to reach a high antireflecting power (in "substrate" configuration, paragraph 5.1.3).

6.4.1 UV-VIS spectroscopy

The instrument used in the ultraviolet-visible (UV-VIS) range measures the intensity of the transmitted light through a sample (I) compared to the intensity of the incident light (I_0). The ratio I / I_0 is the transmittance, usually expressed as a percentage (%T). The absorbance, A, is calculated from the transmittance by the relation:

$$A = -\log(\%T) \qquad \text{(Eq. 6.1)}$$

The basic parts of a spectrophotometer are a light source, a holder for the sample, a diffraction grating or monochromator to separate the different light wavelengths and a detector. The radiation source is often a Tungsten filament (300-2500 nm), a deuterium arc lamp in the ultraviolet region (190-400 nm), and, more recently, light emitting diodes (LED) and Xenon Arc Lamps for the visible wavelengths. The detector is typically a photodiode generally used with a monochromator, which filters in such a way that only the light of a single wavelength can reach the detector.

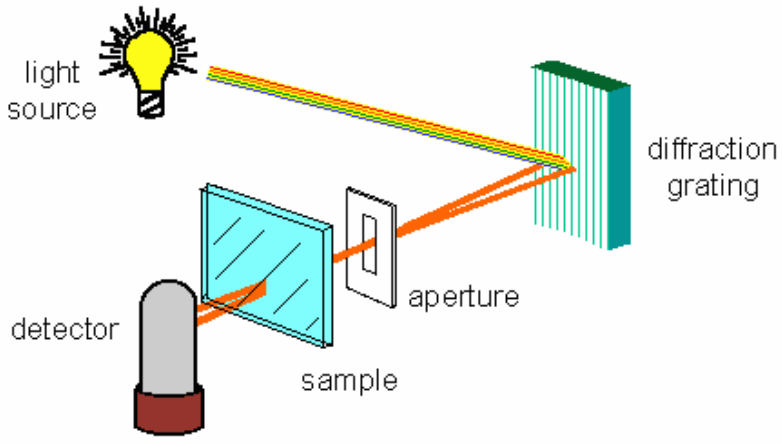

Fig. 6.2 – Scheme of a single beam UV-VIS spectrophotometer

Optical transmission spectra have been measured by a UV-VIS spectrophotometer (JASCO V-530) at IMEM laboratories. All the measures presented have been taken in the 350-1100 nm range and corrected by subtracting the background contribution of the substrate.

6.4.2 Atomic Force Microscopy (AFM)

The AFM instrument consists of a microscale cantilever with a sharp tip (probe) at its end used to scan the specimen surface at nanometric level. The cantilever is typically silicon or silicon nitride with a tip radius of curvature on the order of nanometers. When the tip is brought into proximity of a sample surface, various forces between the tip and the sample lead to a deflection of the cantilever according to Hooke's law:

$$\mathbf{F} = -k\mathbf{x} \qquad \text{(Eq. 6.2)}$$

Depending on the situation, forces that are measured in AFM include mechanical contact force, van der Waals forces, capillary forces, chemical bonding, electrostatic forces, magnetic forces (in Magnetic force microscope (MFM)), Casimir forces, solvation forces etc. As well as force, additional quantities may simultaneously be measured through the use of specialized types of probe using Scanning Thermal Microscopy (STM) or photo thermal microspectroscopy.

Typically, the deflection is measured using a laser spot reflected from the Au- or Al-coated top surface of the cantilever into an array of photodiodes. Other methods include optical interferometry, capacitive sensing or piezoresistive AFM cantilevers.

During the measurements, a feedback mechanism is employed to adjust the tip-to-sample distance to maintain a constant force between the tip and the sample. The tip is mounted on a vertical piezo scanner while the sample is being scanned in X and Y using another piezo block. The resulting map of the scanned area represents the topography of the sample as a function of X and Y coordinates.

The AFM device can operate in a number of modes, depending on the application. In general, possible imaging modes are divided into static (also called contact) and a variety of dynamic (or non-contact) modes where the cantilever is vibrated.

In contact mode, the force between the tip and the surface is kept constant during scanning by maintaining a constant deflection. Close to the surface of the sample,

attractive forces can be quite strong, causing the tip to fall onto the surface. Thus, static mode AFM is always done in contact where the overall force is repulsive and this is the reason for the name.

In the dynamic mode, the cantilever is externally oscillated at, or close to, its fundamental resonance frequency. The oscillation amplitude, phase and resonance frequency are modified by tip-sample interaction forces; these changes in oscillation, with respect to the external reference oscillation, provide information about the sample's characteristics that are collected and imaged. Tapping is the most-known dynamic mode in AFM.

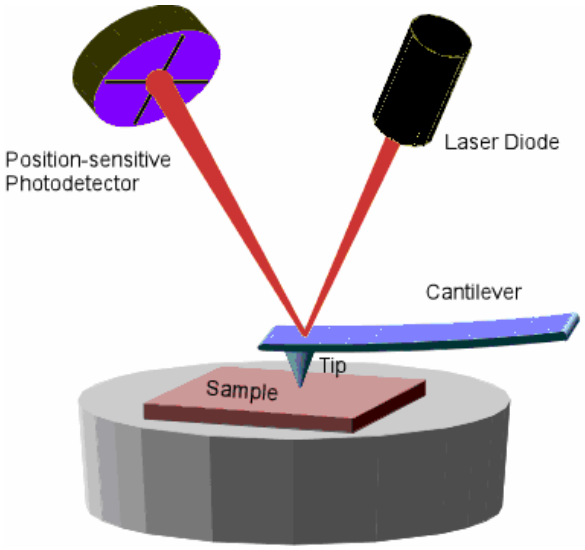

Fig. 6.3 – Schematic image of basic constituents of the AFM instruments

All the presented AFM images have been collected in contact mode by using AFM Digital Instruments NANOSCOPE IIIA located at "Centro Interdipartimentale Misure" of the Parma University.

6.5 Results for ZnO grown by PED

Different series of experiment have been performed to test PED for ZnO and AZO deposition. Starting from pure ZnO, the effect of the substrate temperature and the deposition time have been studied (keeping the background oxygen pressure at $5*10^{-3}$ mbar). In the second step we deposited ZnO doped with 2wt% and 4wt%-Al_2O_3, trying to improve the electrical properties of undoped ZnO films.

We studied the behaviour of electrical properties and optical transmittance as a function of the substrate temperature to test PED system as a reliable and suitable technique for ZnO deposition. The properties of samples grown on 1x1 cm quartz substrates at different temperature are reported in **tab. 6.1.**

Sample	Growth temperature	(200) Orientation degree	Resistivity (Ohm*cm)	Average transmittance (%)
ZnO-1	200°C	0,0%	14	86,7%
ZnO-2	400°C	98,9%	2	95,6%
ZnO-3	500°C	97,7%	0,15	93,0%
ZnO-4	600°C	69,2%	0,3	90,9%
ZnO-5	700°C	39,0%	0,12	97,3%

Tab. 6.1 – Summary of temperature depending features of ZnO thin films deposited on amorphous quartz

As we can extrapolate from the **tab 6.1,** the optimal temperature for depositing (200) oriented ZnO films by PED are included between 400 and 500°C. Outside, it is possible to grow less oriented and even amorphous films by PED.

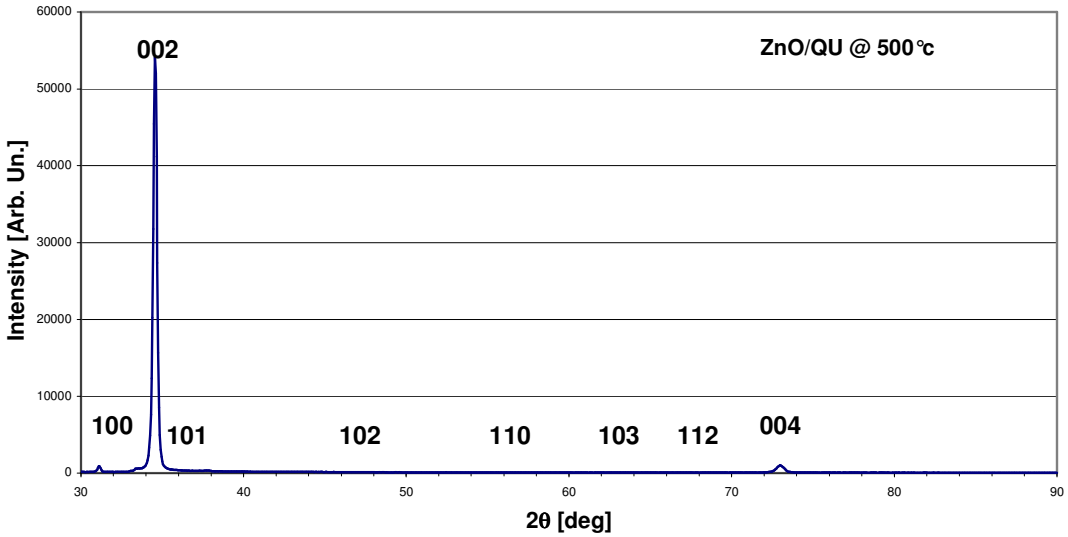

Fig. 6.4 – XRD pattern of the 500°-grown sample showing the high crystalline phase and out-of plane orientation

High orientation degree is important in superstrate-growing configuration of CIGS solar cells to improve its absorption ability.

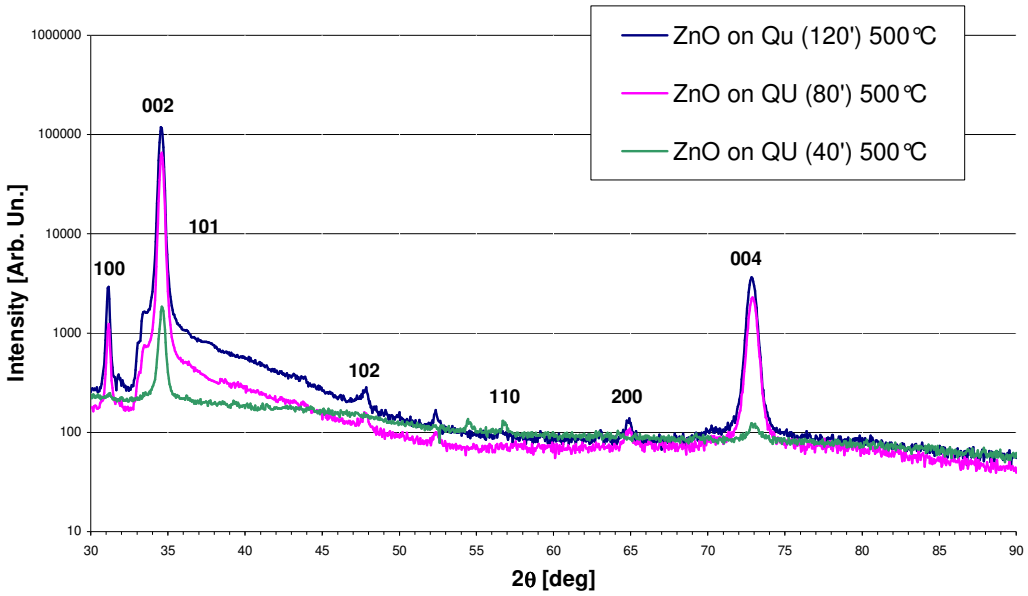

Fig. 6.5 – Comparison among XRD pattern of samples grown at 500°C for different time.
The intensity is evaluated in logarithmic scale to emphasize the smaller peak

Similarly to buffers grown by ISD and IBAD techniques (section 4.3), also in the case of ZnO grown on amorphous quartz, the higher the thickness of the ZnO film, the higher is the out-of-plane orientation (**fig. 6.5**) confirming the step-by-step growth mechanism described in 6.1.1[10].

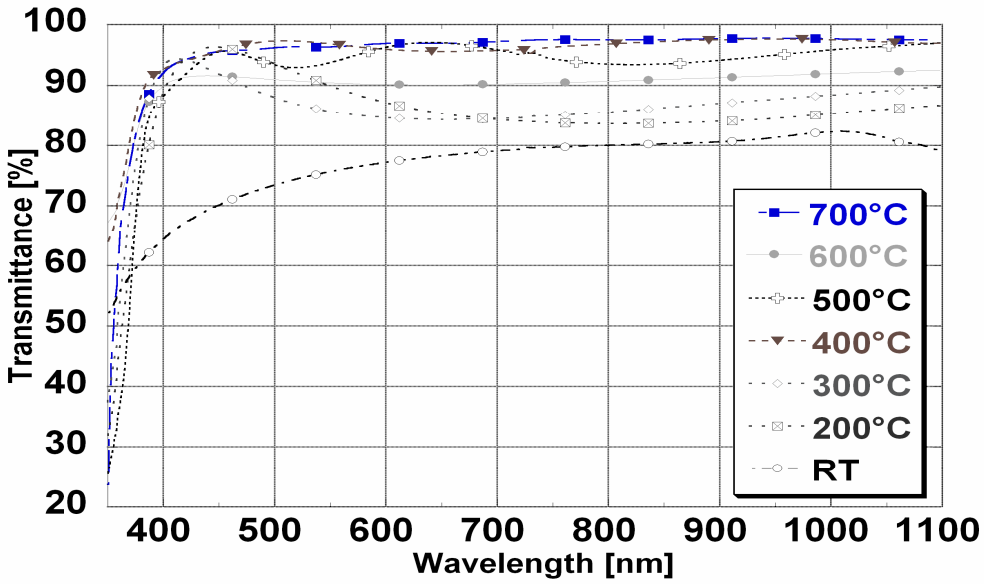

Fig. 6.6 – Transmittance of pure- ZnO films grown at different temperature

In **fig 6.6,** the best optical properties produced during the ZnO deposition series are shown. The presented results have been calculated by subtracting the substrate contribution and normalizing the film thickness to the standard value of 100 nm. Then, a further campaign of deposition has been performed to consider the effect of the thickness on the film transmittance (**fig. 6.7**).

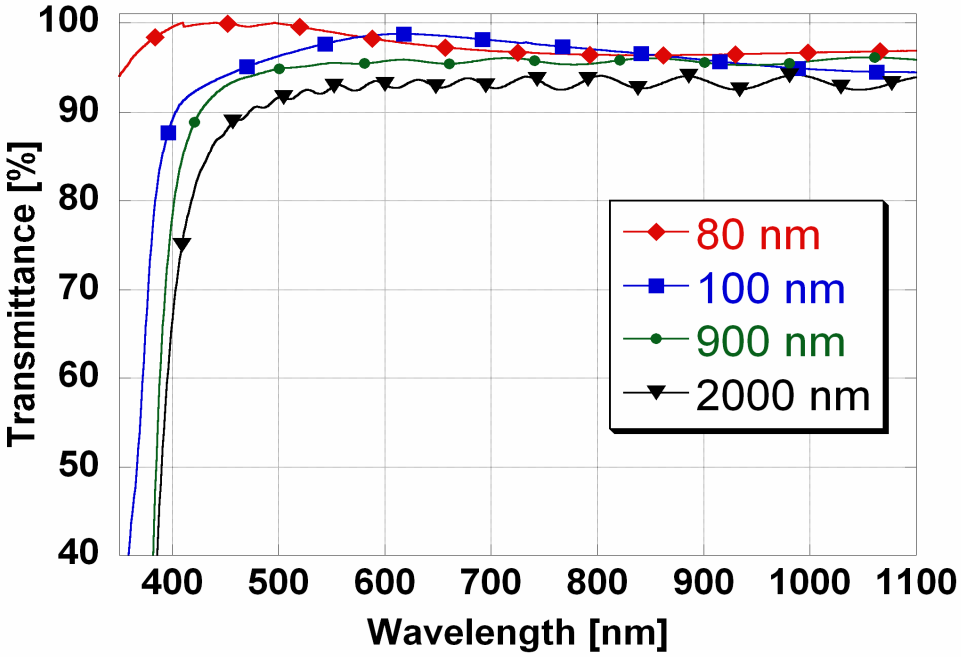

Fig 6.7 – Optical transmittance of samples with different thickness grown at the same temperature and pressure condition

We observed above 90% transmittance value for all the films with thickness up to 2 µm. In this graph (**fig. 6.7**), the oscillations of the transmittance value evidently appear for the thicker film. They are due to the interference fringes caused by constructive and destructive interferences between the film and the substrates presenting a different refractive index. The optical effect has been noticed also for doped-Ceria deposition (section 4.9.1) where, from the colours of the film, we approximately calculated the film thickness.

Standard four probe system has been used to measure the electrical properties; although we obtained good results for pure ZnO (**tab. 6.1**), in order to improve them in view of a

concrete application as TCO in CIGS solar cells, it is necessary to introduce trivalent-dopant to enhance n-type carriers density.

6.6 Results for Al-doped ZnOgrown by PED

6.6.1 Tthe effect of the substrate temperature

Starting from the results obtained for pure ZnO, we defined two fundamental parameters to try to achieve the highest conductivity, keeping the higher transmittance values for ZnO. Thus, also for ZnO-2wt% Al_2O_3 films, we studied the effect of the temperature on the characteristic of the samples and the effect of the background gas type. Moreover, we will provide a major amount of dopant into the target to enhance electrical properties and study its effect on plasma plume formation.

Results due to the temperature variation are summarized in **tab 6.2.**

Sample	Growth temperature	(200) Orientation degree	Resistivity (Ohm*cm)	Average transmittance (%)
AZO-1	200°C	~0 %	$2,2*10^{-1}$	87,4
AZO-2	300°C	96,5	$2,0*10^{-2}$	82,6
AZO-3	400°C	98,5	$1,0*10^{-2}$	79,9
AZO-4	450°C	96,9	$1,5*10^{-1}$	75,1
AZO-5	500°C	93,0	$6*10^{-2}$	91,8
AZO-6	600°C	91,5	2,0	81,4

Tab. 6.2 – Summary of ZnO-2%wtAl_2O_3 results of samples deposited on amorphous quartz at $5*10^{-3}$ mbar of O_2

As reported in literature, the doping affects particularly the transmittance of the AZO specimens[20], but the measured values remain very high in all our samples. In particular, AZO-5 shows the highest average transmittance value and one of the lowest resistivity obtained in this series. However, its resistivity value is still about 2 order of magnitude higher than results reported[25].

Orientation degree follows the behaviour showed by undoped ZnO samples (3rd column of **tab. 6.1**) reaching high (200) orientation degree for deposition temperatures higher than 300°C (**fig. 6.8**), while for a value of 200°C the sample is amorphous.

Since it is not clear the relation between the crystalline degree and the conductivity, further studies are necessary in order to obtain the lowest resistivity values. Probably different causes contribute to this irregular behaviour. From the literature it is known that both amorphous and crystalline doped-ZnO can achieve high conductivity. Defects and oxygen vacancies play an important role and an effective doping control becomes fundamental for the reproducibility of high electrical performance samples.

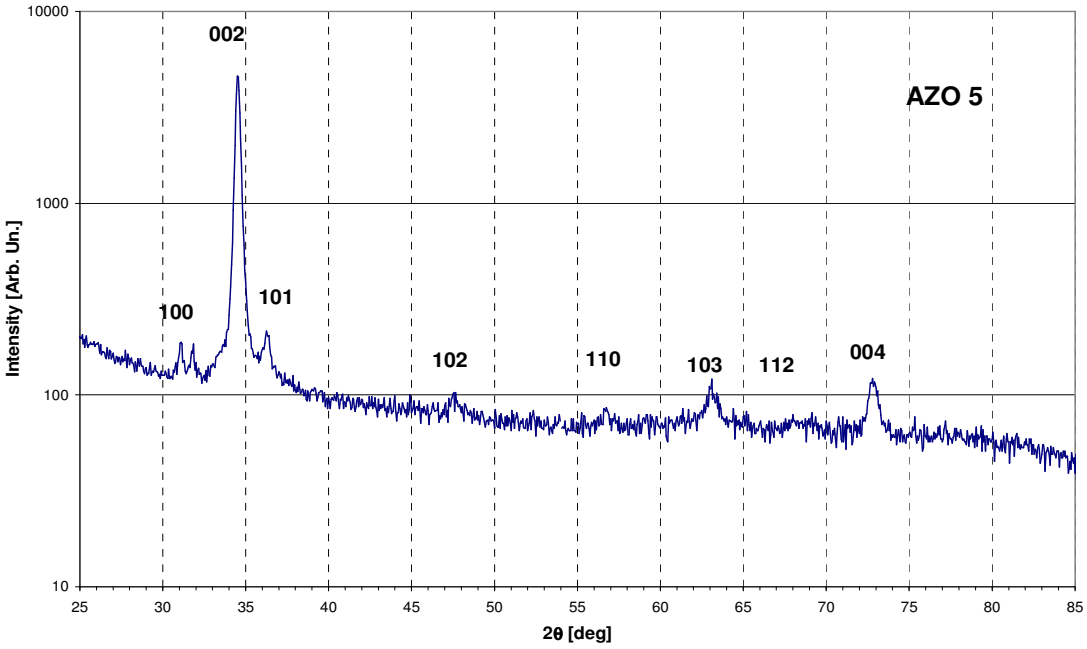

Fig. 6.8 – XRD pattern of the most crystalline and high (200)-oriented AZO film

All the samples produced in this series of deposition show a high transmittance (average value in the 400-1100 nm range) being the lowest value of 75,1% for AZO-4 deposited at 450°C. This result could be predicted on the basis of the results obtained in earlier experiments of undoped ZnO. The graphic reported in **fig. 6.9** shows the comparison of the optical features for the specimens of this series.

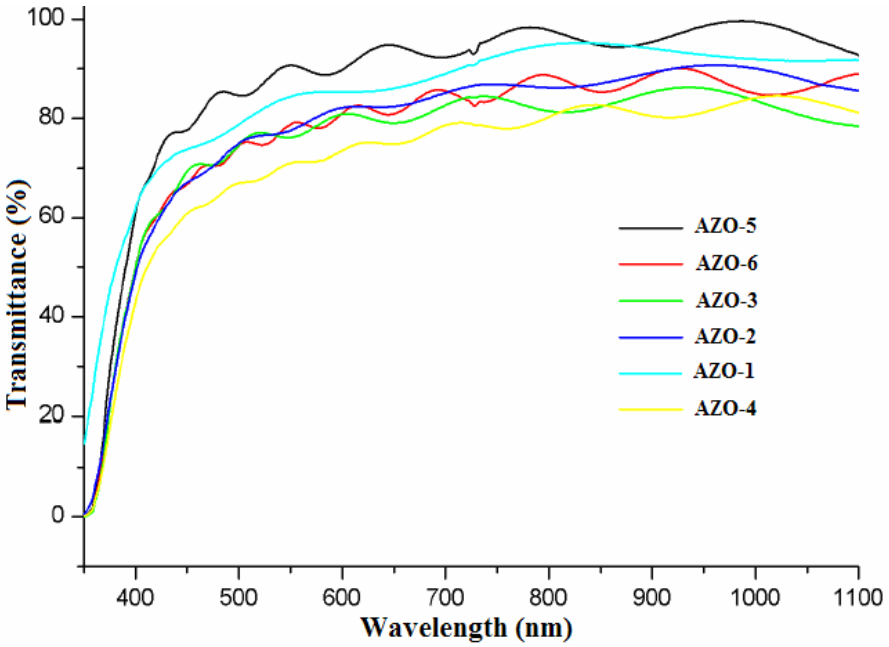

Fig. 6.9 – Transmittance properties of the samples deposited by varying the substrate temperature

The effect of doping and temperature can be observed by analyzing the band-gap values, calculated through the extrapolation method[28]. By neglecting the phenomena of reflection, the absorption coefficient α can be calculated according to the equation:

$$T = A^{(-\alpha t)} \qquad \text{(Eq. 6.3)}$$

where T is the transmittance of the sample as a function of wavelength, *t* is the thickness of the sample and A is a constant usually equal to 1. In the region of main absorption ($\lambda < 400$ nm) the coefficient α follows the Tauch law:

$$\alpha(h\nu) \propto (h\nu - Eg)^n \qquad \text{(Eq. 6.4)}$$

where *Eg* is the energy gap of semiconductor and *n* is the exponent whose value depends on the nature of the electronic transition involved. In particular, *n* = 1/2, 3/2, 2, 3, for direct transitions permitted (as in our case), direct prohibited, indirect permitted and indirect prohibited, respectively. The value of the gap can be calculated from the intersection between the interpolation of the linear part of the equation $\alpha^2 = F(h\nu)$ with the energy axis where $\alpha^2 = 0$.

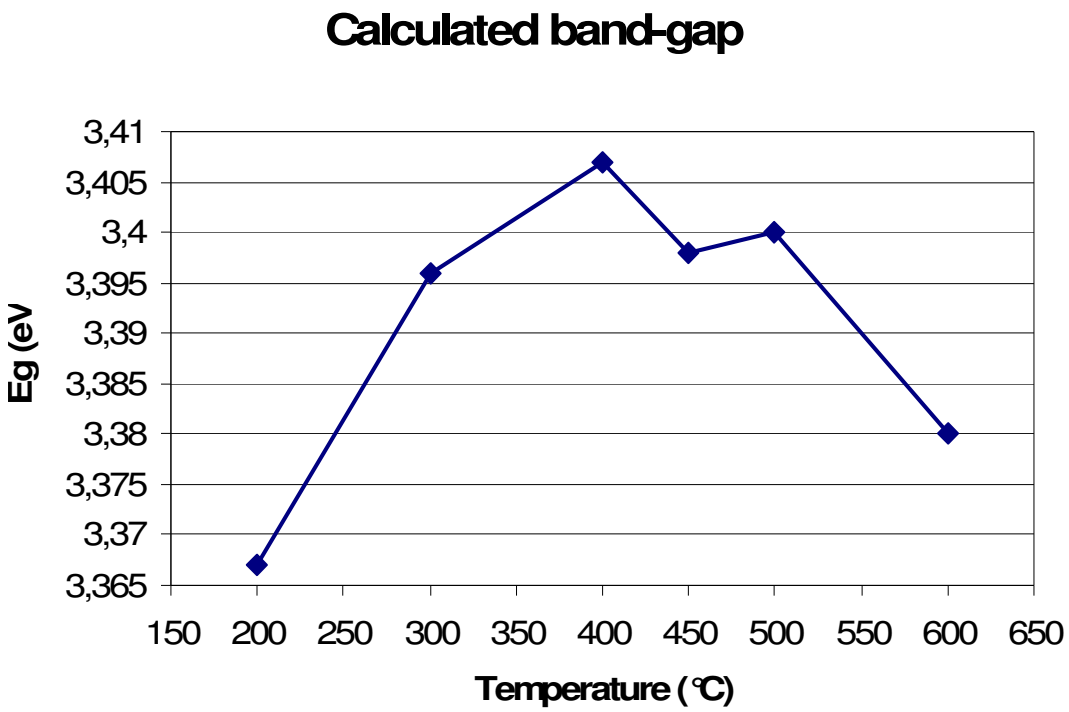

Fig. 6.10 – The calculated Eg of AZO samples grown at different temperature

Analyzing the Eg behaviour as a function of the substrate temperature, we have been able to realize a sort of band-gap engineering for AZO films obtaining the same trend noticed for the (200) orientation degree vs. temperature. Actually, the sample grown at low temperature results structurally amorphous with an Eg value, apparently un-related to the material composition. To explain this behaviour, it can be assumed that only a little amount of Aluminium is activated at lower temperatures and a certain concentration of oxygen vacancy close to that of non-doped ZnO is present. The contributions of these parameters increase with temperature up to a maximum value over which the absorbed oxygen is too high and less defects are formed reducing the concentration of the vacancies in the film.

Morphological analyses have been carried out by SEM and AFM instruments.

The AFM image, taken at "Centro Interdipertimenatle Misure" of Parma University, confirmed the low roughness feature of these samples and the column-coalescence growth already observed in literature. Indeed, the thicker films show an increased flatness of the surface because the layer has been already formed, while thinner specimens show higher roughness value due to the columns-growing before the effective film formation[10].

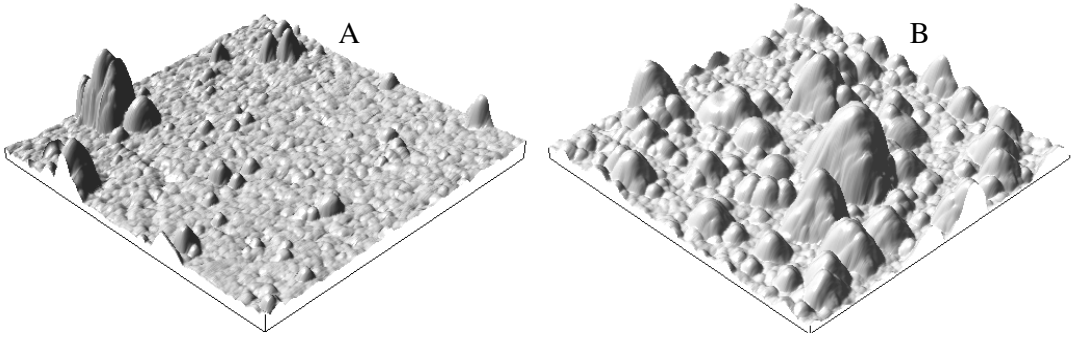

Fig. 6.11 – Two different thick-samples, A and B, with a RMS value of 21,1 nm and 48,5 nm, respectively

In **fig. 6.11**, the AFM images taken in various 5x5 mm zones of a 500 nm thick (A) and a 120 nm thick (B) film are represented; while the former is characterized by a smooth surface with RMS = 21,1 nm and the latter shows a higher roughness with RMS = 48,5 nm due to the growing of single columns on the substrate.

The possibility to control the surface roughness results particularly important in view of the application for the AZO thin film: flat surfaces are needed for PV cells in superstrate configuration while some surface roughness might be preferable for antireflection coating in order to increase the absorbing capability of CIGS solar cells fabricated in substrate configuration.

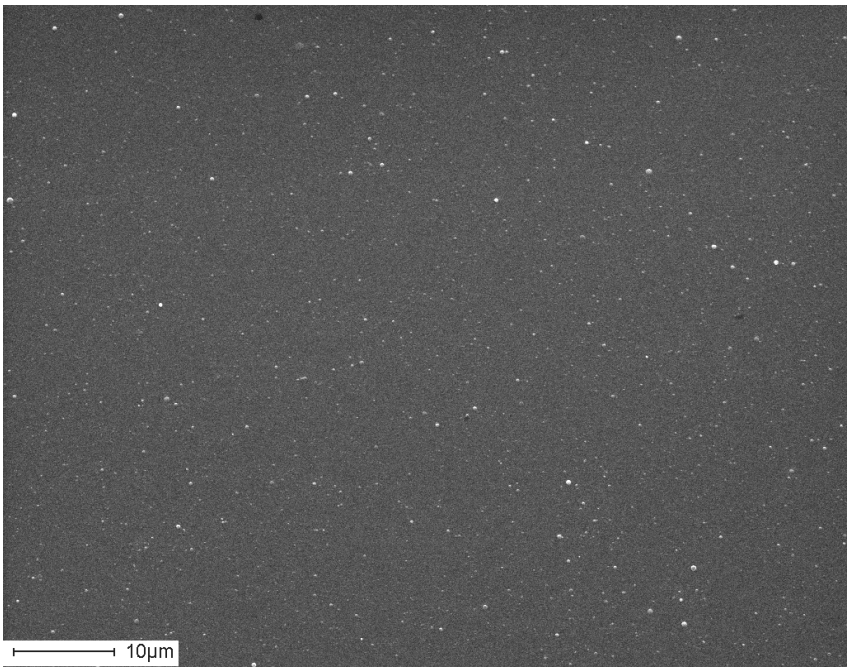

Fig. 6.12 – SEM image of AZO-5 with a very smooth surface

In **fig. 6.12** a smooth sample surfaces can be seen where the number of particulate is relatively low thanks to the background oxygen pressure fixed at $5{,}0*10^{-3}$ mbar.

6.6.2 The effect of the gas

In the second step of the study about AZO thin films grown by PED, we investigated the combined effect of the background gas and the gas used to feed the plasma generated in the hollow cathode of the gun.

Sample	**Background gas ($5*10^{-3}$ mbar)**	**Gun-feeding gas**	**(200) Orientation degree**	**Resistivity (Ohm*cm)**	**Transmittance average (%)**
AZO-OO	Oxygen	Oxygen	98,3 %	$5{,}2*10^{-2}$	72,3
AZO-AA	Argon	Argon	0 %	$2{,}0*10^{+6}$	38,4
AZO-OA	Oxygen	Argon	0 %	$7{,}0*10^{+4}$	**92,7**
AZO-AO	Argon	Oxygen	0 %	$7{,}4*10^{-3}$	69,6
AZO-FO	Forming-gas	Oxygen	98,0 %	**$6{,}8*10^{-4}$**	70,4

Tab. 6.3 – A summary of the results reached by varying the gas type in the chamber and in the gun

All the samples reported in **tab. 6.3** have been grown under the same condition: 500°C of substrate temperature, 15 kV of accelerating voltage and about 1 bar (measured before the pin inlet gas valve) of the gun feeding gas.

The choice for the gas type (to fill the chamber and to feed the gun), has dramatic effects on the AZO film structural, electrical and optical properties. The best resistivity value ($6{,}8*10^{-4}$ ohm*cm) belongs to the gas mixture based on Forming Gas (Ar-4%H_2) as background gas and oxygen for gas-feeding in AZO-FO. This results was expected because the role of H_2 in ZnO doping has been verified in many cases[16]. All the other combinations, excluded the O_2-O_2 reported for comparison, provoke too high resistivity or too low transmittance. Also AZO-FO sample does not show a high value for transmittance and it verifies the effect of the defects and the oxygen vacancies lowering optical properties of ZnO films. Actually, the value of about 70 % for this sample is remarkable for the relatively high background pressure used in this case ($5{,}0*10^{-3}$ mbar). Deposition performed at lower pressure to produce samples characterized by higher values of transmittance are in progress.

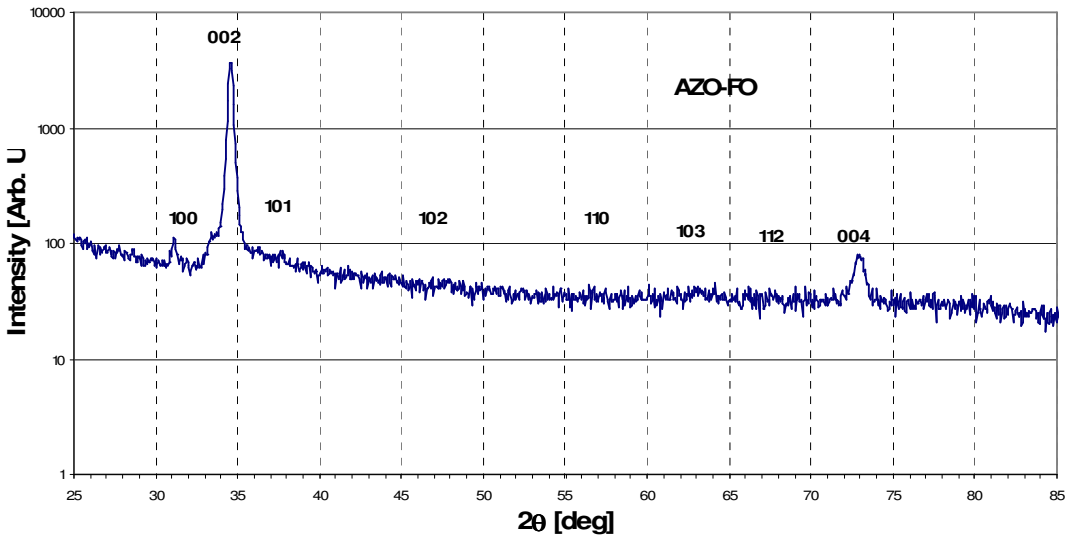

Fig. 6.13 – Log scale of XRD pattern of the AZO-FO sample

A necessary remark about AZO-OA: the transmittance value could be over-estimated because the film was too thin (70 nm) and consequently, the value of resistivity could be so high for the possible cracks formation in the film during the four contact measurements.

From the chemical point of view, contrary to the other films deposited, AZO-AA sample shows a composition quite far from the desired, with an excess of Al in the film up to 11%. Probably, this is due to the absolute absence of oxygen during the ablation when, for the high energy processes involved, Al and Zn formed an alloy losing the oxygen from the relative oxide in the target, rather than simply evaporate.

6.6.3 The effect of the geometry

Once obtained such a low resistivity value, we tried to further improve it by modifying the deposition system varying the geometry of target-gun-substrate and by applying a post-deposition annealing process.

The former solution has been simply realized working on the jointed arm that host the target holder. It has been inclined of 45° respect to the normal to the substrate surface, allowing a longer plume and a larger deposition area (**fig 6.14**). Moreover, in this configuration, the particulate, for the gravity effect, do not fall down directly onto the substrate. Under these conditions and keeping the temperature at 500°C, filling the

chamber with the Forming Gas and feeding the gun with O_2, the samples and related features are reported in **tab. 6.4**.

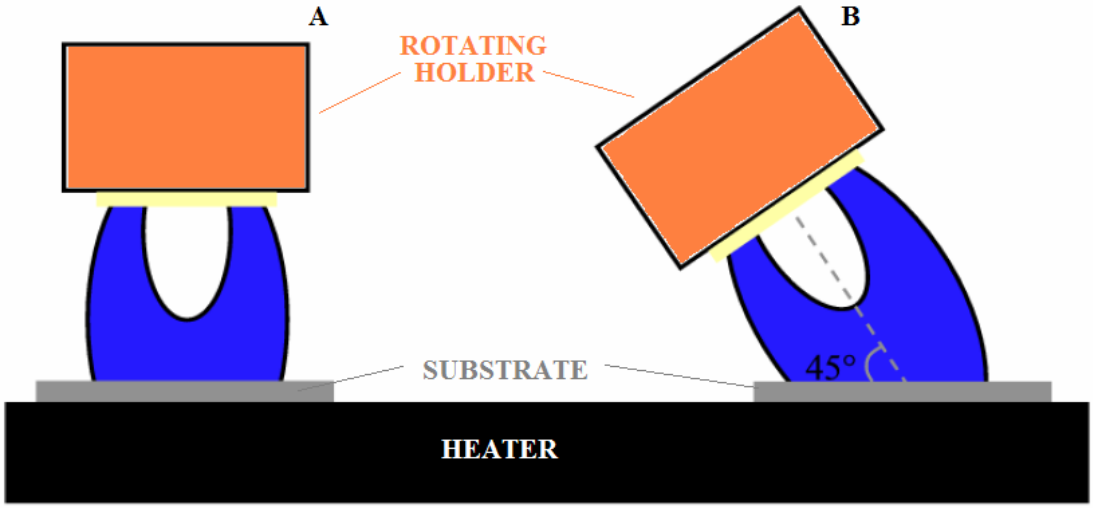

Fig. 6.14 – Vertical (A) and inclined (B) geometry of the target

Due to the different geometry, just the head of the plume could touch the substrate and hence we increased accelerating voltage and reduced background pressure to extend the plume. Moreover, the lower pressure in the chamber ($2*10^{-3}$ mbar), compared to that used to grow AZO-FO, helped us to improve the transmittance value, achieving excellent electrical and optical properties, in view of the use of AZO in PV solar cells production.

Sample	(200) Orientation degree	Resistivity (Ohm*cm)	Transmittance average (%)
AZO-B1	95%	$5,9*10^{-4}$	86,0
AZO-B2	99%	$3,5*10^{-4}$	85,7
AZO-B3	98%	$7,6*10^{-4}$	91,9

Tab. 6.4 – A summary of characteristics owning to the sample grown with geometry B

In order to further reduce the production cost of solar cell, glass substrate have been tested for several AZO deposition, providing good results comparable to the deposition on quartz substrate. Keeping the reducing atmosphere in the chamber, we tried to improve the sample properties, but growing them at low temperature (100°C) the results got worse (2 last lines **in tab 6.5**).

Sample	(200) Orientation degree	Resistivity (Ohm*cm)	Transmittance average (%)
AZO-BG1	98%	$5,8*10^{-4}$	85,4
AZO-BG2	98%	$5,7*10^{-4}$	86,9
AZO-B1001	0%	1,2	86,8
AZO-B1002	93%	$1,6*10^{-3}$	94,6

Tab. 6.5 – Summary of AZO thin films grown on 1x1 cm glass substrate at 450°C and on quartz at 100°C

Tab. 6.5 shows the possibility to obtain high performance AZO films onto an inexpensive substrate, as glass, but high temperature seems to be necessary in order to reach good properties, in particular for the electrical conductivity. This would rule out the possibility to use organic and flexible substrates. Detailed studies must be performed in order to lower the deposition temperature down to suitable values for these type of substrates.

In this configuration we also studied some deposition on larger area on glass substrate. The preliminary results were also encouraging; thickness measures show about a 20% uniformity from the centre to the peripheral zones of the 3x8 cm^2 large substrate with exactly the same orientation degree and a good and uniform transmittance over all the sample. We are currently fabricating a new holder to host larger samples for resistivity measurements by the four probes method.

6.6.4 The effect of the post-deposition annealing

The post-deposition treatment was studied using reducing atmosphere (Forming Gas) as the background gas. The expected results confirmed the observations reported in literature[29,30]: the reducing atmosphere improved the electrical conductivity and decreased the optical transmittance value (**tab. 6.6**) while oxygenation induces the opposite effect

Sample	Pre Resistivity (Ohm*cm)	Pre Transmittance average (%)	Post Resistivity (Ohm*cm)	Post Transmittance average (%)
AZO-1	$2,2*10^{-1}$	87,4	$1,6*10^{-2}$	84,8
AZO-2	$2,0*10^{-2}$	82,6	$6,5*10^{-3}$	77,2
AZO-AO1	$9,5*10^{-4}$	31,2	$1,5*10^{-3}$	57,1

Tab. 6.6 – Summary of some AZO thin films annealed after the deposition

AZO-1 and AZO-2 in this table are the same reported in **table 6.2** while the sample called AZO-AO1 belongs to the Argon-Oxygen deposition series. AZO-1 and AZO-2 are taken to improve their electrical properties and AZO-AO1 to test the annealing procedure on a good sample. For AZO-1 and AZO-2, the experiment confirm the literature observation, but, surprisingly, the latter sample AZO-AO1, while decreasing its electrical properties, improves the optical transmittance by a factor of about 2. Probably, the explanation of this fact can be found in oxygen reorganization inside the structure, reducing the number of vacancies and the defects that typically affect the transmittance, which also are responsible of conductivity.

6.7 Preliminary results on CIGS grown by PED

We tested some deposition of CIGS to explore the feasibility of a solar cell entirely deposited by PED. The target has been prepared in our laboratory by slicing an ingot of CIGS single crystal grown by a modified RF-oven at IMEM. Obviously, in this case, oxygen can not be used neither for background gas, nor for the gun; therefore we used an inert gas such as Argon. The accelerating voltage has been varied between 10 and 17 kV and the Ar background pressure as been set to $5*10^{-3}$ mbar.

The most remarkable results of these preliminary deposition tests showed, are related to the film composition. This is one of the critical issues in CIGS thin film deposition, because the Selenium tends to evaporate during the growth and a post-deposition selenization is generally needed to adjust the stoichiometric ratio of the compound. Avoiding this step, all the associated risks and problems related to the toxicity and the high pressure needed for the Se-based reactant use can be excluded.

By using PED, we noticed a quite good chemical composition of the produced films, where the ratio of the constituent elements is near the optimal value (**tab. 6.7**).

V (kV)	%Cu	%In	%Ga	%Se	%Ga/(In+Ga)
10	9,4	27,1	8,1	55,4	0,23
13,5	18,6	22,2	7,6	51,6	0,25
15	21,1	20,5	7,27	51,1	0,26
17	18,8	21,8	7,27	52,1	0,25

Tab. 6.7 – Chemical composition calculated by EDS data for 4 CIGS thin films

The structural properties have been analyzed by XRD as shown and in **fig. 6.15**.

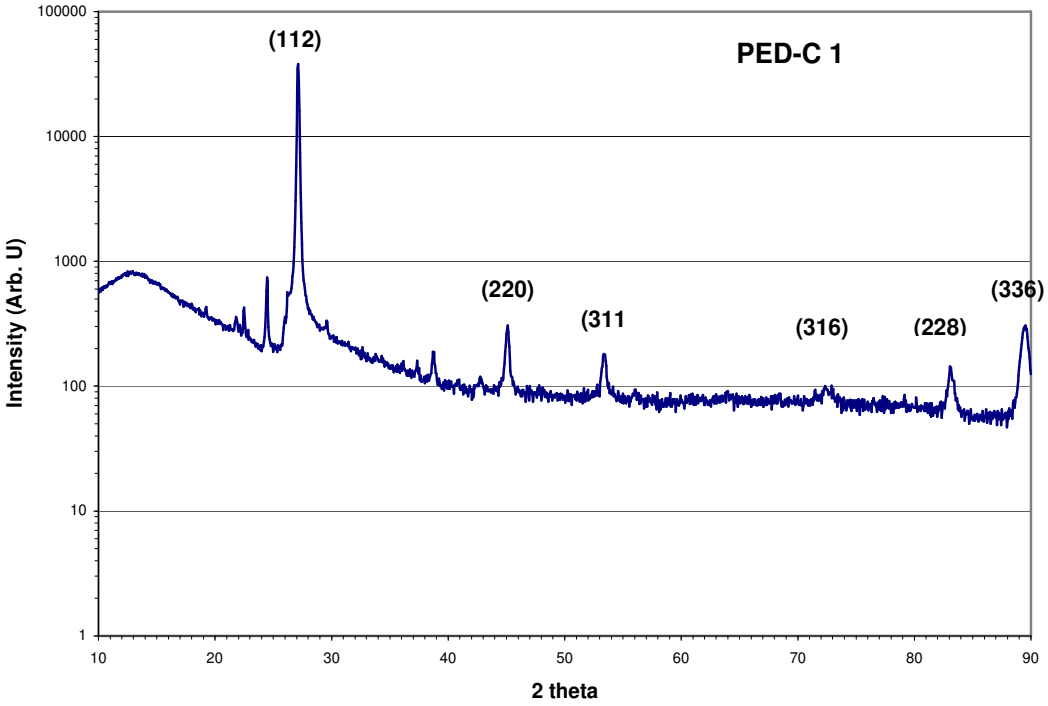

Fig. 6.15 – Log scale of XRD pattern for the sample grown at 15 kV

The (112) reflection is the most important that must be seen to grow efficient absorber-CIGS layer and the XRD shows the high crystalline quality and orientation degree (98%) exhibited by the CIGS thin film deposited on 1x1 cm^2 quartz substrate.

After the remarkable results obtained in TCO deposition, this is the first step towards the realization of an all-PED solar cell based on CIGS.

References

[1] C.G. Granqvist: "Solar energy materials", *Adv. Mater.* (2003) **15**

[2] E.J. Gilman, J.S. Preston:" Transparent conducting films", *Proc. Phys. Soc. London Section B* (1952) **65**

[3] C.G. Granqvist: "Radiative heating and cooling with spectrally selective surfaces", *Appl. Opt.* (1981) **20**

[4] G.B. Smith, G.A. Niklasson, J.S.E.M. Svensson, C.G. Granqvist: "Noble-metal-based transparent infrared reflectors: experiments and theoretical analyses for very thin gold films, *J. Appl. Phys.* (1986) **59**

[5] M. Avrekh, B.M. Thibadeau, O.R. Monteiro, I.G. Brown: "Transparent, conducting, metallic thin films", *Rev. Sci. Instrum*., (1999) **70**

[6] B. Karlsson, C.-G. Ribbing: "Optical properties of transparent heat mirrors based on thin films of TiN, ZrN, and HfN", *Proc. Soc. Photo-Opt. Instrum. Eng*. (1982) **324**

[7] K.E. Andersson, M.K. Wahlstroem, A. Roos: "High stability titanium nitride based solar control films", *Thin Solid Films* (1992) **214**

[8] T. Andersson, C.G. Granqvist: "Morphology and size distributions of islands in discontinuous films", *J. Appl. Phys.* (1975) **48**

[9] N. Kaiser: " Review of the fundamentals of thin-film growth", *Appl. Opt*. (2002) **41**

[10] V.I. Trofimov: "Morphology evolution in a growing film", *Thin Solid Films* (2003) **428**

[11] K. Badeker: "Uber die Elektrische Leitfahigkeit und die Thermoelektrische Kraft Einiger Schwermetallverbindungen", *Ann. Phys*. (Leipzig) **22** (1907)

[12] S. Takaki, K. Matsumoto, K. Suzuki: "Properties of highly conducting ITO films prepared by ion plating", *Appl. Surf. Sci.* (1988) **33/34**

[13] F.O. Adurodija, H. Izumi, T. Ishihara, H. Yoshioka, M. Motoyama: "Effect of Sn doping on the electronic doping mechanism of indium-tin-oxide films grown by pulsed laser deposition coupled with substrate irradiation", *J. Appl. Phys.* (2000) **88**

[14] Gordon R.G.: "Criteria For Choosing Transparent Conductors", *MRS Bull*. (2000) **25**

[15] D.C. Look, J.W. Hemsky, J.R. Sizelove: "Residual Native Shallow Donor in ZnO". *Physical Review Letters* (1999) **82 (12)**

[16] A.Janotti, C.G. Van De Walle: "Hydrogen multicentre bonds", *Nature Materials* (2007) **6 (1)**

[17] Hirschwald, W.H.: "Zinc oxide: an outstanding example of a binary compound semiconductor", *Accounts of Chemical Research* (1985) **18 (8)**

[18] G. Braunstein, A. Muraviev, H. Saxena, N. Dhere, V. Richter, R. Kalish: "p type doping of zinc oxide by arsenic ion implantation", *Applied Physics Letters* (2005) **87**

[19] C. G. Granqvist: "Transparent conductors as solar energy materials: A panoramic review", *Solar Energy Materials & Solar Cells* (2007) **91**

[20] U. Ozgur, Ya. I. Alivov, C. Liu, A. Teke, M. A. Reshchikov, S. Dogan, V. Avrutin, S.-J. Cho, and H. Morkoç: "A comprehensive review of ZnO materials and devices", *Journal of Applied Physics* (2005) **98**

[21] T. Kogure and Y. Bando: "Formation of ZnO nanocrystals in the cubic phase was reported by electron-beam-induced oxidation of ZnS surfaces during TEM observations", *J. Electron Microsc.* (1993) **47**

[22] A. B. M. A. Ashrafi, A. Ueta, A. Avramescu, H.Kumano, I. Suemune, Y.W. Ok and T.Y. Seong: "Growth and characterization of hypothetical zinc-blende ZnO films on GaAs (001) substrates with ZnS buffer layers", *Appl. Phys. Lett.* (2000) **76**

[23] C. G. Van de Walle: "Hydrogen as a Cause of Doping in Zinc Oxide", *Phys. Rev. Lett.* (2000) **85**

[24] B. Kotlyarchuk, V. Savchuk and M. Oszwaldowski: "Preparation of undoped and indium doped ZnO thin films by pulsed laser deposition method", *Cryst. Res. Technol.* (2005) **40**

[25] A. V. Singh, R. M. Mehra, N. Buthrath, A. Wakahara, and A. Yoshida: "Highly conductive and transparent aluminum-doped zinc oxide thin films prepared by pulsed laser deposition in oxygen ambient", *J.Appl. Phys.* (2001) **90**

[26] K. Matsubara, P. Fons, K. Iwata, A. Yamada, K. Sakurai, H. Tampo and S. Niki: "ZnO transparent conducting films deposited by pulsed laser deposition for solar cell applications", *Thin Solid Films* (2003) **431- 432**

[27] M. Nistor, N. B. Mandache and J. Perrière: "Pulsed electron beam deposition of oxide thin films" *J. Phys. D: Appl. Phys*. (2008) **41**

[28] S.H. Jeong, S. Kho, D. Jung, S.B. Lee, J.-H. Boo: "Deposition of aluminum-doped zinc oxide films by RF magnetron sputtering and study of their surface characteristics", *Surface and Coatings Technology*, (2003) **174 –175**

[29] S.J. Baik, J.H. Jang, C.H. Lee, W.Y. Cho, K.S. Lim: "Highly textured and conductive undoped ZnO film using hydrogen post-treatment", *Applied Physics Letters* (1997) **70**

[30] P. Nunes, E. Fortunato, R. Martins: "Influence of the post-treatment on the properties of ZnO thin films" *Thin Solid Films* (2001) **383**

Conclusions and perspectives

In this Thesis, the energy-related problems has been often reminded because they are so relevant and concrete that effective solutions must be quickly found. In this work we presented different materials and technologies for particular uses in energy devices field, trying to solve some of the well-known problems related to production processes and technology.

Superconductors and semiconductors are the fundamental materials on which electronic and electrical devices are based, but the technology to realize high performance materials and efficient devices needs lots of efforts. For this reason several issues must be solved and technology must be improved to reach more effective and low costs solutions, in order to protect the environment and to guarantee better life conditions. For these reasons we investigate superconductors-based devices, in particular HTS-CC, and CIGS-based thin films solar cells to find a new path for the development of energy production and consumption. HTS-CC devices can be used to limit energy waste and improve energy efficiency transport thanks to its zero-resistance at low temperature, making also a great contribution to a higher efficiency turbines for renewable resources, such as wind and hydro power installations. On the other hand thin films solar cell are one of the new frontier to enhance PV modules efficiency making the sun as a concrete and endless energy resource.

During the last three years of PhD, in our laboratory we explored high energy deposition technique as the Pulsed Electron Deposition (PED) for thin films growth in order to solve some of the issues affecting HTS-CC production and CIGS-based PV solar cells.

7.1 Doped-Ceria for HTS-CC

HTS materials present a great potential in several application, in particular for energy devices. HTS-CC have already reached the industrial production but some issues have to be solved in order to reduce fabrication costs and production time. The main reason causing these problems is related to high installation costs of deposition technique and complex buffer layer architecture used. The latter is often related to the former because of many different deposition techniques have to be used in order to deposit the series of different oxide and YBCO layers. Different laboratories and industries adopt this approach but further innovations can allow to realize better cost-effective devices in faster processes.

Indeed, we studied a novel single buffer layer architecture to reach the same properties of multi-buffer layer structure by doping CeO_2 compound a good candidate to be used as buffer layer because of its good lattice match with YBCO. The introduction of iso- or hetero-valent ions such as Zr^{4+}, Sm^{3+}, Yb^{3+}, Ta^{5+} allow the improvement of the structural and the mechanical properties typical for pure Ceria. Indeed, in agreement with different studies carried on SOFC where CeO_2 is one of the most important material, the dopant ions such as Zr^{4+}, Yb^{3+} and Ta^{5+} induce the shrinkage of the CeO_2 lattice parameter and enhance the Young's modulus of the film. This characteristic has been observed also for the Sm-doped Ceria, although the shrinkage effect did not occur. Both these effects allowed to grow doped-Ceria films with a thickness up to 260 nm, much greater than the critical thickness (~100 nm) of pure Ceria, without any cracks on the surface. Moreover, the layers showed higher mechanical properties and higher dielectric strength with an effective barrier ability against ion interdiffusion demonstrated by the high performance YBCO layer deposited by Thermal Co-Evaporation (TCE) with SNEO (Supersonic Nozzle Enhancement Oxygenation) device onto a 8 cm sample showing a Tc of 90,5 K and 36 MA of critical current.

All these experiment have been performed by e-beam evaporation. Nevertheless, seems inappropriate to grow long-length HTS-CC, in particular beacuse the chemical composition transfer is not optimal, due to the physical process related to the evaporation. This technique is based on continuous and low-energy electron beam heating the target until the evaporation. Obviously, this process is related to the melting point of all the compounds present in the crucible, therefore, the vapours will show a different composition from the target and, subsequently, the film will grow poor of the lower-melting temperature compound.

In order to test long deposition and improve the doped-Ceria film properties, a novel deposition technique has been recently installed at IMEM-CNR. This is a pulsed high energy deposition system called PED (Pulsed Electron Deposition). It is conceptually similar to PLD system but with lower installation and running costs and higher efficiency energy transfer to the target, due to an electron flux, different from the LASER photon flux.

Doped-Ceria samples grown by PED show similar properties of the ones deposited by e-beam evaporation but up to 700 nm thick and crack-free films has been reproducibly obtained. This is probably due to the typical particulate falling from the target during the film growth. These droplets are included into the layer during the deposition, forming defects and point of elastic energy relaxation instead of cracking.

The samples obtained by PED have been used for YBCO deposition by TCE and PLD techniques. In both cases, the doped-Ceria layer shows good barrier effect, avoiding ions interdiffusion and allowing the growth of a high performance YBCO with Tc of 88,3 K and 88,0 K, respectively. The PLD-YBCO growth has been particularly interesting because it occurs at high temperature (850°C, i.e. about 200°C higher than the temperature used in TCE), demonstrating that single buffer layer grown by PED represent a reliable template for low-cost HTS-CC characterized by a simplified structure, fabricated by different deposition methods.

As far as the perspectives concern, doped-Ceria will be tested with different YBCO deposition techniques, such as MOD or sputtering. Moreover, further analysis will be made on doped-Ceeria films to completely understand the remarkable mechanicla properties achieved and to correlate them with the type of doping and the role of PED system. These activities will be continued in the frame of national and international collaborations established in the last years where the main goal is the development of all-PED and long length HTS-CCs[1].

7.2 TCO for PV applications

In parallel with the activity on HTS-CC, we started an interesting activity about ZnO thin films deposition for its application in PV field. Second generation solar cell are based on thin film, with a multi-layers structure where a p-n junction is grown between two conductive layers. Generally, these are made of a thin metal layer as the back contact and a Transparent Conductive Oxide (TCO) as front contact. The optical transmittance of this film coupled to its high conductivity are fundamental properties in high efficiency solar cells production. Most used p-type semiconductor are based on Si, CdTe, AlGaAs or CIGS. The latter is a compound with the formula Cu(In, Ga)Se_2 and appears as the optimal absorber layer for PV cells thanks to its characteristics, such as an Energy gap (Eg) value

between 1,0 and 1,7 eV depending on the amount of added Ga. PED system has been used to deposit pure ZnO and Al-doped ZnO (AZO) onto quartz and glass substrate as TCO. The optical and electrical properties have been correlated to the substrate temperature, the gas type and the geometry of the electron flux-target-substrate.

As far as ZnO concerns, samples of amorphous and crystalline layers have been obtained with a resistivity value of $1,2*10^{-1}$ Ohm*cm and an optical transmittance up to 97%. For AZO, in spite of the doping effect, the optical transmittance measured between 400 and 1100 nm remains higher than 90% with a resistivity value of $6*10^{-2}$ for processes performed in O_2 atmosphere. By changing the gas type from O_2 to a reducing Forming Gas, resistivity achieved $3,5*10^{-4}$ Ohm*cm in a inclined-target geometry. Thanks to this method, AZO films performance reached the state-of-the-art level in PV field.

This is just the first step for our PV experience, but it has been encouraging and brought a lots of purpose and ideas for the future. One of them was related to the possibility of growing CIGS as absorber layer in view of an all-PED solar cell production. The CIGS deposition has been performed onto quartz substrates and a high crystalline quality films without an evident chemical composition deviation have been realized. Surprisingly, the film did not result poor in Se, hence the typical and undesired selenization process, necessary to adjust the Se content with other deposition techniques, could be avoided. Also in this field, PED appears effective and reliable for thin film deposition and the all-PED CIGS-solar cell[2] seems a concrete possibility in order to reduce costs and complexity of the cell production.

7.3 PED technique

Since the installation, PED system has demonstrate several advantages compared to other deposition technique, in particular versus the thermal evaporation by electron beam used in the same period for doped-Ceria deposition. Indeed, it confirmed the high chemical composition transfer from the target to the growing films and it has been very useful in AZO deposition for the optimal control of the doping inside and for CIGS, where stoichiometry is one of the main issues. Moreover, in spite of its relatively low installation and running costs, it allows to produce either high crystalline quality and oriented buffer layer and high conductive an transparent films. From the morphological point of view, the

presence of particulate, typical for high energy deposition technique, onto the surface of PED-grown samples is a well-known issue; however, some tricks helped us to dilute them, such as the substrate movement, higher working pressure, lower accelerating voltage or different geometry (tested on a specific deposition-campaign to enhance PED knowledge). Furthermore, long-time deposition showed a high reliability and great independence from the target history and composition, contrary to the case of e-beam evaporation technique.

On the other hand, PED is a relatively novel technique and its knowledge is not complete. The PED apparatus installed at IMEM presents many margins of improvement and several studies must be carried on to completely understand its operation method. Interesting test we have scheduled are dedicated to many aspects of the system:

1. the geometry of the whole gun that can be mounted in horizontal position;
2. the electronic circuit controlling the discharge (capacitors, trigger, new cathode shapes);
3. alternative material for insulating guide;
4. the optimization of the device for the pulsed e-beam measurements[3];
5. the effect of the target on the ablation plume (density, conductivity, sintering temperature, load applied in pellet formation);
6. successive depositions of different materials with a revolver target holder;
7. long-time deposition for long length and all-PED HTS-CC;
8. all-PED solar cells based on CIGS;
9. tests on different materials for various application.

The innovative studies on PED carried out at IMEM allowed the deposition of 3 application patents exciting high interest in industrial field.

PED choice could be defined as the concrete solution to realize cost-effective devices for energy application creating more favourable and fruitful collaborations with the present industrial partners. To properly manage these collaborations, a spin-off company of the CNR will be created at IMEM with the purpose to industrialize the promising results so far obtained at a laboratory level.

References

[1] Zannella S., Gilioli E., Bindi M., Pattini F., Bissoli F., Rampino S., Baldini M.
Metodo di realizzazione di film sottili di biossido di Cerio drogato, in particolare costituenti strati barriera di nastri compositi superconduttori (patent application n.MI2007A001531)

[2] CNR-IMEM, Gilioli E., Pattini F., Bissoli F., Rampino S.
Struttura di una cella solare a film sottile "CADMIUM-FREE" basata su uno strato assorbitore di CU (IN, GA, AL) (SE, S)$_2$ e ottenuta mediante tecnica di deposizione a elettroni pulsati (patent application n.MI2008A002091)

[3] CNR-IMEM, Gilioli E., Pattini F., Bissoli F., Rampino S., Ferrari C., Mazzer M.
Metodo e apparecchiatura di realizzazione di film sottili su un substrato tramite processo di deposizione a elettroni pulsati (patent application n.MI2008A002090)

Acknowledgments

I am very grateful to Dr. Edmondo Gilioli, my scientific point of reference during this work, for his surprising enthusiasm which allowed me to "overtake" (actually in the concrete sense of the term) all the obstacles found and for his great interest in more or less serious discussion outside research ambient. I wish to express my gratitude to the former IMEM-CNR director, Dr. Lucio Zanotti for having accepted me in this institute and for his sincere interest in all the activities carried on at IMEM. At the same time, I express my sincere acknowledgments to the current director, Professor Salvatore Iannotta for his determined conviction in continuing to support the superconductivity activity at IMEM Institute . I wish to thank Dr. Francesca Licci who has initiated and promoted the research project on HTS at IMEM and to Professor Massimo Marezio, who drove the SCENET school and supported the coated conductors activity in this Institute. I would like to thank Dr. Sergio Zannella (Edison S.p.A.) who gave me the opportunity of working in a frame of this project, Drs. Massimilino Bindi and Stefano Ginocchio for their precious collaboration in thin film deposition and electrical measurements, respectively. Special thanks to my colleague Dr. Francesco Bissoli for scientific discussions, for his patience and interest in political and legal aspects of the working world and for his great efforts in organization and promotion of healthy sport activities. Many thanks also to, Dr. Michele Baldini for his contribution to the work on doped ceria and for the pleasant time spent together in Torino and Trofarello. A special thanks to Dr. Massimo Mazzer for sharing his incredible knowledge about photovoltaics, Mr. Tullo Besagni for his patience and reliable technical assistance in the XRD characterization work, Claudio Minari for his concrete work to realize the stranger devices ever seen, Mrs. Patrizia Ferro for technical assistance in the chemistry laboratory and the attention to the safety of all the researchers. Many thanks to Dr. Davide Calestani for the never-ending availability in SEM measurements, Professor Scardi of the University of Trento for pole figures, Dr. Carlo Vignali for having explained me all the secrets of AFM technique. I would like to thank also Professor Manfredo Manfredi and Anna Painelli, coordinators of the Graduate School of Materials Science and Technology of the Parma University, for their attention and problem solving ability. Finally, I would like to thank all of the colleagues of the IMEM Institute for the nice moments spent together. In particular all of my wishes to the temporary researchers of the institute: without them many research activities at IMEM would be already expired.

And finally, because “the last shall be first”, (even if they are already the first ones for me) a sincere and friendly THANK to Stefano Rampino for his great interest and obstinacy in wondering to understand everything inside and outside the material science; to Simone Fabbrici for his calm and his tolerance for all the jokes we played; to Fabio Papini, Paolo Zurlini and Roberto Jakomin, who shared a more or less long pleasant period in the same house; to Simone Frati and his loving of madness and electronic, car and motorcycle market knowledge.

Thanks to all my friends of the Community of Sant’Egidio who, since 1998, open my mind to the whole world outside my windows trying to realize a better one.

Never-ending thanks to my family, that supported me up to now with sacrifices and love.

Always according to the principle that the “very last” is concretely the “very first”, I finally express all of my gratitude and love to Alessia, my exceptionally sweet present and future.